Ph.D. Thesis

Induced Seismicity in Enhanced Geothermal Systems: Assessment of Thermo-Hydro-Mechanical Effects

Author:
Silvia De Simone

Supervisors:
Dr. Jesús Carrera Ramírez
Dr. Víctor Vilarrasa Riaño

Hydrogeology Group (GHS)

Department of Civil and Environmental Engineering, Universitat Politècnica de Catalunya (UPC)

Institute of Enviromental Assessment and Water Research (IDAEA, CSIC)

February, 2017

This thesis was funded by AGAUR (Generalitat de Catalunya) through the "Grant for Universities and Research Centers for the Recruitment of New Research Personnel" (FI-DGR 2012). Financial support was also provided by the "TRUST" project (European Community's Seventh Framework Programme FP7/2007-2013 under grant agreement nº 309607) and by the "FracRisk" project (European Community's Horizon 2020 Framework Programme H2020-EU.3.3.2.3 under grant agreement nº 640979).

Abstract

Micro-seismicity, and especially felt seismicity, induced by Enhanced Geothermal Systems (EGS) operations is a matter of scientific interest, not only because of the related risks and concerns, but also because the correspondence between injection and seismic activity still remains unclear. The Thesis aims to deepen the understanding of the involved Thermo-Hydro-Mechanical (THM) processes, in order to explain and manage co- and post-injection seismicity.

First, we investigate the HM coupling and its effects on pressure response. Fluids injection exerts a force over the aquifer that causes deformation. This implies that Specific Storage, which reflects the capacity of permeable media to deform, cannot be treated as a single parameter, like in classical groundwater hydrology, because deformation also depends on aquifer geometry and on surrounding formations, which constrain displacements. We demonstrate the non-local nature of storage (i.e., its dependence on the poroelastic response over the whole aquifer) by means of analytical solutions to the transient pressure response to injection into one-dimensional and cylindrical finite aquifers, while acknowledging HM coupling. We find that the pressure response is faster and much greater than predicted with traditional solutions.

Second, we consider non-isothermal injection and compare the effects of HM and TM couplings. We present analytical expressions for long-term hydraulic and thermal stresses and displacements for unidirectional and radial geometries. To obtain them, we assume steady-state fluid flow and develop an easy-to-use solution to the transient heat transport problem. The solution is then used to illustrate the poroelastic and thermoelastic response and, in particular, the sensitivity of stresses to the outer mechanical boundary conditions.

Third, we perform coupled HM and THM simulations of cold water injection in a fault-intact rock system, which allows us to analyze mechanical stability changes during injection in the vicinity of the well. Simulation results show that temperature drop induces a significant perturbation of stresses in the intact rock near the injection well. This perturbation is likely to induce seismicity around critically oriented fractures. HM simulations show that fracture stability depends on the orientation of the faults and on the initial stress tensor. Results show

that TM effects dominate and could induce seismicity, when the largest confining stress acts perpendicular to a fracture.

Finally, we investigate the mechanisms that may induce seismicity after the end of fluid injection into a deep geothermal system (post-injection seismicity). Apart from the direct impact of fluid pressure increase, we acknowledge thermal effects due to cooling and stress redistribution caused by shear slip along favorably oriented fractures during injection. The effect of these three processes are analyzed both separately and superimposed. We find that post-injection seismicity may occur on unfavorably oriented faults that were originally stable. During injection, such faults become destabilized by thermal and shear slip stress changes, but remain static by the superposition of the stabilizing effect of pressure forces. However, these fractures become unstable and fail when the pressure forcing dissipates shortly after injection stops abruptly, which suggests that a slow reduction in injection rate may alleviate post-injection seismicity.

Resumen

La micro-sismicidad inducida por operaciones relacionadas con los Sistemas Geotérmicos Estimulados ha originado un gran interés científico, no solo por el riesgo y la preocupación que conlleva, sino también porque no se entiende completamente la relación entre inyección de fluidos y actividad sísmica. Esta tesis pretende avanzar en la comprensión de los procesos hidro-termo-mecánicos (THM) que causan esta sismicidad, para poder explicarla y gestionarla.

En primer lugar, hemos investigado el acoplamiento hidro-mecánico (HM) y su efecto sobre las presiones. En Hidrología Subterránea clásica el almacenamiento especifico expresa la capacidad del acuífero de deformarse tras una variación de presión. Sin embargo, la sobrepresión generada por la inyección ejerce una fuerza que deforma todo el acuífero, dependiendo de su geometría y de las formaciones adyacentes. Por ello, el almacenamiento no se puede expresar con un solo parámetro, sino que depende de la respuesta poro-elástica de todo el acuífero, por lo que decimos que el almacenamiento específico es "no-local", cosa que mostramos mediante soluciones analíticas de la respuesta transitoria al problema HM de la inyección en acuíferos de dimensión finita, con geometría tanto unidimensional como cilíndrica.

Seguidamente, hemos considerado una inyección no isoterma y comparado los efectos del acoplamiento hidro-mecánico (HM) y termo-mecánico (TM). Hemos obtenido expresiones analíticas para las tensiones y los desplazamientos inducidos a largo plazo por la perturbación hidráulica y térmica, en el caso de dominios unidireccional y radial. Para ello, hemos considerado flujo estacionario y desarrollado una solución analítica sencilla para el transporte de calor en régimen transitorio, lo que nos ha permitido calcular la respuesta poro y termo-elástica y en particular la sensibilidad de las tensiones a las condiciones mecánicas en el contorno exterior.

A continuación, hemos desarrollado simulaciones HM y THM acopladas de la inyección de agua fría en un sistema formado por una falla embebida en una roca intacta, a fin de analizar las variaciones de la estabilidad mecánica durante la inyección. Las simulaciones HM muestran que la estabilidad de las fracturas depende de su orientación y del tensor de tensiones inicial. Concluimos que la reducción de temperatura provoca cerca del pozo una fuerte perturbación de las

tensiones, que puede inducir sismos en fracturas orientadas críticamente, especialmente cuando la tensión máxima actúa perpendicularmente a la fractura.

Finalmente, hemos estudiado los mecanismos que pueden inducir sismos al parar la inyección de fluidos en sistemas geotérmicos profundos (sismicidad post-inyección). Además del efecto directo del aumento de la presión, hemos considerado el efecto térmico debido al enfriamiento y la redistribución de tensiones generada por el movimiento de cizalla que ocurre durante la inyección en fracturas favorablemente orientadas. Estos efectos se han analizado tanto por separado como superpuestos. De los resultados podemos deducir que la sismicidad post-inyección puede ocurrir a lo largo de fracturas que eran inicialmente estables y se desestabilizan durante la inyección, debido a las tensiones térmicas y a las inducidas por la cizalla, pero se mantienen estables gracias a las fuerzas de presión. Posteriormente, estas fracturas rompen cuando se interrumpe la inyección, ya que las presiones se disipan rápidamente. Esto sugiere que la sismicidad post-inyección puede atenuarse con una reducción lenta del caudal de inyección.

Resum

La micro-sismicitat induïda per operacions relacionades amb els Sistemes Geotèrmics Estimulats ha originat un gran interès científic, no només pel risc i la preocupació que comporta, sinó també perquè la relació entre la injecció de fluids i l'activitat sísmica no s'entén completament. Aquesta tesi pretén avançar en la comprensió dels processos hidro-termo-mecànics (THM) que causen aquesta sismicitat, per poder explicar-la i gestionar-la.

En primer lloc, hem investigat l'acoblament hidro-mecànic (HM) i el seu efecte sobre les pressions. En Hidrologia Subterrània clàssica l'emmagatzematge especifico expressa la capacitat de l'aqüífer de deformar-se després d'una variació de pressió. Malgrat això, la sobrepressió generada per la injecció exerceix una força que deforma tot l'aqüífer, depenent de la seva geometria i de les formacions adjacents. Per això, l'emmagatzematge no es pot expressar amb un sol paràmetre, sinó que depèn de la resposta poro-elàstica de tot l'aqüífer, per la qual cosa diem que l'emmagatzematge específic és "no-local", cosa que vam mostrar mitjançant solucions analítiques de la resposta transitòria al problema HM de la injecció en aqüífers de dimensió finita, amb geometria tant unidimensional com cilíndrica.

Seguidament, hem considerat una injecció no isoterma i comparat els efectes de l'acoblament hidro-mecànic (HM) i termo-mecànic (TM). Hem obtingut expressions analítiques per a les tensions i els desplaçaments induïts a llarg termini per la pertorbació hidràulica i tèrmica, en el cas de dominis unidireccional i radial. Per a això, hem considerat flux estacionari i desenvolupat una solució analítica senzilla per al transport de calor en règim transitori, la qual cosa ens ha permès calcular la resposta poro i termo-elàstica i en particular la sensibilitat de les tensions a les condicions mecàniques en el contorn exterior.

A continuació, hem desenvolupat simulacions HM i THM acoblades de la injecció d'aigua freda en un sistema format per una falla embeguda en una roca intacta, a fi d'analitzar les variacions de l'estabilitat mecànica durant la injecció. Les simulacions HM mostren que l'estabilitat de les fractures depèn de la seva orientació i del tensor de tensions inicial. Concloem que la reducció de temperatura provoca prop del pou una forta pertorbació de les tensions, que pot induir sismes en fractures orientades críticament, especialment quan la tensió màxima actua perpendicularment a la fractura.

Finalment, hem estudiat els mecanismes que poden induir sismes quan s'atura la injecció de fluids en sistemes geotèrmics profunds (sismicitat post-injecció). A més de l'efecte directe de l'augment de la pressió, hem considerat l'efecte tèrmic a causa del refredament i la redistribució de tensions generada pel moviment de cisalla que ocorre durant la injecció en fractures favorablement orientades. Aquests efectes s'han analitzat tant per separat com superposats. Dels resultats podem deduir que la sismicitat post-injecció pot ocórrer al llarg de fractures que eren inicialment estables i es desestabilitzen durant la injecció, a causa de les tensions tèrmiques i a les induïdes per la cisalla, però es mantenen estables gràcies a les forces de pressió. Posteriorment, aquestes fractures trenquen quan s'interromp la injecció, ja que les pressions es dissipen ràpidament. Això suggereix que la sismicitat post-injecció pot atenuar-se amb una reducció lenta del cabal d'injecció.

Sintesi

La microsismicitá indotta dalle operazioni associate ai Sistemi Geotermici Stimolati ha suscitato grande interesse scientifico, non solo a causa del rischio e della preoccupazione che essa comporta, ma anche perché la ralazione tra l'iniezione di fluidi e l'attivitá sísmica non é del tutto chiara. Questa tesi si propone di approfondire la comprensione dei processi termo-idro-meccanici responsabili della sismicitá indotta sia durante che dopo l'iniezione, di modo da poterla spiegare e gestire.

Per prima cosa, abbiamo studiato l'accoppiamento idro-meccanico e i suoi effetti sulle pressioni. L'iniezione di fuidi esercita una forza sull'acquifero che comporta la sua deformazione. L'immagazzinamento specifico esprime la capacitá di deformarsi del mezzo poroso, la quale non puó essere ridotta ad un singolo parametro, come é d'uso nell'Idrogreologia classica, perché la deformazione in realtá dipende dalla geometria dell'acquifero e dalle formazioni circostanti, che possono impedirne l'espansione. Tale natura non-locale dell'immagazzinamento specifico (ossia la sua dipendenza dalla risposta poroelastica nell'intero acquifero) é dimostrata in questa tesi per mezzo di soluzioni analitiche che esprimono la risposta transitoria delle pressioni al problema idromeccanico dell'iniezione in acquiferi di dimensione finita con geometria unidimensionale e cilindrica.

In secondo luogo, abbiamo messo in conto la possibilitá di un'iniezione non-isoterma e abbiamo confrontato gli effetti dell'accoppiamento idro-meccanico e termo-meccanico. Abbiamo presentato espressioni analitiche che descrivono le tensioni e gli spostamenti indotti nel lungo termine dalla perturbazione idraulica e termica nel caso di dominio unidirezionale e radiale. A tal fine, abbiamo assunto flusso stazionario e abbiamo sviluppato una soluzione semplice per il trasporto di calore in transitorio. Tale procedimento ci ha permesso di mostrare la risposta poroelastica e termoelastica ed, in particolare, la sensibilitá delle tensioni alle condizioni meccaniche agenti sul contorno esterno.

In seguito, abbiamo svolto simulazioni accoppiate idro-meccaniche e termo-idro-meccaniche dell'iniezione di acqua fredda in un sistema composto da una faglia all'interno di una matrice solida, con l'obiettivo di analizzare le variazioni della stabilitá meccanica durante l'iniezione. Le simulazioni idro-meccaniche rivelano che la stabilitá delle fractture dipende dalla loro orientazione e dal tensore delle tensioni iniziale. Inoltre, l'abbassamento di temperatura induce una

rilevante perturbazione delle tensioni vicino al pozzo, la cual cosa puó indurre sismicitá lungo fratture criticamente orientate, soprattutto quando la tensione principale massima agisce perpendicolarmente ad esse.

Infine, abbiamo studiato i meccanismi che possono indurre sismi dopo il termine dell'iniezione di fluidi in sistemi geotermici profondi (sismicitá post-iniezione). Oltre all'impatto diretto dell'aumento di pressione, abbiamo considerato anche l'effetto termico dovuto al raffreddamento e la redistribuzione di tensioni generata dallo scorrimento di taglio che avviene durante l'iniezione lungo fratture favorevolmente orientate. Tali effetti sono analizzati sia separatamente che sovrapposti. Da quest'analisi deduciamo che i terremoti post-iniezione possono verificarsi lungo faglie orientate non-favorevolmente, che al principio erano stabili. Infatti, durante la fase di iniezione, tali faglie vengono destabilizzate dalle tensioni termiche e di scorrimento, ma rimangono stabili grazie all'effetto stabilizzante delle forze di pressione. In seguito, tali fratture rompono nel momento in cui le pressioni si dissipano rapidamente, dopo la conclusione brusca dell'iniezione. Ció suggerisce che una lenta riduzione della portata iniettata puó mitigare la sismicitá post-iniezione.

Acknowledgements

I would like to express my deep gratitude to my advisors, Dr. Jesús Carrera and Dr. Victor Vilarrasa. To Jesús, for giving me the opportunity of this PhD, for guiding me, on one hand, and for letting me grow on my own, on the other hand. Thank you for always pushing me further. Second, but not less important, I sincerely acknowledge Victor for teaching me, for all the suggestions and the motivation he was giving me through all these years, even when he was far away.

I am also grateful to Andrés Alcolea and Peter Meier for valuable discussions that have contributed to the development of this Thesis. I would also like to thank Sebastiá Olivella, for his interest in my work and for useful suggestions, and Paul Hsieh, whose accurate revision have significantly helped to improve the understanding of the Thesis.

Then I have to sincerely thank all my fellows of the Hydrogeology Group for the awesome working atmosphere, for the stimulating discussions, for the time we were working together (yes, also for the stressful time before deadlines) and, most of all, for sharing the good and the bad days. I am deeply grateful to Anna, Estanis, Violeta, Gonzalo, Victor and Bruno, who were the first ones to welcome me (thanks to be patient with my Spanish!) and have become very good friends. I'm also especially grateful to the ones who did the whole PhD journey with me, Bayaraa, Mar and Alex. That was a long way, but we did it! A big thank to all the other members of the group, in particular to Francesca, Laura, Yoar, Linda, Quim, Rotman, Berta, Sheila, Alessandro, Lazaro, Alba, Miguel Angel, Jordi. Thanks for all the coffees, the cakes, the beers and the laughs. Every one of them has been important to me during the process.

Finally I would like to acknowledge my family for their unconditional love and support. Thanks for always being there for me. A special thank goes to my Alessandro, for putting up with me through all the stressful moments of these years and to be responsible, in some way, of the beginning of this adventure.

Muchas gracias!

Table of Contents

List of Figures

List of Tables

1

Introduction

1.1 Background and motivation

Geothermal energy represents a powerful and clean carbon-free alternative in the current scenario of energy demand. Heat stored in the Earth has been exploited since ancient Roman times. Contrary to conventional hydrothermal resources, such as hot springs at relatively shallow depth, which are limited in their location and potential for supplying electricity, deep geothermal energy constitutes an attractive prospect, able to generate enormous and virtually unlimited energy (Giardini, 2009).

Deep geothermal energy involves the exploitation of hot reservoirs, with temperature higher than 100°C, which are generally found in crystalline basements at a depth of 3-5 km, depending on the natural geothermal gradient. Cold fluid injected into the formation through a borehole is heated after circulation through the reservoir and extracted through one or more wells. Extracted heat can be distributed in district heating, used to produce electricity, or both. It is estimated that exploitation of a reservoir at 150°C can produce 40 MW of thermal power and 5 MW of electricity with production flow rates in the range of 100 L/s (Jung, 2014). However, to ensure a sufficient efficiency, the heat exchanger has to allow massive fluid circulation, which means that adequate hydraulic conductivity between injection and production wells is required (Tester et al., 2007). The crystalline basement is not permeable enough, despite the presence of fissures, fractures and faults (Jung, 2013). Hydraulic stimulation is performed to overcome this limitation. It involves the injection of a large volume of water (several thousand cubic meters) at high flow rates in order to increase permeability by creating or enhancing fractures (Batchelor, 1982). This process leads to the development of an Enhanced Geothermal System (EGS).

Hydraulic stimulation usually induces seismic or microseismic events, which are generally weak (i.e., Magnitude, M<2) and certifies the effectiveness of the

operation. However, in some occasions, this induced seismicity has reached sufficient magnitude to be felt by the local residents (Table 1.1), raising public concern (Majer and Peterson, 2007; National Academy of Science, 2012). It is clear that, for EGS to become a standard technology, such levels of seismic activity during

Table 1.1: Maximum earthquake magnitude of events associated with hydraulic stimulation in selected EGS projects. Asterisks denote events occurring after stop of the injection (sources: Baisch et al., 2010; Evans et al., 2012; Zang et al., 2014)

EGS project	**Activity**	**M_{max} (year)**	**References**
KTB (Germany)	Injection test	1.2 (1994)	Zoback and Harjes (1997); Baisch and Harjes (2003); Jost et al. (1998)
Bad Urach (Germany)	Stimualtion	1.8 (2002)	Schanz et al. (2003); Tenzer et al. (2004)
Rosemanowes (UK)	Circulation	2 .0 (1987)	Pine and Batchelor (1984); Turbitt et al. (1987)
Soultz-sous-Forêts (France)	Stimul. GPK4	2.3* (2004)	Charléty et al. (2007)
Hellisheidi (Iceland)	Drill- stimul.	2.4 (2003)	Bjornsson (2004)
Unterhaching (Germany)	Circulation	2.4 (2007)	Kraft et al. (2009)
Soultz-sous-Forêts (France)	Stimul. GPK2	2.4* (2000)	Brustle and Stange (2000)
Paralana (Australia)	Stimulation	2.5* (2011)	Hasting et al. (2011); Albaric et al. (2014)
Landau (Germany)	Circulation	2.7* (2009)	Bönnemann et al. (2010)
Latera (Italy)	Injection	2.9 (1984)	Carabelli et al. (1984); Moia (2008)
Soultz-sous-Forêts (France)	Stimul. GPK3	2.9* (2003)	Dorbath et al. (2009)
Lardarello-Travale (Italy)	Circulation	3.0 (1977)	Batini et al. (1980a, 1985)
Torre Alfina (Italy)	Injection	3.0 (1977)	Batini et al. (1980b); Moia (2008)
Basel (Switzerland)	Stimulation	3.4* (2006)	Häring et al. (2008); Deichmann and Ernst (2009)
Monte Amiata (Italy)	Circulation	3.5 (1969)	Batini et al. (1980b); Moia (2008)
Cooper Basin (Australia)	Stimulation	3.7* (2003)	Asanuma et al. (2005); Baisch et al. (2006)
Berlín Field (El Salvador)	Stimulation	4.4* (2003)	Bommer et al. (2006)
The Geysers (CA, USA)	Circulation	4.6 (1982)	Oppenheimer (1986); Rutqvist (2010)

injection operations must be avoided, as public concern may compromise the continuation of the project. One of the most critical issues from a scientific point of view is the lack of a direct correspondence between injection and seismic activity, and specifically the occurrence of such events after the end of injection (Table 1.1), as in the notorious EGS cases of Soultz-sous-Forêts, France (Baria et al., 2005; Evans et al., 2005) and Basel, Switzerland (Häring et al., 2008; Deichmann and Giardini, 2009; Terakawa et al., 2012). The inability of operators to manage these incidents pointed out the incomplete understanding of the processes involved in co- and post-injection felt induced seismicity, which caused a negative impact on the local population. This has drawn the issue into scientific attention.

It is therefore crucial to deepen the understanding of the processes involved in the stimulation and circulation phases, and how they govern seismicity, in order to adequately design and manage the operations (Parotidis et al., 2004; Ellsworth, 2013). The topic is also of paramount relevance in other energy-related activities that involve injection of fluids, such as conventional oil and gas recovery, hydraulic fracturing for shale gas production, CO_2 storage, and waste-water disposal (Fig. 1.1). In fact, seismic activity in the US has increased dramatically in the last

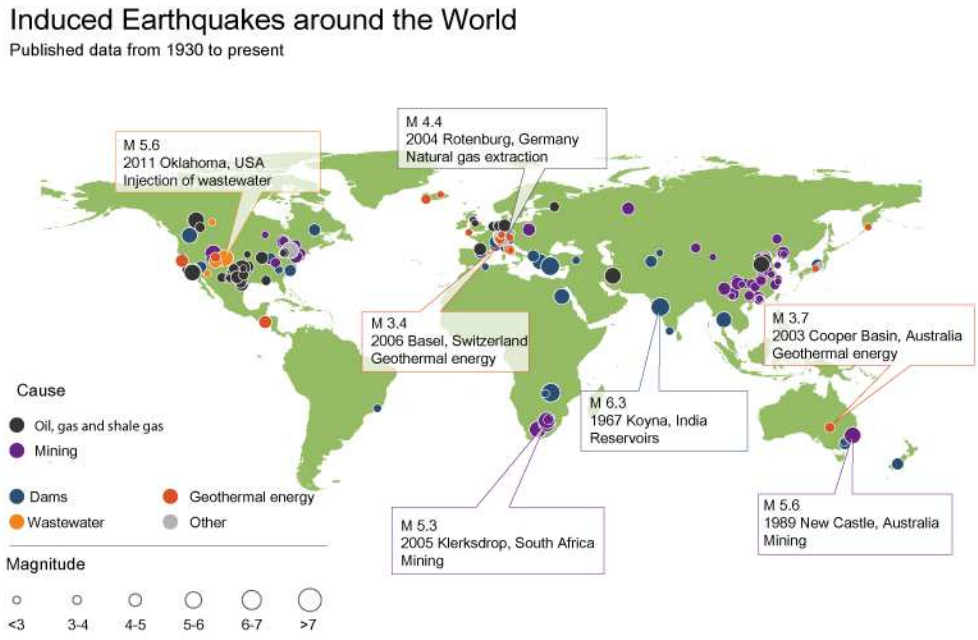

Figure 1.1: World map of seismicity induced by human activities (source: Swiss Seismological Service webpage - http://www.seismo.ethz.ch/).

6 years (Fig. 1.2), because of deep injections of waste-water related to oil and gas operations, which have therefore become a source of concern (Rubinstein and Mahani, 2015).

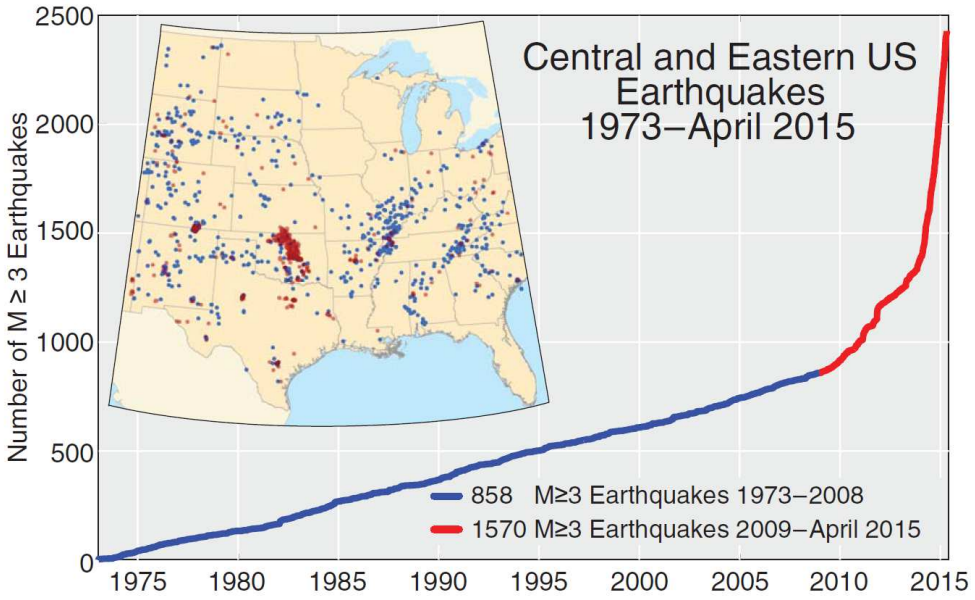

Figure 1.2: Cumulative count of M ≥3 earthquakes in the central and eastern United States from 1973 to April 2015. Two abrupt increases in the earthquake rate occurred in 2009 and 2013. (Inset) Spatial distribution of earthquakes. Red dots represent earthquakes that occurred between 2009 and April 2015, and blue dots represent earthquakes that occurred between 1973 and 2008. Red color becomes brighter when there are more earthquakes in the area. The earthquake rate and distribution of earthquakes changed in 2009. Prior to 2009, earthquakes were spread across the United States. Beginning in 2009 the earthquakes are tightly clustered in a few areas (central Oklahoma, southern Kansas, central Arkansas, southeastern Colorado and northeastern New Mexico, and multiple parts of Texas) (Rubinstein and Mahani, 2015).

Seismicity occurs when shear failure conditions are reached along pre-existing or newly created fractures (Fig. 1.3), which, according to the Mohr-Coulomb failure criterion (Jaeger et al., 2007), occurs when shear stress parallel to the plane exceeds the frictional resistance τ_r

$$\tau_r = c + \mu \cdot \sigma_n' \,, \tag{1.1}$$

where c is cohesion, $\sigma_n' = \sigma_n - p$ is normal effective stress, σ_n is normal total stress, p is fluid pressure, and μ is friction coefficient. Failure triggers irreversible

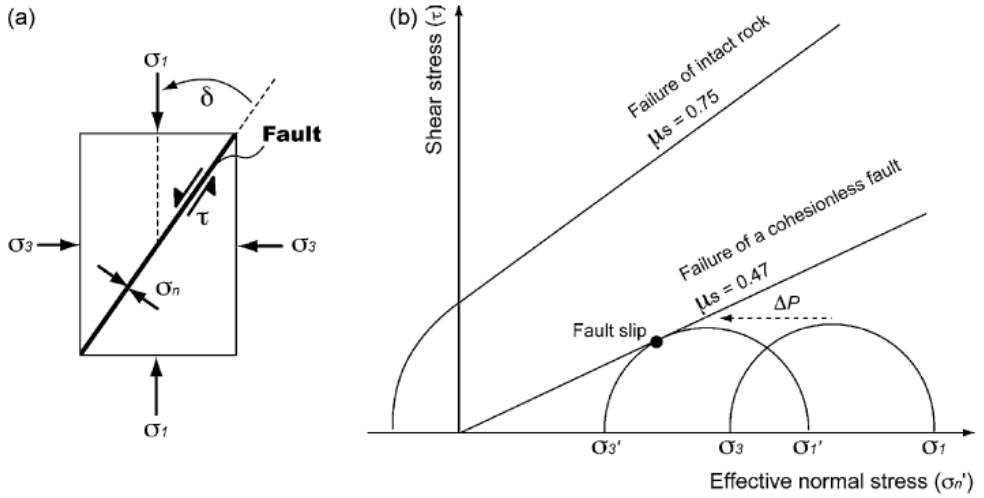

Figure 1.3: (a) Normal and shear stresses resolved on a fault with a given orientation with respect to the principal stresses; (b) Mohr diagram of shear stress (τ) versus normal effective stress (σ'_n) showing how the increasing fluid pressure (Δp) may activate a critically-oriented, cohesionless fault (Cappa and Rutqvist, 2011b).

shear sliding, which not only gives rise to an earthquake, but also permanently increases the fracture aperture (and thus permeability), due to dilation associated to the roughness of the fracture surface (Pine and Batchelor, 1984; Rutledge and Phillips, 2003; Rutqvist, 2015).

In the case of injection-induced seismicity, downhole overpressure is assumed to be the main triggering mechanism, because it reduces the effective stresses and therefore, the frictional resistance (Hubbert and Rubey, 1959; Raleigh et al., 1976; Pearson, 1981). However, the behavior is not trivial because of the hydro-mechanical (HM) coupling, that is, the two-way interaction between hydraulic and mechanical processes. In fact, variation of pressure generates variation of the stress field and deformation of the reservoir, which in turn influences the pressure response (Rutqvist and Stephansson, 2003).

One of the implications of HM coupling is that storage is not a constant in time, locally defined coefficient (Verruijt, 1969), because it depends on deformations throughout the aquifer. The presence of adjacent and surrounding strata may hinder deformations and therefore reduce the storage capacity of the medium, which results in a faster pressure response. This effect should be properly acknowledged in the evaluation of pressure build-up, which is crucial during hydraulic stimulation.

However, pore pressure increase cannot be the only mechanism to induce seismicity because seismic events occur after the stop of injection, when overpressure dissipates. Actually, cooling causes a perturbation of the stress and strain field due to the thermo-mechanical (TM) or thermo-hydro-mechanical (THM) coupling (Majer and Peterson, 2007; Ghassemi, 2012). In fact, the large temperature contrast between the cold injected fluid and the hot reservoir provokes a significant contraction of the reservoir and may significantly affect the local stress field (Segall and Fitzgerald, 1998; Mossop, 2001; Bruel, 2002). Therefore, it is important to identify the respective effects of pressure and temperature, also with respect to the temporal scale, as well as their dependence on controlling parameters, in order to predict the reservoir response.

In the presence of spatial variability of hydraulic and mechanical properties, stresses induced by HM and THM processes are heterogeneous and anisotropic. Non-isotropic stresses may promote or hinder seismicity on a fracture, depending on its orientation and location (Segall, 1989). Moreover, they can cause stress changes even at distances greater than the region of pressure or thermal perturbation (McClure and Horne, 2012). These issues should be investigated in detail because they strongly affect the failure potential both during injection and after shut-in.

A third relevant mechanism that may induce seismicity is shear slip stress transfer. The activation of frictional sliding in the form of microseismic events affects the nearby stress field, which may induce further seismicity (King et al., 1994; Freed, 2005; Schoenball et al., 2012; Catalli et al., 2013). The combination of stress transfer with the above-mentioned coupled processes may help to explain post-injection seismicity.

1.2 Objectives and Thesis Outline

The aim of this Thesis is precisely to deepen the understanding of the processes involved in the operations of hydraulic stimulation and their respective and combined contribution to the triggering of seismicity, both during the injection and after shut-in.

To pursue this goal, two approaches have been adopted. The first approach is analytic. The equations governing the HM and TM couplings are considered

and analytic solutions are derived, which enables to gain insight into the processes and to identify the governing scaling relationships. Moreover, analytical solutions provide a rapid assessment of the system response to an alteration, and can be useful for benchmarking of new numerical codes. The second approach is numeric. The reservoir response to non-isothermal injection is analyzed by means of numerical simulations. This allows taking into account more complicated settings, in terms of geometry and spatial variability of parameters. The resulting alteration of the stress field allows assessing reservoir stability conditions for failure and consequent induced seismicity.

The Thesis is therefore structured as follows:

- Chapter 2 describes the HM coupling and highlights the non-local nature of storage, which depends on the poroelastic response over the whole aquifer. Therefore, analytic solutions are proposed to evaluate the transient pressure response to fluid injection into finite aquifers, acknowledging the HM coupling. This chapter resulted in an article by De Simone and Carrera, which is currently under review in an international scientific journal.

- In Chapter 3 the mechanical response to pressure and temperature variation are analyzed and compared. Practical analytical expressions are presented to calculate hydraulically and thermally driven displacements and stresses for unidirectional and radial geometries. To obtain them, an easy-to-use solution to the transient advection-conduction heat transfer problem is developed, whereas the fluid flow is assumed at steady-state. The contents of this chapter have been included in the publication of De Simone et al. (2017a) in the scientific journal *International Journal of Rock Mechanics and Mining Sciences*.

- Chapter 4 presents the results of numerical simulations of non-isothermal injection into a fracture zone-intact rock system. The HM and THM coupled effects are compared, as well as their effect on the generation of seismicity during the injection period. This study has been published in the scientific journal *Physics and Chemistry of the Earth* by De Simone et al. (2013).

- Chapter 5 deals with the identification of the potential processes leading to post-injection seismicity. Apart from the effects of pressure and temperature perturbations, the stress transfer consequent to shear slip activation is also

considered. The three processes are analyzed separately and in conjunction. Furthermore, their respective and superposed effects on the mechanical stability in the co- and post-injection period are evaluated. The contents of this chapter have been included in an article by De Simone et al., which is currently under review in an international scientific journal.

- Finally, in Chapter 6 the most relevant outcomes of the Thesis are summarized.

In addition, Appendix F summarizes publications and presentations in congresses which are related with the Thesis.

2

Analytical Solutions to Coupled HM Problems to Highlight the Non-Local Nature of Aquifer Storage *

2.1 Introduction

Specific storage is defined as the volume of water released per unit volume of aquifer per unit drop in head (Hantush, 1961). Despite its importance, the very concept of storage has been the subject of an extensive and animated discussion since Meinzer (1928) conceived that idea that "aquifers are compressible and elastic" (Narasimhan, 2006).

Underlying this discussion is the need to distinguish between storage as a "behavior" and storage as a "property" (Hsieh, 2017, personal communication). The term behavior refers to the concept that a drop in head drives the release of water. The term property refers to the measured quantity (or function of other measurable quantities) needed to quantify this behavior. Actually, this study is largely motivated by a third related concept, namely, the way in which this behavior is represented in fluid mass conservation equation. For example, the storage "behavior" is usually represented by the term $S_s \partial h/\partial t$, where S_s is the specific storage coefficient (i.e, "property") and h is head. The initial definition (Jacob, 1940) of storage coefficient equated the behavior and the property by assuming that the pumped aquifer deforms only in the vertical direction. In fact, the initial definition was vertically integrated. Actually, transient flow is coupled to mechanical equilibrium because fluctuations in head (pore pressure)

*This chapter is based on the paper by De Simone and Carrera (2017).

cause changes in effective stresses (Terzaghi, 1923; Biot, 1941) that drive three-dimensional deformations. Therefore, the problem has to be formulated as a coupled hydro-mechanical (HM) one to properly represent these deformations, which altogether eliminates the need for an explicit storage term. While the HM coupled nature of the problem is widely acknowledged, the assumption of vertical deformation has remained common practice by hydrogeologists because solving HM problem is complex. Yet, the issue is not free of debate. Several authors have argued that pumping causes non negligible horizontal displacements (Poland and Davis, 1969; Gambolati, 1974; Bear and Corapcioglu, 1981b; Helm, 1994). The topic is well addressed by Burbey (1999; 2001), who also illustrates the analytic derivation of uniaxial and volumetric storage coefficients starting from elasticity theory and compares the effects of considering or not the horizontal displacements. In fact, Hsieh and Cooley (1995) show that horizontal displacements can be neglected when the under- and/or overlying layers are somewhat stiff.

Whether or not horizontal strains are acknowledged, it is clear that the storage behavior depends on the factors (dimension, flow geometry, boundary conditions, etc.) that control volumetric deformation. In fact, poroelasticity allows one to distinguish between two "extreme" (plus other "intermediate") specific storage concepts (Wang, 2000): (1) unconstrained specific storage, when the total stress remains unaffected by pressure changes, and (2) constrained specific storage, when it is strain what remains unaffected. By itself, the distinction suggests that storage at a point depends on the HM response of the whole aquifer system, which means that storage is non-local.

The implication is that it is not possible to define specific storage as a constant in time, locally defined coefficient (Verruijt, 1969). Non-locality is well known for Darcy's law, where flux at a point depends not only on local permeability, but also on whether such point is well connected to the rest of the aquifer (Renard and De Marsily, 1997; Sanchez-Vila et al., 2006). Ironically, connectivity and Darcy's flux non-locality affect field estimates of storage coefficient by accelerating or delaying the drawdown response to pumping (Meier et al., 1998; Sanchez-Vila et al., 1999). Poroelasticity implies that storage is also non-local because, even if the aquifer is homogeneous, storage is not constant, but depends on deformations throughout the aquifer. Therefore, it is function of space and time (Narasimhan and Kanehiro, 1980). Injection (or pumping) exerts a force over the whole system that causes volumetric deformation and stress redistribution everywhere. In fact,

field observations (Verruijt, 1969) and numerical studies (Hsieh, 1996; Yin et al., 2007; Berg et al., 2011) highlight that the presence of adjacent strata influence the deformation and therefore the pressure response, especially in the case of highly compressible media.

Treating storage as a constant-in-time and locally-defined parameter allows simplifying the flow equation into a linear diffusion equation, which is relatively easy to solve, whereas acknowledging HM coupling requires numerical solution, which hinders its application. Therefore, the question is whether coupling effects are relevant. Conventional hydrogeology disregards HM coupling for the vast majority of problems, except when interpreting drawdowns at aquitards adjacent to pumped aquifers (Berg et al., 2011). However, the study of low permeability formations for enhanced geothermics, waste disposal, CO_2 storage or shale gas extraction grants revising the concepts, which is the objective of our work. To this end, we first revise the various definitions of specific storage as a property and then analyze the non-local nature of the storage term by means of analytic solutions to the HM problem of flow injection into one-dimensional and cylindrical two-dimensional laterally finite aquifers. These solutions highlight that the storage term in the fluid conservation equation becomes non-local (i.e., the value of the storage at a point depends on heads elsewhere) when the mechanical equilibrium equation is substituted into the flow equation.

2.2 Storage in deformable porous media

2.2.1 Local storage

Water released by a porous medium in response to a drop in pressure comes from (1) the expansion of water, characterized by its compressibility, β, (2) the growth of grains volume, characterized by the compressibility of the solid grains, $(1/Ks)$, and (3) the reduction in porosity associated to the rearrangement of grains and driven by the increase in effective compressive stress, characterized by the porous matrix compressibility, α. Therefore, it is most natural to write the specific storage as (de Marsily, 1981)

$$S_s = \phi\beta + \frac{a-\phi}{K_s} + \alpha = \beta_T + \alpha \quad , \tag{2.1}$$

where ϕ is porosity and $a = 1 - (K/K_s)$ is the Biot-Willis coefficient, with K representing the Bulk modulus. Note that S_s in Eq. (2.1) is usually multiplied

by ρg (where ρ is fluid density and g is the acceleration of gravity), to express the response to change in head. However, we will be working with pressure. K_s is usually so large, compared to β or α, that $(a-\phi)/K_s$ is normally neglected. The compressibilities of water and solid grains, grouped into the coefficient β_T, are local by definition. Difficulties arise with the compressibility of the porous matrix α because it is defined in terms of effective stresses and only indirectly related to head fluctuations, so that further assumption are required. In order to properly define α, we have to introduce the Hooke's law of elasticity, which relates stresses and strains

$$\boldsymbol{\sigma'} = 2G\,\boldsymbol{\varepsilon} + \lambda\,\varepsilon_{vol}\,\mathbf{I} \quad , \tag{2.2}$$

where $\boldsymbol{\sigma'}$ is the change in effective stress tensor, $G = E/(2(1+\nu))$ and $\lambda = E\nu/((1+\nu)(1-2\nu))$ are the shear and Lamé moduli, respectively, E is Young's modulus, ν is Poisson ratio, $\mathbf{I}$ is the identity matrix, $\boldsymbol{\varepsilon} = 1/2\left[\nabla\mathbf{u} + (\nabla\mathbf{u})^T\right]$ is the strain tensor, $\epsilon_{vol} = \nabla\cdot\mathbf{u}$ is the volumetric strain and $\mathbf{u}$ is the displacements vector. According to Eq. (2.2), it is easy to express the compressibility (α_σ) against mean effective stress σ'_m as

$$\alpha_\sigma = \frac{\varepsilon_{vol}}{\sigma'_m} = \frac{3}{2G+3\lambda} = \frac{1}{K} \quad . \tag{2.3}$$

This expression for compressibility is also valid under conditions of plane strain with respect to one or two directions (i.e., $\varepsilon_i = 0$).

Actually, instead of α_σ, the compressibility against pressure α_p (i.e., volumetric deformation caused per unit change in water pressure) is usually introduced in Eq. (2.1). To this end, poroelasticity must be considered, which relates variation of effective stress to variation of pressure, according to $\boldsymbol{\sigma'} = \boldsymbol{\sigma} + ap\mathbf{I}$, where $\boldsymbol{\sigma}$ is the total stress tensor and tensile stress is assumed positive. The compressibility against pressure can be derived by assuming that effective stress changes equal ap in the directions along which the medium is free to deform, which leads to a general α_{p_n} of the form

$$\alpha_{p_n} = \frac{\varepsilon_{vol}}{p} = \frac{a}{2G/n+\lambda} \quad , \tag{2.4}$$

where n is the number of non-zero strain directions, or rather, the number of directions in which total stress is assumed to remain unchanged. It is easily veri-

fied that compressibility against pressure is equivalent to compressibility against stress (i.e., $\alpha_p = \alpha_\sigma$) when total stress remain unchanged in the three directions ($n = 3$) because a is often assumed to be 1. On the other hand, in the case of uniaxial strain, the definition of specific storage involves α_{p1}, which corresponds to the traditional Jacob's (1940) definition that assumes exclusively vertical deformation and no change in vertical total stress (i.e., $\sigma_z = 0; \varepsilon_x = \varepsilon_y = 0$).

2.2.2 Non-local storage

The assumption of zero total stress variation may not be valid and the full HM problem has to be solved. The problem involves fluid mass conservation

$$\beta_T \frac{\partial p}{\partial t} + a \frac{\partial \epsilon_{vol}}{\partial t} = \nabla \frac{k}{\mu} \nabla p \,, \tag{2.5}$$

and mechanical equilibrium, which, together with constitutive laws (e.g., Hooke's and Biot's law), yields (Jaeger et al., 2007)

$$G \nabla^2 \mathbf{u} + (G + \lambda) \nabla (\nabla \cdot \mathbf{u}) = \nabla (ap) \,. \tag{2.6}$$

These two equations have to be solved together with appropriate boundary and initial conditions. It is useful to reduce the system of Eq. (2.6) to one equation, by applying the divergence operator (Verruijt, 1969), which gives

$$(2G + \lambda) \nabla^2 \varepsilon_{vol} = a \nabla^2 p \,. \tag{2.7}$$

Integration of the latter gives

$$(2G + \lambda) \varepsilon_{vol} = ap + f \quad , \tag{2.8}$$

where $f(\mathbf{x}, t)$ is a harmonic function (i.e., such that $\nabla^2 f = 0$). In general, calculating f requires solving the full problem. But relevant approximations can be obtained in specific cases. For example, in the case of constant total stress, comparing Eqs. (2.8) and (2.4) leads to

$$f = \Big[(2G + \lambda) \alpha_{p_n} - a \Big] p = \frac{(n-1)(1-2\nu)}{1 + (n-2)\nu} \, ap \,. \tag{2.9}$$

In general, function f depends on the shape and dimension of the medium and on the boundary conditions (Gambolati, 1974).

Introduction of (2.8) into (2.5) gives

$$\left(\beta_T + \frac{a^2}{2G+\lambda}\right)\frac{\partial p}{\partial t} + \frac{a}{2G+\lambda}\,\frac{\partial f}{\partial t} = \nabla\,\frac{k}{\mu}\nabla p\;, \tag{2.10}$$

where the temporal derivative of f is part of the storage term and determines its non-locality. Therefore, the storage term results different from the form adopted in the classical groundwater hydrology (Eq. (2.1)). This alteration should be considered if two-way hydro-mechanical coupling is analyzed.

Furthermore, in terms of mean stress, volumetric deformation is defined by $\varepsilon_{vol} = \alpha_\sigma(\sigma_m + ap)$, which can be substituted into Eq. (2.5) yielding

$$\left(\beta_T + a^2\alpha_\sigma\right)\frac{\partial p}{\partial t} + a\alpha_\sigma\frac{\partial \sigma_m}{\partial t} = \nabla\,\frac{k}{\mu}\nabla p\;. \tag{2.11}$$

If the latter equation is compared with Eq. (2.10), it can be again derived that f depends on the geometry (in order to transform $a/(2G+\lambda)$ into α_σ (Eq. (2.3)) and on the total stress variation, which may depend not only on the mechanical boundary conditions (restraints), but also on the distribution of the perturbation. Note that the expression $a\alpha_\sigma/(\beta_T + a^2\alpha_\sigma)$ defines the Skempton coefficient B (Detournay and Cheng, 1993; Rice and Cleary, 1976; Zimmerman, 2000), which relates the variation of pressure with the variation of total stress under undrained condition (i.e., $p = B\sigma_m$).

Eq. (2.10) is not very satisfying, because the parameter f is unknown. We consider below some simple cases that allow us to define f and thus gain insight into the variable, and non-local, nature of the storage term. In particular, we consider continuous injection into homogeneous and finite cylindrical and one-dimensional domains. Other cases can be solved by means of the proposed methodology.

2.3 One-dimensional finite domain

We first analyze the simplest case of unidirectional (linear) flow within a finite domain of dimension L with displacements allowed only in the flow direction

$0 < x < L$, i.e., $\varepsilon_y = \varepsilon_z = 0$ and $\partial p/\partial y = \partial p/\partial z = 0$. It can be shown (Appendix A) that the volumetric strains ($\varepsilon_{vol} = \varepsilon_x$), when displacement is constrained at $x = 0$ and $x = L$, is expressed by

$$\varepsilon_{vol}(x,t) = \frac{a}{2G+\lambda}\left[p(x,t) - \frac{1}{L}\int_0^L p(x,t)dx\right] = \frac{a}{2G+\lambda}\Big[p(x,t) - \overline{p}(t)\Big], \quad (2.12)$$

where $\overline{p}$ indicates the spatial average of pressure. Therefore fluid mass conservation becomes

$$(\beta_T + a\alpha_{p1})\,\frac{\partial p(x,t)}{\partial t} - a\alpha_{p1}\,\frac{\partial\,\overline{p}(t)}{\partial t} = \frac{k}{\mu}\,\frac{\partial^2 p(x,t)}{\partial x^2}\,, \quad (2.13)$$

where we have substituted $a/(2G+\lambda)$ with α_{p1}, defined in Eq. (2.4).

Comparing this equation with Eq. (2.10) yields that f is given by the spatial average of pressure, i.e., $f = -a\overline{p}(t)$. Therefore, the storage term is not just proportional to the local pressure fluctuations, but also to the mean pressure fluctuation along the whole domain.

To find the solution of Eq. (2.13), we define

$$p^*(x,t) = p(x,t) + \theta\,\overline{p}\,(t) \quad , \quad (2.14a)$$

$$S_{s_1} = \beta_T + a\alpha_{p1} \quad , \quad (2.14b)$$

$$\theta = -\frac{a\alpha_{p1}}{S_{s_1}} \quad , \quad (2.14c)$$

$$D = \frac{k/\mu}{S_{s_1}} \quad . \quad (2.14d)$$

Using p^* and considering that the gradient of the spatial average is zero, Eq. (2.13) can be written as

$$\frac{\partial p^*(x,t)}{\partial t} = D\,\nabla^2 p^*(x,t)\,. \quad (2.15)$$

This equation is identical to the traditional flow equation, which can be solved for different problems (e.g., Carslaw and Jaeger, 1959). The boundary condition for $p^*(x,t)$ is the same as for $p(x,t)$ at the injection point $x = 0$, where q_0 is injected, though not at the outer boundary $x = L$. The solution in terms of

pressure can then be found by means of Eq. (2.14a), where $\overline{p}(t)$ depends on the hydraulic boundary conditions at the outer boundary.

2.3.1 Constant pressure at the outer boundary

In this case, the boundary condition at the outer boundary is

$$p^*(L,t) = \theta\,\overline{p}(t)\,, \tag{2.16}$$

which is inconvenient because it depends on the solution. Instead, we obtain a supplementary condition by operating the spatial average of p^*

$$\overline{p^*}(t) = \frac{1}{L}\int_0^L p^*(x,t)dx = (1+\theta)\,\overline{p}(t) = \frac{1+\theta}{\theta}\,p^*(L,t)\,. \tag{2.17}$$

Once p^* solution is obtained (Appendix B), Eqs. (2.14a) and (2.16) lead to

$$p(x,t) = p^*(x,t) - p^*(L,t)\,, \tag{2.18}$$

which allows us to define the solution to the problem in terms of p (Appendix B).

The problem can be greatly simplified if the compressibility of solid grains and water, β_T, is assumed much smaller than the compressibility of the porous medium and neglected, so that $\theta = -1$ and $D = (k/\mu)/\alpha_{p1}$, where Biot-Willis coefficient a has been taken equal to 1, because the solid grains are being considered incompressible (Detournay and Cheng, 1993). With these assumptions, p^* simply represents the fluctuation with respect to the spatial average, i.e., $p(x,t) = \overline{p}(t) + p^*(x,t)$, and the supplementary condition (Eq. (2.17)) becomes

$$\frac{1}{L}\int_0^L p^*(x,t)dx = 0\,, \tag{2.19}$$

which is logical, because the spatial average of the fluctuation is zero by definition.

After solving for p^* (Appendix B) and application of Eq. (2.18), the solution for $p(x,t)$ becomes:

$$p(x,L,t) = p_{trad}(x,L/2,t) + \overline{p}(t) \quad , \tag{2.20}$$

where $p_{trad}(x,t)$ is the well-known solution to the traditional (i.e., without HM coupling) problem of 1-D injection into a finite domain (Carslaw and Jaeger, 1959)

$$p_{trad}(x,L,t) = \frac{q_0}{k/\mu}\sqrt{4Dt}\sum_{m=0}^{\infty}(-1)^m\Big[A(2L,x) - A(2L,2L-x)\Big]\,, \qquad (2.21)$$

whereas

$$\overline{p}(t) = p_{trad}(0,L/2,t) \quad , \qquad (2.22)$$

with $A(\Gamma,\psi) = \text{ierfc}\left[(\Gamma m + \psi)/\sqrt{4Dt}\right]$ and ierfc indicates the integral error function, defined as $\text{ierfc}(y) = \exp(-y^2)/\sqrt{\pi} - y\,\text{erfc}(y)$. This series converges very fast because it is alternate and because the exponential term in A decays rapidly as m increases. This is especially true for small time, but truncation at $m = 2$ is sufficient even for large time, as shown by comparison with numerical solutions (Fig. 2.1).

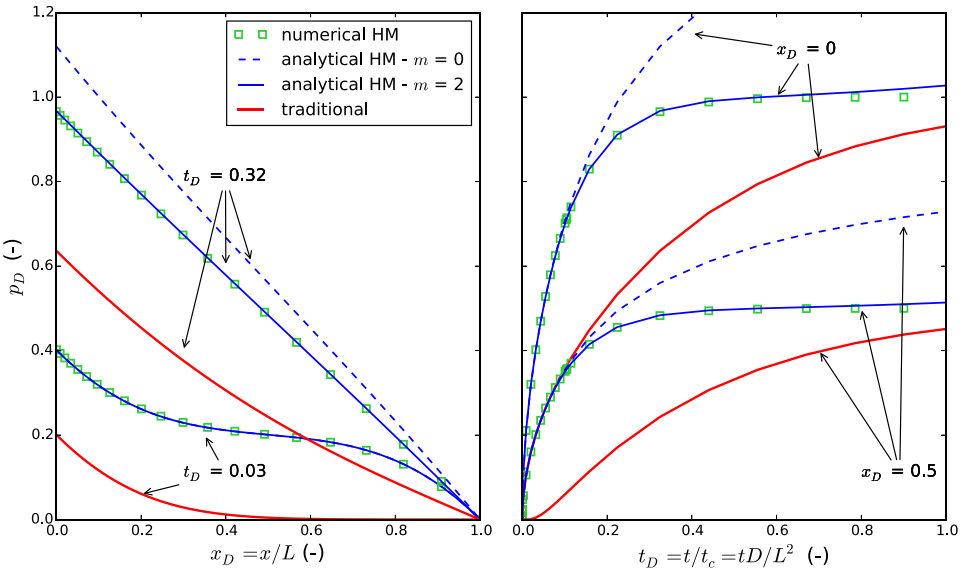

Figure 2.1: Comparison between traditional and hydromechanical solutions for the one-dimensional domain with constant pressure at the outer boundary. Also shown are the results of truncating the series after m=0 and m=2, against results of numerical simulations. Results are normalized respect to $q_0 L\mu/k$, which is the steady state pressure at $x = 0$.

The HM solution corresponds to the traditional solution for half the domain

plus the spatial average of pressure $\overline{p}$, given by the traditional solution for half the domain at $x = 0$. At early time ($t < 0.1t_c$, where $t_c = L^2/D$ is the characteristic time of the problem) the extension of the domain is not relevant, thus the HM effects implies raising pressure by a constant ($\overline{p}$) within the whole domain, except near the outer boundary, where pressure was prescribed to be zero (Figs. 2.1 and 2.2). Note that the drop in pressure, with respect to the constant $\overline{p}$, near this boundary is identically symmetric to the rise near the inflow (Fig. 2.1).

For time greater than $0.1t_c$, the outer boundary starts to significantly affect the solution within the whole domain. Thus, the difference between solutions is given not only by $\overline{p}$, but depends on the position, being greater in the vicinity of the injector and smaller in the vicinity of the constant pressure boundary (Fig. 2.2). At time greater than the characteristic time t_c the difference tends to zero, because both solutions tend to the steady state and the effect of pressure derivatives becomes negligible.

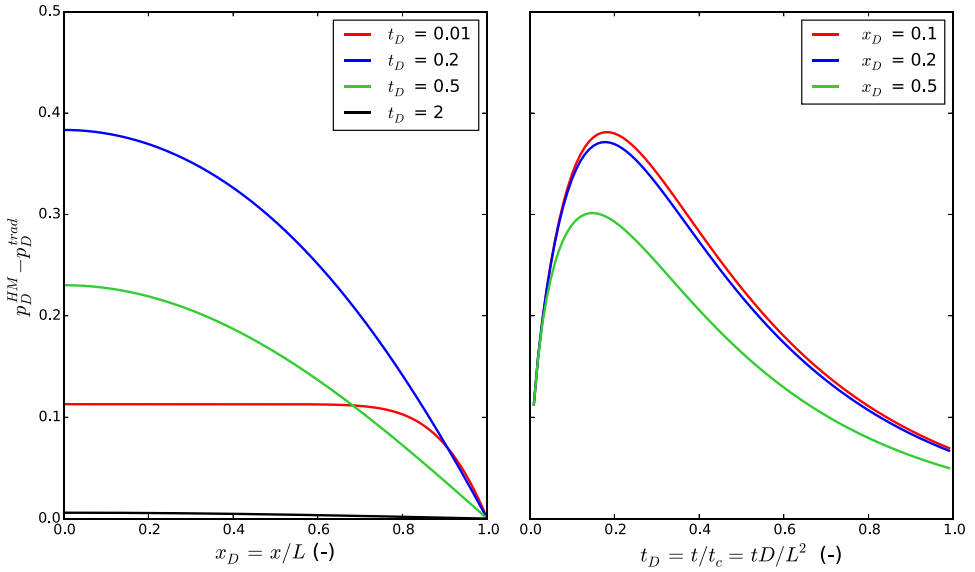

Figure 2.2: Difference between hydro-mechanical and traditional solutions for the one-dimensional domain with constant pressure at the outer boundary. Results are normalized respect to $q_0 L\mu/k$, which is the steady state pressure at $x = 0$.

2.3.2 No flow at the outer boundary

When a no flow boundary condition is imposed at $x = L$, the problem in terms of p^* is subject to the same BCs than the traditional flow problem at both

boundaries (Appendix B). However, the value of the spatial average $\overline{p}$ is unknown. It can be found by operating the spatial average of Eq. (2.13), which gives

$$\beta_T \frac{\partial \overline{p}}{\partial t} = \frac{1}{L}\left(q_0 - q_L\right) \ , \tag{2.23}$$

where q_0 and q_L represents the flux at $x = 0$ and $x = L$, respectively.

This equation highlights that the spatial average of the water storage is exclusively due to the compressibility of water and solid grains (β_T), which therefore cannot be disregarded. This implies that parameter θ cannot be equal to -1. In our case, with constant q_0 and zero q_L, the spatial average is therefore defined by

$$\overline{p}(t) = \frac{q_0\, t}{\beta_T L} \ , \tag{2.24}$$

which allows to find the solution in terms of $p(x,t)$

$$p(x,t) = p_{trad} - \theta \frac{q_0\, t}{\beta_T L} \quad , \tag{2.25}$$

where p_{trad} is the traditional solution given by (Carslaw and Jaeger, 1959)

$$p_{trad}(x,t) = \frac{q_0}{k/\mu}\sqrt{4Dt}\sum_{m=0}^{\infty}\Big[A(2L,x) + A(2L,2L-x)\Big] \tag{2.26}$$

and $A(\Gamma,\psi)$ has been defined above.

Solution (2.25) can be normalized respect to $q_0 L\mu/k$, which, together with eqs. (2.14c) and (2.14d), gives

$$p_D(x,t) = p_{trad_D}(x,t) + \frac{a\alpha_{p1}}{\beta_T}\, t_D \tag{2.27}$$

where p_D and p_{trad_D} are the dimensionless form of p and p_{trad} and $t_D = tD/L^2$. This expression highlight that the term $a\alpha_{p1}/\beta_T$ is the governing dimensionless parameter for the case of no flow at the outer boundary.

Figure 2.3 displays the comparison between the traditional and the HM solutions, whose validity is tested against numerical solutions. It is clear that the two solutions diverge by the spatial average $\overline{p}$, which is constant in space and

increases linearly with time and with the parameter $a\alpha_{p1}/\beta_T$. This latter parameter is assumed approximately equal to 150 in this example, which means that θ is slightly smaller than 1.

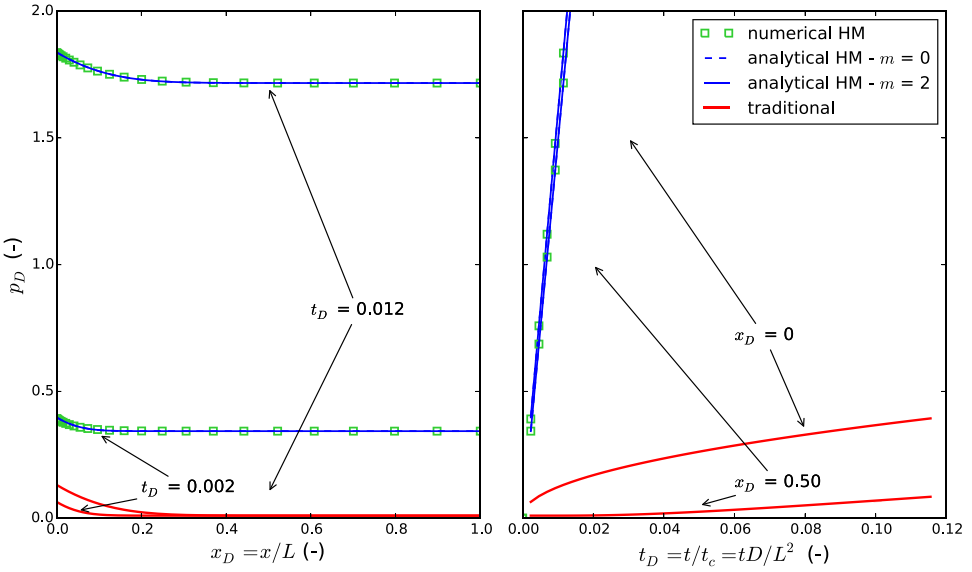

Figure 2.3: Comparison between traditional and hydromechanical solutions for the one-dimensional domain with no flow outer boundary. Also shown are the results of truncating the series after m=0 and m=2, against results of numerical simulations. Results are normalized respect to $q_0 L\mu/k$.

2.4 Cylindrical finite domain

We now consider the more general case of radial flow within a finite aquifer $r_0 < r < R$, adopting cylindrical coordinates r, θ, z and axial symmetry around the z-axis. For the sake of simplicity, we consider the cases of plane strain or plain stress in the z direction, i.e., $\varepsilon_z = 0$ and $\sigma_z = \tau_{rz} = \tau_{\theta z} = 0$, respectively. The former may correspond to an aquifer with infinite extension in the z direction. The latter represents a thin aquifer confined between two soft layers, which cannot resist shear stress (Verruijt, 1969).

The expression for the volumetric strains, for both plane stress and plane strain, is (Appendix C)

$$\varepsilon_{vol} = \alpha_{p_n} \left[p(r,t) + g_1 \, 2C(t) \right] \quad , \tag{2.28}$$

where g_1 is 1 for plane strain and $(1-2\nu)/2/(1-\nu)$ for plane stress and α_{p_n} is the compressibility against pressure (Eq. (2.4)) with n=1 for plane strain and n=2 for plane stress. The latter may surprise because n was defined as the number of non-zero strain directions (which is actually 2 for plane strain and 3 for plane stress) or the number of directions along which total stress does not change (0 for plane strain, 1 for plane stress). In reality, Eq. (2.4) was derived by assuming that either strain or total stress were zero along three orthogonal directions, a condition that is not met in this case. The actual α_{p_n} are derived from the axial symmetry assumption and the equilibrium equations (Appendix C). In the resulting α_{p_n}, however, n corresponds to the number of non-zero displacements, rather than to the non-zero strains.

Constant C is zero for infinite aquifer, but depends on the mechanical boundary conditions for finite domain. We consider the two possibilities of zero displacements ($u_r = 0$) or zero stress ($\sigma_r = 0$) at the external radius $r = R$. They lead to different expressions for the constant C that, in the case of small inner radius r_0, can be summarized into

$$2C = g_2 \frac{2}{R^2} \int_{r_0}^{R} rp(r,t)dr = g_2 \, \overline{p}(t) \quad , \tag{2.29}$$

where g_2 is -1 (both plane stress and plane strain) for zero lateral displacements and $(1-\nu)/(1+\nu)$ (plane stress) or $1-2\nu$ (plane strain) for zero increase in total stress, as shown in Appendix C.

Therefore, fluid mass conservation (Eq. (2.10)) is expressed by

$$(\beta_T + a\alpha_{p_n}) \frac{\partial p(x,t)}{\partial t} + a\alpha_{p_n} g_1 \, g_2 \, \frac{\partial \overline{p}(t)}{\partial t} = \frac{k}{\mu} \frac{1}{r} \frac{\partial}{\partial r} \left(r \frac{\partial p(r,t)}{\partial r} \right) , \tag{2.30}$$

which shows again the non-local nature of the storage term. Similarly to the one-dimensional case, we define

$$p^*(r,t) = p(r,t) + \theta \, \overline{p}(t) \quad , \tag{2.31a}$$

$$S_{s_r} = \beta_T + a\alpha_{p_n} \quad , \tag{2.31b}$$

$$\theta = \frac{a\alpha_{p_n} g_1 g_2}{S_{s_r}} \quad , \tag{2.31c}$$

$$D = \frac{k/\mu}{S_{s_r}} \quad , \tag{2.31d}$$

which allows us to transform Eq. (2.30) into the well-known diffusion equation in radial coordinates

$$\frac{\partial p^*(r,t)}{\partial t} = D\,\frac{1}{r}\,\frac{\partial}{\partial r}\left(r\,\frac{\partial p^*(r,t)}{\partial r}\right)\,. \tag{2.32}$$

The boundary conditions for this problem are identical to the ones of the traditional flow problem at the injection boundary $r = r_0$, where Q_0 is injected, but differ at the outer boundary $r = R$.

2.4.1 Constant pressure at the outer boundary

As for the one-dimensional case, given the inefficiency of the outer BC

$$p^*(R,t) = \theta\,\overline{p}(t)\,, \tag{2.33}$$

we define a supplementary condition by operating the spatial average of p^*, which results

$$\overline{p^*}(t) = \frac{2}{R^2 - r_0^2}\int_{r_0}^{R} r\,p^*(r,t)dr = (1+\theta)\,\overline{p}(t) = \frac{1+\theta}{\theta}\,p^*(R,t)\,. \tag{2.34}$$

Once p^* solution has been found (Appendix D), Eqs. (2.31a) and (2.33) lead to

$$p(r,t) = p^*(r,t) - p^*(R,t)\,, \tag{2.35}$$

which allow us to define the solution in terms of p in the Laplace domain

$$\widehat{p}(r,s) = C_1\Big[I_0\,(r\eta) - I_0\,(R\eta)\Big] - \frac{2}{\pi}C_2\Big[K_0\,(r\eta) - K_0\,(R\eta)\Big]\,, \tag{2.36}$$

where constants C_1 and C_2 depend on the hydraulic boundary conditions (Appendix D).

Again, the problem can be greatly simplified disregarding the compressibility of water and solid grains, β_T, with respect to the compressibility of the porous medium, which also implies $a = 1$. In this case, the values of the parameter θ and D are the ones given in Table 2.1.

Table 2.1: Values of the parameters θ and D in the case in which compressibility of the solid grains and that of water are disregarded.

		Plane stress	**Plane strain**
D		$\dfrac{k/\mu}{1/(G+\lambda)}$	$\dfrac{k/\mu}{1/(2G+\lambda)}$
θ	**Constrained**	$-\dfrac{1-2\nu}{2(1-\nu)}$	-1
	Unconstrained	$\dfrac{1-2\nu}{2(1+\nu)}$	$1-2\nu$

In the simpler case of plane strain and zero displacement at the outer boundary, $p^*(r,t)$ represents the fluctuation of pressure with respect to the spatial average, i.e., $p(r,t) = \overline{p}(t) + p^*(r,t)$. Therefore the supplementary condition (Eq. (2.34)) becomes $\overline{p^*}(t) = 0$, which is logical, since the spatial average of the fluctuation is zero by definition.

In this case the solution for pressure in the Laplace domain is

$$\widehat{p}(r,s) = \frac{Q_0}{2\pi k/\mu}\,\frac{1}{s}\left\{\frac{RK_1(R\eta) - r_0K_1(r_0\eta)}{RI_1(R\eta) - r_0I_1(r_0\eta)}\right. \\ \left.\Big[I_0(r\eta) - I_0(R\eta)\Big] + K_0(r\eta) - K_0(R\eta)\right\}, \quad (2.37)$$

where I_m and K_m are modified Bessel's functions of first and second kind, of order m, respectively, and $\eta = \sqrt{s/D}$.

The solution to the conventional problem in the Laplace domain is instead given by (Carslaw and Jaeger, 1959; Chen, 1984; Verruijt, 2013)

$$\widehat{p}_{trad}(r,s) = \frac{Q_0}{2\pi k/\mu}\,\frac{1}{s}\left[-\frac{K_0(R\eta)}{I_0(R\eta)}\,I_0(r\eta) + K_0(r\eta)\right]. \quad (2.38)$$

Numerical inversion of this Laplace transform solution is compared with results of discrete numerical methods and with the traditional solution in Fig. 2.4.

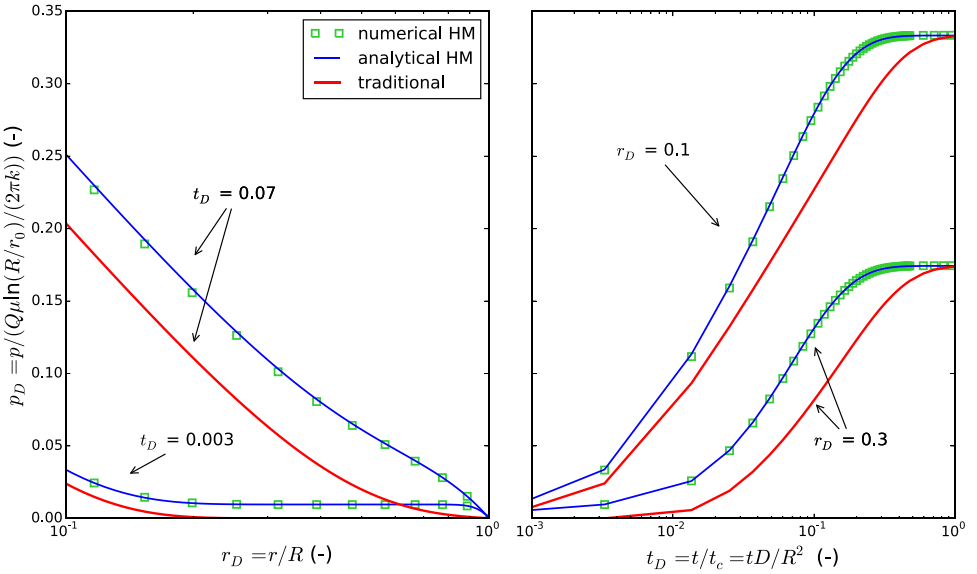

Figure 2.4: Comparison between traditional and hydromechanical solutions for the cylindrical domain with constant pressure outer boundary, plane strain and zero displacement at the outer boundary. Also shown are the results of numerical simulations. Pressures are normalized with respect to $Q_0\mu \ln(R/r_0)/(2\pi k)$, which is the steady state pressure at $r = r_0$.

The behavior is similar to the one-dimensional case (Fig. 2.2) in that pressure builds up immediately throughout the domain due to the horizontal stress caused by the push of injected water, although the understanding of the analytic expressions is less intuitive. For early times ($t < 0.1t_c$, with $t_c = R^2/D$), the traditional solution is Theis'. The HM overpressure is larger by the same amount over the domain ($\overline{p}$), except near the outer boundary (Fig. 2.5). For times greater than 0.1 t_c, the difference between solutions varies with space, being greatest near the injector. This behavior is consequence of the influence of the outer boundary, which tends to reduce the pressure increase. In fact, the deviation respect to the traditional solution is maximum at around $t = 0.2t_c$. For time greater than t_c, both solutions converge to the steady state (Thiem) solution.

The pressure field predicted by the HM solution is different from the traditional one also when the outer boundary is free to deform (Fig. 2.6). The deviation is smaller than in the constrained case and it is negative because the medium deforms more than calculated by means of compressibility, as also expressed by Eqs. (C.4) and (C.6). The negative deviation is quite surprising because it implies that injection may cause a drop in pressure. Actually, the drop

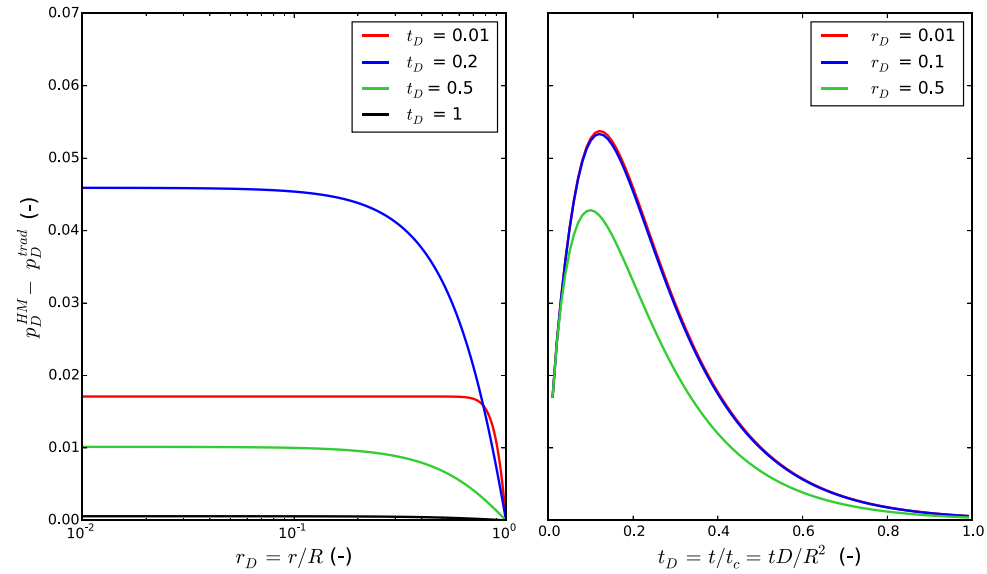

Figure 2.5: Difference between hydro-mechanical and traditional solutions for the cylindrical domain in plane strain with constrained outer boundary. Results are normalized respect to $Q_0\mu\ln(R/r_0)/(2\pi k)$, which is the steady state pressure at $r = r_0$. A value of 0.3 is assumed for the Poisson's ratio.

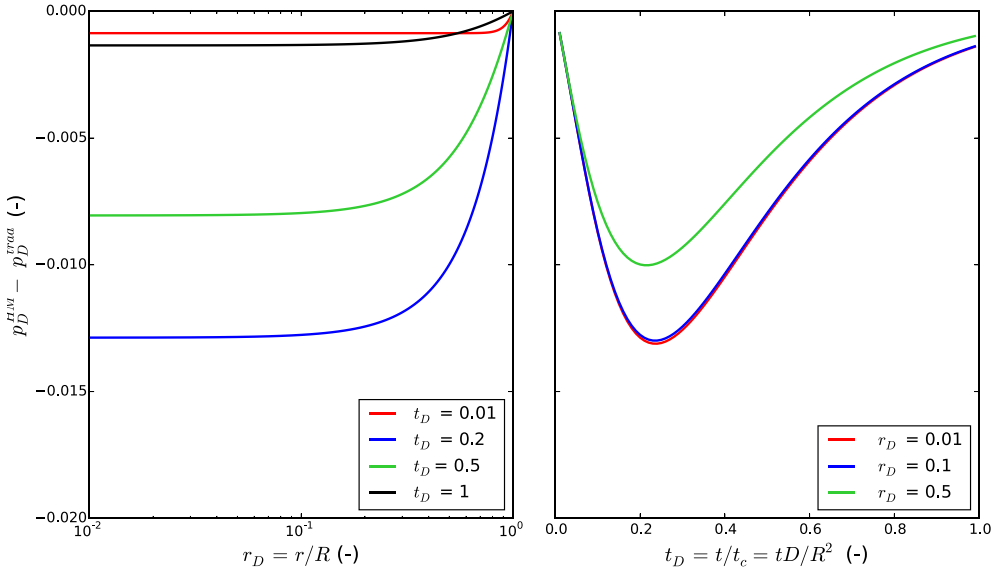

Figure 2.6: Difference between hydro-mechanical and traditional solutions for the cylindrical domain in plane strain with unconstrained outer boundary. Results are normalized respect to $Q_0\mu\ln(R/r_0)/(2\pi k)$, which is the steady state pressure at $r = r_0$. A value of 0.3 is assumed for the Poisson's ratio.

only occurs ahead of the injection pressure cone and reflects that, since radial displacements are unhindered, the medium tends to expand laterally by the push of water near the injection point. We do not know of any case where such drop has been reported, which probably reflects the small magnitude of the drop and the highly idealized conditions of this case. In real aquifers, horizontal displacements would be hindered by shear stresses from the adjacent formations (Hsieh, 1996). However, the behavior is similar to other observed reverse water-level fluctuations, such as the Noordbergum effect (Verruijt, 1969) and the Rhade effect (Langguth and Treskatis, 1989).

The behavior in the case of plane stress (constrained and unconstrained cases) is similar to that observed for the plane strain, but scaled according to the values of parameter θ (Table 2.1), which are around 1/3 of the corresponding plane strain θ.

In general, the deviation respect to the traditional solution is largest in the case of plane strain with constrained outer boundary, whereas it is smallest in the case of plane stress with unconstrained outer border. This result reflects that the HM additional pressure variation is inversely proportional to the possibility of the medium to deform. In general, HM coupling can be disregarded when the medium is free to deform.

2.4.2 No flow at the outer boundary

The case of no flow at the outer boundary is similar to the one-dimensional case in that the solution for p^* is completely defined by the BCs and corresponds to the traditional solution of the hydraulic problem p_{trad} (Appendix D). To find the HM solution in terms of pressure, the spatial average $\overline{p}$ is obtained by averaging Eq. (2.30) and taking into account Eqs. (2.31), which yields

$$S_{s_r}\,(1+\theta)\,\frac{\partial \overline{p}}{\partial t} = \frac{Q_0 - Q_R}{\pi(R^2 - r_0^2)}\,, \tag{2.39}$$

where Q_0 and Q_R represent the inflow at $r = r_0$ and the outflow at $r = R$, respectively. In our case, with constant Q_0 and zero Q_R, the spatial average is

$$\overline{p}(t) = \frac{1}{S_{s_r}\,(1+\theta)}\;\frac{Q_0\,t}{\pi(R^2 - r_0^2)}\,. \tag{2.40}$$

Introduction of Eq. (2.40) into Eq. (2.31a) returns the HM solution for pressure, which normalized respect to $Q_0\mu/(\pi k)$ and taking into account Eq. (2.31d), becomes

$$p_D = p_{trad_D} - \frac{\theta}{1+\theta}\, t_D \,, \tag{2.41}$$

where $t_D = tD/(R^2 - r_0^2)$ and p_D and p_{trad_D} are the dimensionless expressions of p and p_{trad}. It is clear that the dimensionless term $-\theta/(1+\theta)$ governs the discrepancy between traditional and HM solutions. In the plane strain case with constrained outer boundary this parameter corresponds to $a\alpha_{p_1}/\beta_T$, like in the case of one-dimensional domain. Note that the values of θ given in Table 2.1 do not apply to this case, in which we cannot disregard β_T.

The solution to the traditional problem is given in the Laplace space by (Carslaw and Jaeger, 1959)

$$\widehat{p}_{trad}(r,s) = \frac{Q_0}{2\pi k/\mu}\,\frac{1}{s}\left[\frac{K_1(R\eta)}{I_1(R\eta)} I_0(r\eta) + K_0(r\eta)\right] . \tag{2.42}$$

Therefore the solution in terms of pressure can be written in the Laplace domain as (Appendix D)

$$\widehat{p}(r,s) = \widehat{p}_{trad}(r,s) + \frac{1}{S_{s_r}(1+\theta)}\,\frac{Q_0}{\pi(R^2 - r_0^2)}\,\frac{1}{s^2} \,. \tag{2.43}$$

Similar to the one-dimensional domain, it is apparent that the two solutions diverge by the spatial average $\overline{p}$, which is constant in space and increases linearly with time (Eq. (2.40)). Therefore, when long-term continuous injection is performed in bounded aquifer, ignoring the HM coupling implies a great underestimation of the pressure variation.

2.5 Sensitivity to parameters

HM coupling acknowledge that pressure gradients produce deformations throughout the flow domain, which causes a deviation with respect to the hydraulic solution because storage is modified respect to the traditional formulation by an amount proportional to the spatial average $\overline{p}$ (Eqs. (2.13) and (2.30)), which

would tend to increase with time and to reduce with the domain dimension (Eqs. (2.24) and (2.40)). However, $\overline{p}$ is strongly affected by the boundary conditions.

In the case the outer BC is of no flow, the deviation from the traditional solution increases with time and decreases with the domain extension, as apparent in Eqs. (2.25) and (2.43).

The behavior is different and more complex in the case of prescribed pressure at the outer boundary, which limits the increase of pressure, and therefore of $\overline{p}$. Figure 2.7 displays pressure evolution for three values of the domain extent for the one-dimensional (upper) and the cylindrical (lower) domains in both dimensional (left) and dimensionless (right) variables. This allows us to get a double point of view, because the dimensional scale exhibits the behavior as it would be observed, while the dimensionless scale reveals the actual dependence on the domain extent, which is however unknown in real situations.

In the case of one-dimensional domain, the deviation is independent on the domain extent at early times, whereas it increases significantly with L for greater times (Fig. 2.7a). When results are scaled with the respective characteristic pressure and time (Fig. 2.7b), the curves collapse and the peak occurs at dimensionless time t_D=0.2, which shows that the deviation is proportional to the domain dimension.

The behavior is pretty different in the cylindrical domain (Fig. 2.7 - lower panels). The case of plane strain and constrained outer boundary is considered here, but we have observed that the behavior of the other cases is similar, but scaled according with values of parameter θ (Table 2.1). At early time, the deviation is greater for smaller domain extension R, but the peak values are pretty insensitive to domain extent, with an almost imperceptible increase for larger R (Fig. 2.7c). On the other hand, when results are normalized with the respective characteristic pressure and time (Fig. 2.7d), the peaks are greater for smaller domain, which is coherent with the tendency of the spatial average $\overline{p}$.

The reason of discrepancy between one-dimensional and cylindrical domain resides in the geometry, because, as stated above, the outer boundary affect results and the volume of aquifer affected increases with the radius of the cone of overpressure in the cylindrical case, but not in the one-dimensional case. Therefore the influence of the outer boundary is slight in the cylindrical domain and great

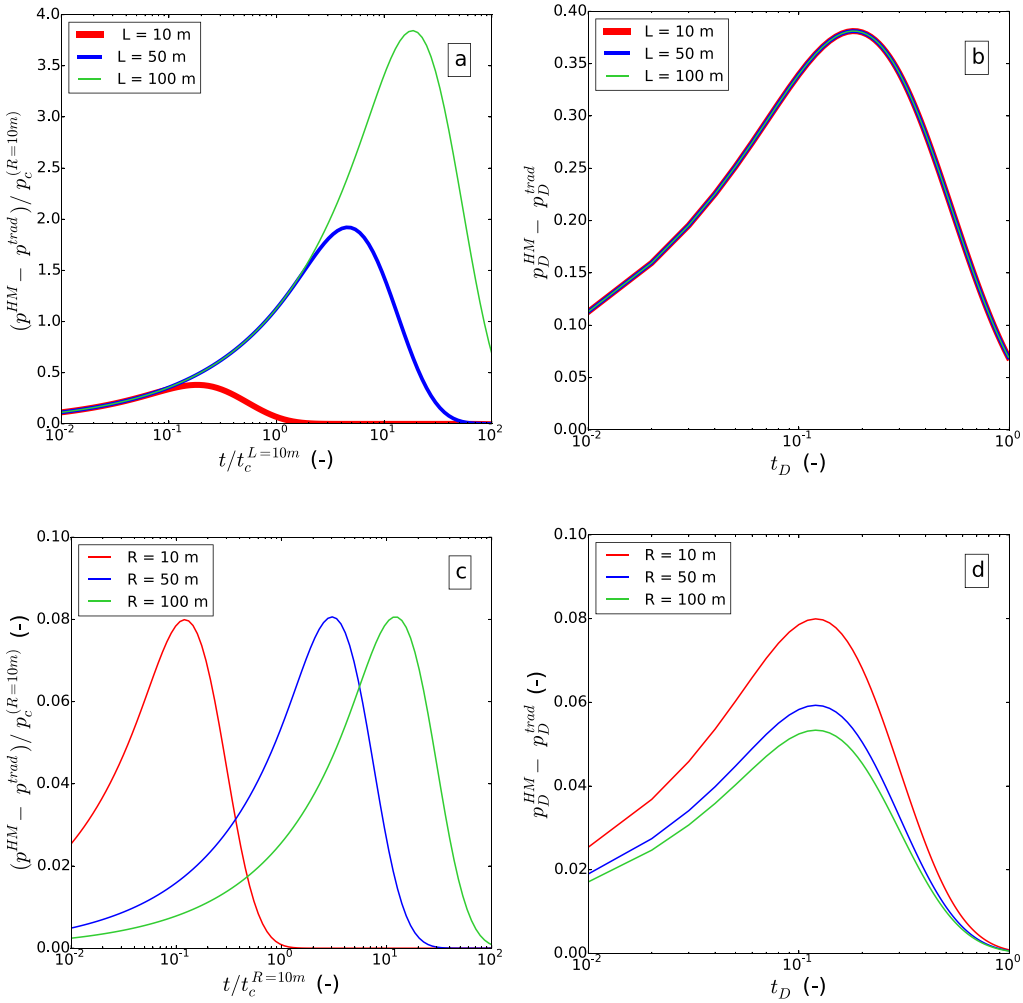

Figure 2.7: Sensitivity analysis respect to domain extent for one-dimensional domain (upper) and cylindrical domain with plane strain and constrained outer boundary (lower). Temporal evolution of the difference between HM and traditional solutions for three values of domain extension in both dimensional (a and c - pressure and time are scaled by a constant value) and dimensionless variable (b and d). Results are relative to a point placed at 1 m distance from the well (a and c) and at dimensionless distance equal to 0.1 (b and d).

for one-dimensional domain. The implications are interesting, since the domain extension is in general unknown. In the cylindrical domain, which is the most realistic, the maximum deviation is almost independent of the domain extension.

In the foregoing we have simplified the solution to the problems with constant pressure at the outer boundary, disregarding the compressibility of solid grains and water with respect to that of the porous medium. This simplification is valid

for unconsolidated aquifers, but not for rocks, especially at large depths. If the compressibility of grains and water (β_T) is acknowledged, the solution is barely sensitive to the compressibility of the porous matrix, which slightly modifies the parameter θ (Eqs. (2.14c) and (2.31c)), i.e., θ is smaller for stiffer rocks. Note that, when β_T is ignored, θ depends solely on Poisson's ratio, but not on the actual stiffness of the medium (Tab. 2.1).

Moreover, response is quite sensitive to compressibility of solid grains K_s, which is strictly related to the Biot-Willis coefficient a. It is often assumed that solid grains are incompressible, which corresponds to $a = 1$. However, a can be smaller than 1, especially in rocks (Nur and Byerlee, 1971; Mitchell et al., 2005). Smaller values of a corresponds to smaller θ (recall Eqs. (2.31c) and (2.4)), which reduces the difference between HM and traditional formulation in both cases of prescribed pressure (Fig. 2.8) and prescribed flux (Eq. (2.43)) on the outer boundary.

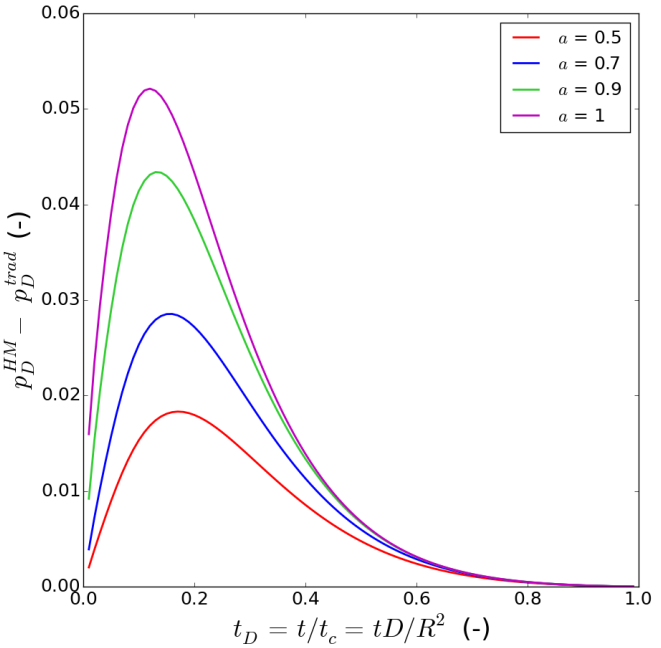

Figure 2.8: Sensitivity analysis respect to the Biot-Willis coefficient a for the case of cylindrical domain with plane strain and constrained outer boundary. Difference between HM and traditional solutions vs dimensionless time for a point placed at 1 m distance from the well. Pressure is normalized respect to the steady state pressure at $r = r_0$.

2.6 Discussion and Conclusions

Storage expresses the volumetric deformation capacity of the aquifer. The main point of our work is that deformation capacity depends not only on the compressibility of the medium, but also on the geometry of the aquifer and on the surrounding constraints to deformation, because hydraulic gradients act as body forces that press the medium in the direction of flow. We apply poroelasticity equations to highlight the non-local nature of the storage, i.e., it depends on the pressure distribution over the whole aquifer.

We present analytic solutions to the hydro-mechanical problem of fluid injection (or extraction) into finite aquifers, i.e., aquifers that are laterally confined by surrounding formations. We analyze the HM pressure response and its deviation respect to the traditional hydraulic solutions. If the lateral confinement allows deformations, the deviation is minor so that it can be disregarded and the classical storage coefficient can be adopted with a small error. On the other hand, if the aquifer deformation is constrained by the surrounding formations, pressure variations may be greater than expected (i.e., calculated according to the traditional methods). We have adopted the hypotheses of a complete restraint on the outer boundary, which may be not realistic. However, even a partial restraint of deformations may have significant effects on the pressure response. This correction should, therefore, be taken into account in situation of massive injection, such as Enhanced Geothermal Systems or CO_2 geological storage, because maximum sustainable pressure limit can be exceeded.

HM coupling implies that the pressure response propagates faster than predicted by the traditional solution, which upsets the concept of characteristic time. This complicates the estimation of the area affected by overpressure at certain time of injection.

It is worth noting that the described behavior applies on both injection and pumping. As also observed by Pujades et al. (2017), field measurements of pumping tests and laboratory tests may provide different estimations of the storage coefficient and therefore of the mechanical parameters. Application of the proposed formulation in conjunction with the traditional methods may help to avoid an incorrect estimation of the hydraulic and mechanical parameters.

3

A Practical Solution to the Mechanical Perturbations Induced by Non-Isothermal Injection into a Permeable Medium *

3.1 Introduction

Fluid injection into geological formation is required for numerous purposes and engineering operations related to energy production. When fluid is injected into a reservoir, pore liquid pressure increases, which modifies the stress field (Rutqvist and Stephansson, 2003). Furthermore, if the reservoir is deep, it will usually be hotter than the injected fluid. In fact, the temperature contrast may be great (e.g., Enhanced Geothermal Systems), which may generate large thermal deformations that will in turn affect the stress field (Ghassemi, 2012). In fractured reservoirs, hydraulic and thermal stress changes provoke opening and sliding of the fractures. When the perturbation is significant, it can induce seismic events or open secondary fractures. This coupled thermo-hydro-mechanical behavior has become a matter of special interest because of public concern about microseismicity. Thus, it is crucial to understand how pressure and temperature variations modify the stress field in order to predict the reservoir response. It is important to identify the respective effects of pressure and temperature variations as well as their combined effects.

Coupling between hydraulic and mechanical processes in permeable media was originally formulated by Terzaghi (1923) for the unidirectional case and then extended to the three dimensions by the Biot poroelasticity theory (Biot, 1941), subsequently refined by this author (Biot, 1956a), Verruijt (1969), and

*This chapter is based on the paper by De Simone et al. (2017a).

Nomenclature

C_s,C_w	thermal heat capacity of solid and water	(J/m^3 K)
C	thermal heat capacity of the reservoir, $C = C_s(1-\phi) + C_w\phi$	(J/m^3 K)
D_H	hydraulic diffusivity, $D_H = k/S_s$	(m^2/s)
D_T	thermal diffusivity, $D_T = \zeta/C$	(m^2/s)
E	Young's modulus	(Pa)
F	generic perturbation p or T	
G	shear modulus, $G = E/(2(1+\nu))$	(Pa)
k	intrinsic permeability	(m^2)
K	Bulk modulus, $K = E/(3(1-2\nu))$	(Pa)
L	unidirectional domain length	(m)
p	fluid pressure	(Pa)
q	specific flux	(m^3/s m^2)
q_0	specific injection rate	(m^3/s m^2)
r	space coordinate along the radial flow direction	(m)
r_0	well radius	(m)
R	radial domain length	(m)
S_s	specific storage coefficient, $S_s = (\phi\beta + 1/K)$	(1/Pa)
t	time	(s)
T	Temperature	($^\circ$ C)
$\mathbf{u}$	displacement vector	(m)
V	constant parameter for radial velocity, $V = (q_0 C_W r_0 - \zeta)/C$	(m^2/s)
x, y, z	space coordinates	(m)
α_T	linear thermal expansion coefficient	(1/$^\circ$C)
β	water compressibility	(1/Pa)
$\boldsymbol{\varepsilon}$	strain tensor	(-)
θ	space coordinate along the hoop (or angular) direction	($^\circ$)
ζ	thermal conductivity	(W/m K)
λ	Lamé constant, $\lambda = E\nu/((1+\nu)(1-2\nu))$	(Pa)
μ	fluid viscosity	(Pa s)
ν	Poisson ratio	(-)
ξ	advective distance in unidirectional case, $\xi = C_w q_o t/C$	(m)
ϱ	advective distance in radial coordinates, $\varrho = \sqrt{r_0^2 + 2Vt}$	(m)
$\boldsymbol{\sigma}$, $\boldsymbol{\sigma'}$	total and effective stress tensor	(Pa)
ϕ	porosity	(-)

by Rice and Cleary (1976). Thermo elastic effects were then introduced into the thermo-poroelasticity formulation (Biot, 1956b; Palciauskas and Domenico, 1982). Analogies and comparisons between thermal and hydraulic effects have been studied for many years and they continue to be a subject of interest (Biot, 1956b; Geertsma, 1957; Perkins and Gonzalez, 1984, 1985; McTigue, 1986; Norris, 1992; Segall and Fitzgerald, 1998; Rudnicki, 1999; Zimmerman, 2000; Dempsey et al., 2014). Poroelastic and thermoelastic effects depend on mechanical properties in different ways and display different response times (Ghassemi et al., 2007). In general, the area affected by fluid overpressure will be much greater than the cooled zone at any given time. Furthermore, the combined effect of pressure and thermal perturbations is non-trivial. In fact, heat transport depends on fluid flow, which, in turn, is affected by reservoir deformations driven by temperature

and pressure variations. Moreover, temperature affects density and viscosity, and thus fluid flow.

Coupled thermo-hydro-mechanical effects of cold water injection into a hot reservoir is usually studied by means of numerical simulations (Kohl et al., 1995; Kolditz and Clauser, 1998; Bruel, 2002; McDermott et al., 2006; Ghassemi et al., 2007, 2008; Ghassemi and Zhou, 2011; De Simone et al., 2013). The increased calculation capacity allows modelers to simulate several coupled processes simultaneously applied to sophisticated geometry. Nevertheless, the very complexity of the problem makes it difficult to interpret model results, which is a prerequisite for useful recommendations. In addition, errors in model input or in the code itself may be hard to detect. In this context, analytical solutions are a useful tool for improving our understanding of interactions, identifying the controlling parameters, testing codes and for providing a rapid assessment of the system response to an alteration.

Analytical expressions for poroelastic deformations due to dewatering or injection have been formulated by Verruijt (1969), Gambolati (1974), Bear and Corapcioglu (1981a), among others. Furthermore, analytical solutions to the thermoelasticity problem in a hollow cylinder have been proposed by several authors (see review by Shahani and Nabavi, 2007). Some of them considered a general temperature distribution (Timoshenko and Goodier, 1951; Wang, 1995; Cho et al., 1998). Most of these solutions use the Laplace or Hankel transform, defining the transient temperature solution by means of Bessel functions, which leads to large and complex expressions for displacements and stresses. Such solutions are not easy to use and do not account for the influence of the conditions and the parameters. Moreover, these solutions are generally restricted to the case of pure heat conduction (Shahani and Nabavi, 2007, and references therein) or pure advection (Hojka et al., 1993; Kocabas, 2004). To our knowledge, only Wang and Dusseault (2003) have considered the two processes. They calculated thermal stress with a transient temperature distribution defined by means of Bessel functions. In fact, thermal transfer can be governed by either advection or conduction, depending on in-situ properties. Since the thermal properties of geological materials have a restricted range of variation, the process depends on hydraulic conductivity of the medium which has a wider range of variability. As reported by Hojka et al. (1993) and Wang and Dusseault (2003), conduction dominates heat transfer in formation with permeability smaller than 10^{-18} m^2, whereas advection dominates

heat transfer in formation with permeability greater than 10^{-15} m^2.

In this paper a practical solution to the transient advection-conduction heat transfer problem in radial coordinates is proposed. The solution yields a good approximation in the case of advection-dominated problems. The derived solution appears very similar to that of the unidirectional problem, which is easy to apply to mechanical equilibrium equations. This facilitates the development of usable analytical solutions for the thermoelastic response to non-isothermal injection into a radial reservoir. This solution is then compared with the analytical solution for the poroelastic problem in order to better understand the respective roles of overpressure and temperature in the overall behavior and to define the parameters that govern the processes. The validity of the approximation is verified by comparison of the analytical solution to numerical simulation results.

3.2 Derivation of the analytical solutions

3.2.1 Problem Statement

We assume a horizontal, homogeneous and isotropic reservoir that is initially at rest, with constant pressure, temperature and stress. A cold fluid is injected at a constant rate and temperature through a vertical borehole that runs through the whole reservoir. The reservoir is assumed to be of an infinite thickness (i. e., infinite in the axial dimension). As a result, the problem is axisymmetric around the well and fluid flux is defined by a single horizontal radial component. Since the pressure and temperature field are axisymmetric, plane strain conditions in the vertical direction are assumed, i.e., displacements are only radial, but vertical and angular (hoop) stresses will be generated.

A unidirectional problem is also considered for the sake of completeness. The model is identical to the radial one but without the axisymmetry condition around the well. Unidirectional and radial solutions may be compared to provide insight into similarities and differences.

All fluid and reservoir properties (fluid density and viscosity, reservoir hydraulic conductivity, thermal conductivity and porosity) are assumed to be constant and isotropic in order to simplify the derivation of analytical solutions. It should be noted that, in general, pressure and temperature variations generate

strains that affect porosity, hydraulic conductivity and fluid density, which in turn affect pressure and temperature variations. Moreover, temperature affects fluid density and viscosity, hence the pressure field. All these relations are formalized in a fully coupled formulation and are best taken into account in a numerical simulation and will be ignored here.

The effect of the mechanical boundary conditions (BCs) on the porothermoelasticity coupling will be explored. BCs are known to affect the mechanical response (Rudnicki, 1999; Segall and Fitzgerald, 1998; Hillis, 2000). Geomechanical models are generally performed by adopting fixed or free displacement (i.e. prescribed stress) BCs for the outer boundary and by adopting a domain that is sufficiently big to avoid excessive boundary influence in the zone of interest. Nevertheless, the real in-situ condition is probably an intermediate condition. The presence of stiffer surroundings, for instance, may partially hinder the reservoir deformation. However, the geological environment is often unknown. Thus, we consider two extreme cases: (1) no displacements (i.e., stiff outer boundary) and (2) constant stress (i.e., soft outer boundary) in order to elucidate their respective influences on the process (Fig. 3.1). No displacement condition is assumed for the inner boundary (the injection well).

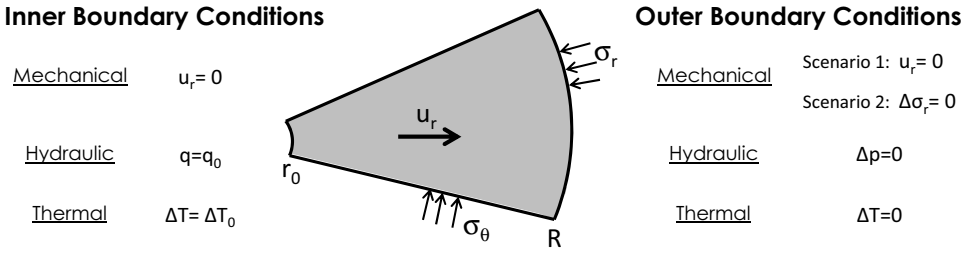

Figure 3.1: Boundary conditions considered.

We consider that fluid flow is at steady-state, whereas the heat transport is transient. The assumption is reasonable because the processes have very different response time, i.e. pressure propagates much faster than temperature.

3.2.2 Governing equations

The problem is governed by fluid mass balance, energy balance and momentum conservation, which can be written as

$$\text{Fluid flow:} \qquad \frac{k}{\mu}\,\nabla^2 p = 0 \tag{3.1}$$

$$\text{Heat transport:} \qquad \frac{\partial T}{\partial t} + q\,\frac{C_w}{C}\,\nabla T = \frac{\zeta}{C}\,\nabla^2 T \tag{3.2}$$

$$\text{Mechanical equilibrium:} \qquad \nabla\cdot\boldsymbol{\sigma} + \mathbf{b} = \mathbf{0} \tag{3.3}$$

where p is fluid pressure, k is intrinsic permeability, μ is fluid viscosity, T is temperature, q is specific flux, C_w is the fluid thermal heat capacity, C is the reservoir thermal heat capacity, ζ is thermal conductivity, $\boldsymbol{\sigma}$ is total stress tensor and $\mathbf{b}$ represents the body forces vector. ∇f is the gradient of a field ($\partial f/\partial x$ in the unidirectional case, $\partial f/\partial r$ in the radial case), $\nabla^2 f$ is the Laplacian of a scalar field ($\partial^2 f/\partial x^2$ or $(1/r)\partial(r\partial f/\partial r)/\partial r$ in the unidirectional and radial cases, respectively) and $\nabla\cdot\boldsymbol{g}$ is the divergence of a vector field ($\partial g_x/\partial x$ or $(1/r)\partial(rg_r)/\partial r$ in the unidirectional and radial cases, respectively). We adopt a linear elastic model by means of the generalized Hooke's Law for non-isothermal conditions (Biot, 1956b; Palciauskas and Domenico, 1982):

$$\boldsymbol{\sigma'} = 2G\,\boldsymbol{\varepsilon} + \lambda\,\varepsilon_{vol}\,\mathbf{I} - (2G+3\lambda)\,\alpha_T\,\Delta T\,\mathbf{I}\,, \tag{3.4}$$

where $\boldsymbol{\sigma'}$ is the effective stress tensor, G and λ are the shear and Lamé moduli, respectively, α_T is the linear thermal expansion coefficient, $\mathbf{I}$ is the identity matrix, $\boldsymbol{\varepsilon} = 1/2\left[\nabla\mathbf{u} + (\nabla\mathbf{u})^T\right]$ is the strain tensor and $\epsilon_{vol} = \nabla\cdot\mathbf{u}$ is the volumetric strain, which corresponds to $\varepsilon_x + \varepsilon_y + \varepsilon_z = \partial u_x/\partial x + \partial u_y/\partial y + \partial u_z/\partial z$ in Cartesian coordinates and to $\varepsilon_r + \varepsilon_\theta + \varepsilon_z = \partial u_r/\partial r + u_r/r + \partial u_z/\partial z$ in radial coordinates. Substituting equation (3.4) into (3.3), by means of Terzaghi's Law, i.e., $\boldsymbol{\sigma} = \boldsymbol{\sigma'} - \alpha p\mathbf{I}$ (we assume the Biot coefficient α to be equal to 1) yields

$$G\,\nabla^2\mathbf{u} + (G+\lambda)\;\nabla(\nabla\cdot\mathbf{u}) = \nabla(\Delta p) + (2G+3\lambda)\,\alpha_T\,\nabla(\Delta T)\;. \tag{3.5}$$

Note that we assume the convention that tensile stress and extensional strain are positive. Note also that this equation is driven by two forcing terms (fluid

pressure and temperature gradients). Below we take advantage of linearity to solve the problem independently for each forcing term before superimposing the solutions. For subsequent derivations, it is convenient to divide the equation by $(2G + \lambda)$, and write the right hand side as $f\nabla(\Delta F)$, where F can be p or T, and f is

$$f \equiv \begin{cases} \dfrac{1}{2G+\lambda} & \text{if } F \equiv P \\ \\ \dfrac{1+\nu}{1-\nu}\,\alpha_T & \text{if } F \equiv T \end{cases} \tag{3.6}$$

where $\nu = \lambda/(2\lambda + 2G)$ is the Poisson ratio. Equations can be greatly simplified in the unidirectional and radial cases. In the unidirectional case, assuming unidirectional strain in the x direction yields $\varepsilon_y = \varepsilon_z = \varepsilon_{xy} = \varepsilon_{yz} = \varepsilon_{xz} = 0$, so that equation (3.4) becomes

$$\begin{aligned} \sigma_x^F &= (2G+\lambda)\,\frac{\partial u_x^F}{\partial x} - (2G+\lambda)\;f\,\Delta F \\ \sigma_y^F \equiv \sigma_z^F &= \lambda\,\frac{\partial u_x^F}{\partial x} - (2G+\lambda)\;f\,\Delta F \end{aligned} \tag{3.7}$$

while equation (3.5) becomes

$$\frac{\partial^2 u_x^F}{\partial x^2} = f\,\frac{\partial(\Delta F)}{\partial x}\,. \tag{3.8}$$

In the radial case, axisymmetry and plane strains in the z direction yield $\varepsilon_z = \varepsilon_{rz} = \varepsilon_{\theta z} = 0$ and $\tau_{r\theta} = \tau_{rz} = \tau_{\theta z} = 0$. Therefore, the generalized Hooke's Law becomes

$$\begin{aligned} \sigma_r^F &= (2G+\lambda)\,\frac{\partial u_r^F}{\partial r} + \lambda\,\frac{u_r^F}{r} - (2G+\lambda)\;f\,\Delta F \\ \sigma_\theta^F &= (2G+\lambda)\,\frac{u_r^F}{r} + \lambda\,\frac{\partial u_r^F}{\partial r} - (2G+\lambda)\;f\,\Delta F \\ \sigma_z^F &= \lambda\,\left(\frac{\partial u_r^F}{\partial r} + \frac{u_r^F}{r}\right) - (2G+\lambda)\;f\,\Delta F \end{aligned} \tag{3.9}$$

and equation (3.5) in terms of perturbation of the generic F yields

$$\frac{\partial^2 u_r^F}{\partial r^2} + \frac{1}{r}\frac{\partial u_r^F}{\partial r} - \frac{1}{r^2}u_r^F = f\,\frac{\partial(\Delta F)}{\partial r}\,. \tag{3.10}$$

Note that time does not appear explicitly in any of these equations as inertial terms were ignored in the equilibrium equation (3.3). Yet stresses, strains and displacements evolve in time in response to changes in p and T. Specifically $\boldsymbol{\sigma}$ refers to stress variation if an initial stress $\neq 0$ is assumed.

3.2.3 Analytical solutions

The solution procedure is the same for both cases. We first derive the pressure and temperature field solutions. We then obtain the displacement solution using the equilibrium equation (eq. (3.5) for the general case; eq. (3.8) for the unidirectional case and eq. (3.10) for the radial case) with a generic forcing term F. We then use the generalized Hooke's Law to compute stresses. Because of the linear elasticity, the stress variations and the displacements calculated for temperature and pressure variation can be superimposed on each other and on the initial conditions.

Unidirectional

We assume the boundary conditions of Fig. 3.1, with a constant injection rate q_0 at $x = 0$, and a constant pressure ($\Delta p = 0$) at $x = L$. In this case the solution for unidirectional fluid flow at steady state is

$$\Delta p(x) = \frac{q_0 \mu}{k}\,(L - x)\,, \tag{3.11}$$

where $\Delta p(x)$ is the pressure variation respect to the undisturbed condition, q_0 is the injection rate Q per unit surface. We now consider the heat equation (eq. (3.2)) for unidirectional flow in the x direction, constant initial condition and a Dirichlet boundary condition at $x = 0$ (prescribed temperature variation ΔT_0) with (quasi) steady state fluid flow. The left side of equation (3.2) represents the material derivative DT/Dt. It is therefore convenient to formulate the problem by adopting a Lagrangian formulation with a coordinate system that moves at

the velocity of temperature. The velocity is $d\xi/dt = C_w\, q_0/C$, even if q_0 is not constant. Thus, the solution of the advection problem is

$$\xi = \frac{C_w}{C}\, q_0\, t\,. \tag{3.12}$$

The solution to the advection-diffusion problem was formulated by Ogata (1970) on the basis of the solution for heat conduction of Carslaw and Jaeger (1959), which is also valid with dispersion:

$$\Delta T(x,t) = \frac{\Delta T_0}{2}\left[\operatorname{erfc}\left(\frac{x-\xi}{\sqrt{4D_T t}}\right) + \exp\left(\frac{\xi/t}{D_T}x\right)\,\operatorname{erfc}\left(\frac{x-\xi}{\sqrt{4D_T t}}\right)\right] \tag{3.13}$$

where $D_T = \zeta/C$ is the thermal diffusivity. The solution is valid for a semi-infinite medium, that is as long as the temperature front is far from the outer border at $x = L$.

The equation could also be used for the Cauchy BC, for large values of time, without much loss of accuracy (Sauty, 1980). If advection dominates (e.g. Peclet number greater than 10) , the second term in equation (3.13) may be neglected (Ogata, 1970), leading to the approximate symmetric solution

$$\Delta T(x,t) = \frac{\Delta T_0}{2}\,\operatorname{erfc}\left(\frac{x-\xi}{\sqrt{4D_T t}}\right)\,. \tag{3.14}$$

For the sake of simplicity, we use this latter solution for the thermoelasticity problem. The solution to the elasticity problem is obtained by integrating twice equation (3.8), which yields

$$\begin{aligned} u_x^F(x,t) &= f\left[\int_0^x \Delta F\,(x,t)\,dx + A\,x + B\right] \\ \sigma_x^F(x,t) &= (2G+\lambda)\,f\,A \\ \sigma_y^F(x,t) \equiv \sigma_z^F &= -2G\,f\,\Delta F(x,t) + \lambda\,f\,A\,. \end{aligned} \tag{3.15}$$

Constants A and B are found by applying the mechanical boundary conditions of the two scenarios considered (unidirectional version of Fig. 3.1). The zero

displacement condition at the origin yields $B = 0$. The zero displacement at $x = L$ (Scenario 1) implies $A = -\int_0^L \Delta F\,(x,t)\,dx/L$, whereas the zero stress at $x = L$ (Scenario 2) yields $A = 0$. Substitution of pressure and temperature expressions and their integrals (view Appendix E) will provide the final solution (Table 3.1).

Table 3.1: Solutions to the unidirectional problem at steady state flow.

		Hydraulic forcing	**Thermal forcing (valid for large Pe)**
Scenario 1 $u_x(L,t) = 0$	u_x	$\frac{1}{2G+\lambda}\frac{q_0\mu}{k}\left(\frac{Lx}{2} - \frac{x^2}{2}\right)$	$\frac{1+\nu}{1-\nu}\alpha_T\frac{\Delta T_0}{2}\left[I_x - \frac{x}{L}I_L - \left(1-\frac{x}{L}\right)I_0\right]$
	σ_x	$-\frac{q_0\mu}{k}\frac{L}{2}$	$-(2G+3\lambda)\alpha_T\frac{\Delta T_0}{2}\frac{1}{L}(I_L - I_0)$
	$\sigma_y \equiv \sigma_z$	$\frac{q_0\mu}{k}\left(\frac{1-2\nu}{1-\nu}x - \frac{2-3\nu}{2(1-\nu)}L\right)$	$-\frac{1+\nu}{1-\nu}\alpha_T\frac{\Delta T_0}{2}\left[\frac{\lambda}{L}(I_L - I_0) + 2G\,\mathrm{erfc}\left(\frac{x-\xi}{\sqrt{4D_T t}}\right)\right]$
Scenario 2 $\Delta\sigma_x(L,t) = 0$	u_x	$\frac{1}{2G+\lambda}\frac{q_0\mu}{k}\left(Lx - \frac{x^2}{2}\right)$	$\frac{1+\nu}{1-\nu}\alpha_T\frac{\Delta T_0}{2}\left[I_x - I_0\right]$
	σ_x	0	0
	$\sigma_y \equiv \sigma_z$	$-\frac{1-2\nu}{1-\nu}\frac{q_0\mu}{k}(L-x)$	$-\frac{E}{1-\nu}\alpha_T\frac{\Delta T_0}{2}\,\mathrm{erfc}\left(\frac{x-\xi}{\sqrt{4D_T t}}\right)$

$$I_x = (x-\xi)\,\mathrm{erfc}\left(\frac{x-\xi}{\sqrt{4D_T t}}\right) - \frac{\sqrt{4D_T t}}{\sqrt{\pi}}\exp\left[-\left(\frac{x-\xi}{\sqrt{4D_T t}}\right)^2\right]$$

$$I_L = (L-\xi)\,\mathrm{erfc}\left(\frac{L-\xi}{\sqrt{4D_T t}}\right) - \frac{\sqrt{4D_T t}}{\sqrt{\pi}}\exp\left[-\left(\frac{L-\xi}{\sqrt{4D_T t}}\right)^2\right]$$

$$I_0 = -\xi\,\mathrm{erfc}\left(\frac{-\xi}{\sqrt{4D_T t}}\right) - \frac{\sqrt{4D_T t}}{\sqrt{\pi}}\exp\left[-\left(\frac{-\xi}{\sqrt{4D_T t}}\right)^2\right]$$

Radial

Given the boundary conditions of Fig. 3.1, with a constant injection rate q_0 at r=r_0, and constant pressure ($\Delta p = 0$) at $r = R$, the solution for radial fuid flow (eq. (3.1)) in steady state conditions is given by the Dupuit-Thiem formula (Thiem, 1906)

$$\Delta p(r) = \frac{q_0 r_0 \mu}{k}\, ln\left(\frac{R}{r}\right) \tag{3.16}$$

where q_0 is the injection flow rate Q divided by the injection surface $2\pi r_0 b$ (b is the aquifer thickness).

The solution to the transient transport equation in radial coordinates is not easy. It has been proposed by several authors and for different fields of application. Exact or approximate solutions to the radial dispersion-adevction problem have been put forward by Ogata (1970); Hoopes and Harleman (1967); Tang and Babu (1979); Hsieh (1986), De Josselin de Jong (in Lau, 1959), Raimondi et al. (1959), among others (see Veling (2012) for a complete review of literature and for a generalized solution). These solutions are related to solute transport in aquifers and often do not take into account the diffusion process. As regards the temperature field, the exact solutions to the pure conduction problem (Carslaw and Jaeger, 1959) and to the conduction-advection problem (Wang and Dusseault, 2003) have been formulated, but they involve the use of mathematics that is not straightforward. We now develop an approximate and easy-to-use solution to the advection-conduction case with prevalent advection. The flow rate q is only a function of space for both steady state and transient conditions (i.e., if $r \leq \sqrt{2.25kt/\mu S_s}$). It yields

$$q(r) = \frac{Q}{2\pi r} = \frac{q_0 r_0}{r} \,. \tag{3.17}$$

If dispersion is ignored and if constant thermal conductivity ζ is considered, the heat transfer equation is

$$\frac{\partial T}{\partial t} = \frac{\zeta}{C}\,\frac{\partial^2 T}{\partial r^2} + \frac{\zeta}{C}\,\frac{1}{r}\,\frac{\partial T}{\partial r} - q_0\,\frac{C_w}{C}\,\frac{r_0}{r}\,\frac{\partial T}{\partial r} \,. \tag{3.18}$$

As in the foregoing section, we apply the method of characteristics and write the equation in terms of the material derivative obtaining the following expression in which the first order part of the conduction term is joined with the advection term in the constant parameter $V = (q_0 C_w r_0 - \zeta)/C$.

$$\frac{DT}{Dt} \equiv \frac{\partial T}{\partial t} + \frac{V}{r}\frac{\partial T}{\partial r} = \frac{\zeta}{C}\,\frac{\partial^2 T}{\partial r^2} \,. \tag{3.19}$$

Note that velocity is $d\varrho/dt = V/r$, which yields the solution to the advection problem

$$\varrho = \sqrt{r_0^2 + 2Vt} \,. \tag{3.20}$$

A similar procedure was proposed by Hojka et al. (1993), who considered only advection. Bearing this in mind, equation (3.18) takes the form of equation (3.2) for the unidirectional case if the velocity term (V/r) is substituted by an average constant velocity $= \varrho/t$. Thus, in the case of constant temperature initial conditions and the Dirichlet boundary condition at $r = r_0$ (prescribed temperature variation ΔT_0), the solution is similar to that of Ogata and Banks. This yields

$$\Delta T(r,t) = \frac{\Delta T_0}{2}\left[\operatorname{erfc}\left(\frac{r-\varrho}{\sqrt{4D_T t}}\right) + \exp\left(\frac{\varrho/t}{D_T}\, r\right)\, \operatorname{erfc}\left(\frac{r-\varrho}{\sqrt{4D_T t}}\right)\right] . \quad (3.21)$$

The solution is valid for a semi-infinite medium, that is the time during which the temperature front is far from the outer border at $r = R$. Note also that this solution is valid as long as q is constant in time, which is valid for steady-state fluid flow, but would also be very approximate for transient radial flow. As in the previous section, we remove the second term of equation (3.21), obtaining the approximate solution

$$\Delta T(r,t) = \frac{\Delta T_0}{2}\, \operatorname{erfc}\left(\frac{r-\varrho}{\sqrt{4D_T t}}\right) \quad (3.22)$$

which is then used for the solution to the thermoelasticity problem. Integration of equation (3.10) can be found in Timoshenko and Goodier (1951) and leads after some algebra to the solution

$$\begin{aligned}
u_r^F(r,t) &= f\left[\frac{1}{r}\int_{r_0}^{r} r\,\Delta F(r,t)\,dr + C\,r + \frac{D}{r}\right] \\
\sigma_r^F(r,t) &= f\left[-2G\,\frac{1}{r^2}\int_{r_0}^{r} r\,\Delta F(r,t)\,dr + (2G+2\lambda)\,C - 2G\,\frac{D}{r^2}\right] \\
\sigma_\theta^F(r,t) &= f\left[2G\,\frac{1}{r^2}\int_{r_0}^{r} r\,\Delta F(r,t)\,dr - 2G\Delta F(r,t) + (2G+2\lambda)\,C + 2G\frac{D}{r^2}\right] \\
\sigma_z^F(r,t) &= f\left[-2G\,\Delta F(r,t) + 2\lambda\,C\right]
\end{aligned} \quad (3.23)$$

Constants C and D are found assuming the mechanical boundary conditions of the two scenarios considered (Fig. 3.1). Substitution of pressure and temperature expressions and their integrals (view Appendix E) will provide the final solution (Table 3.2).

Table 3.2: Solutions to the radial problem

		Hydraulic forcing (valid for steady state flow)	**Thermal forcing** (valid for transient or steady state flow and large Pe)
Scenario 1 $u_r(R,t)=0$	u_r	$\frac{1}{2G+\lambda}\frac{\omega}{2r}\left[Y_r-\frac{r^2-r_0^2}{R^2-r_0^2}Y_R-\frac{R^2-r^2}{R^2-r_0^2}Y_0\right]$	$\frac{1+\nu}{1-\nu}\frac{\psi}{2r}\left[I_r-\frac{r^2-r_0^2}{R^2-r_0^2}I_R-\frac{R^2-r^2}{R^2-r_0^2}I_0\right]$
	σ_r	$-\frac{1-2\nu}{1-\nu}\frac{\omega}{2r^2}\left[Y_r-Y_0+\left(\frac{r^2}{1-2\nu}+r_0^2\right)\frac{Y_R-Y_0}{R^2-r_0^2}\right]$	$-\frac{E}{1-\nu}\frac{\psi}{2r^2}\left[I_r-I_0+\left(\frac{r^2}{1-2\nu}+r_0^2\right)\frac{I_R-I_0}{R^2-r_0^2}\right]$
	σ_θ	$\frac{1-2\nu}{1-\nu}\frac{\omega}{2r^2}\left[Y_r-Y_0-2r^2\ln\left(\frac{R}{r}\right)-\left(\frac{r^2}{1-2\nu}-r_0^2\right)\frac{Y_R-Y_0}{R^2-r_0^2}\right]$	$\frac{E}{1-\nu}\frac{\psi}{2r^2}\left[I_r-I_0-2r^2\operatorname{erfc}\left(\frac{r-\varrho}{\sqrt{4D_Tt}}\right)-\left(\frac{r^2}{1-2\nu}-r_0^2\right)\frac{I_R-I_0}{R^2-r_0^2}\right]$
	σ_z	$-\frac{1-2\nu}{1-\nu}\omega\left[\ln\left(\frac{R}{r}\right)+\frac{\nu}{1-2\nu}\frac{Y_R-Y_0}{R^2-r_0^2}\right]$	$-\frac{E}{1-\nu}\psi\left[\operatorname{erfc}\left(\frac{r-\varrho}{\sqrt{4D_Tt}}\right)+\frac{\nu}{1-2\nu}\frac{I_R-I_0}{R^2-r_0^2}\right]$
Scenario 2 $\Delta\sigma_r(L,t)=0$	u_r	$\frac{1}{2G+\lambda}\frac{\omega}{2r}\left[Y_r-Y_0+\frac{G(r^2-r_0^2)}{(G+\lambda)R^2+Gr_0^2}(Y_R-Y_0)\right]$	$\frac{1+\nu}{1-\nu}\frac{\psi}{2r}\left[I_r-I_0+\frac{G(r^2-r_0^2)}{(G+\lambda)R^2+Gr_0^2}(I_R-I_0)\right]$
	σ_r	$-\frac{1-2\nu}{1-\nu}\frac{\omega}{2r^2}\left[Y_r-Y_0-\frac{(G+\lambda)r^2+Gr_0^2}{(G+\lambda)R^2+Gr_0^2}(Y_R-Y_0)\right]$	$-\frac{E}{1-\nu}\frac{\psi}{2r^2}\left[I_r-I_0-\frac{(G+\lambda)r^2+Gr_0^2}{(G+\lambda)R^2+Gr_0^2}(I_R-I_0)\right]$
	σ_θ	$\frac{1-2\nu}{1-\nu}\frac{\omega}{2r^2}\left[Y_r-Y_0-2r^2\ln\left(\frac{R}{r}\right)+\frac{(G+\lambda)r^2-Gr_0^2}{(G+\lambda)R^2+Gr_0^2}(Y_R-Y_0)\right]$	$\frac{E}{1-\nu}\frac{\psi}{2r^2}\left[I_r-I_0-2r^2\operatorname{erfc}\left(\frac{r-\varrho}{\sqrt{4D_Tt}}\right)+\frac{(G+\lambda)r^2-Gr_0^2}{(G+\lambda)R^2+Gr_0^2}(I_R-I_0)\right]$
	σ_z	$-\frac{1-2\nu}{1-\nu}\omega\left[\ln\left(\frac{R}{r}\right)-\frac{\lambda}{(G+\lambda)R^2+Gr_0^2}\frac{Y_R-Y_0}{2}\right]$	$-\frac{E}{1-\nu}\psi\left[\operatorname{erfc}\left(\frac{r-\varrho}{\sqrt{4D_Tt}}\right)-\frac{\lambda}{(G+\lambda)R^2+Gr_0^2}\frac{I_R-I_0}{2}\right]$

$$\omega=\frac{q_0r_0\mu}{k}\qquad \psi=\alpha_T\frac{\Delta T_0}{2}$$

$$Y_r=r^2\ln\left(\frac{R}{r}\right)+\frac{r^2}{2}$$

$$I_r=(r^2-\varrho^2)\operatorname{erfc}\left(\frac{r-\varrho}{\sqrt{4D_Tt}}\right)+\frac{\sqrt{4D_Tt}^2}{2}\operatorname{erf}\left(\frac{r-\varrho}{\sqrt{4D_Tt}}\right)-\frac{\sqrt{4D_Tt}}{\sqrt{\pi}}(r+\varrho)\exp\left(-\left(\frac{r-\varrho}{\sqrt{4D_Tt}}\right)^2\right)$$

$$Y_R=\frac{R^2}{2}$$

$$I_R=\left(R^2-\varrho^2\right)\operatorname{erfc}\left(\frac{R-\varrho}{\sqrt{4D_Tt}}\right)+\frac{\sqrt{4D_Tt}^2}{2}\operatorname{erf}\left(\frac{R-\varrho}{\sqrt{4D_Tt}}\right)-\frac{\sqrt{4D_Tt}}{\sqrt{\pi}}(R+\varrho)\exp\left(-\left(\frac{R-\varrho}{\sqrt{4D_Tt}}\right)^2\right)$$

$$Y_0=r_0^2\ln\left(\frac{R}{r_0}\right)+\frac{r_0^2}{2}$$

$$I_0=\left(r_0^2-\varrho^2\right)\operatorname{erfc}\left(\frac{r_0-\varrho}{\sqrt{4D_Tt}}\right)+\frac{\sqrt{4D_Tt}^2}{2}\operatorname{erf}\left(\frac{r_0-\varrho}{\sqrt{4D_Tt}}\right)-\frac{\sqrt{4D_Tt}}{\sqrt{\pi}}(r_0+\varrho)\exp\left(-\left(\frac{r_0-\varrho}{\sqrt{4D_Tt}}\right)^2\right)$$

3.3 Results

3.3.1 Validity of the solutions

In order to verify the solutions derived in the foregoing section and to gain further insight into their nature, we compare them to fully coupled numerical simulations performed with CODE_BRIGHT (Olivella et al., 1996) and an application of KRATOS multiphysics (Dadvand et al., 2010; CIMNE, 2012). The numerical models represent the conceptual models of section 3.2.1. Material properties are constant. Well radius r_0 is 0.1 m and the reservoir extends for 1000 m (R). The values assumed for the model parameters are shown in Table 3.3. Results are relative to the times in which the flow is at steady state whereas the heat transport is in transient condition. For comparison, the unidirectional solutions are also shown.

Table 3.3: Parameters used for the verification. Most of them change little from one problem to another. We have marked with an asterisk those that may change significantly.

Parameters	Values	Units
E*	1000	MPa
ν	0.3	-
k*	10^{-13}(unidirectional) / 10^{-14}(radial)	m^2
ζ	3	W m /°K
α_T	10^{-5}	1/°C
μ	10^{-10}	MPa s
C_s	2.16×10^6	J/m^3/°K
C_w	4.19×10^6	J/m^3/°K
ϕ	0.1	-
q_0*	10^{-3}(unidirectional) / 10^{-1}(radial)	kg/s/m^2
ΔT_0*	-70	°C

In Section 3.2.3, we considered the Ogata and Banks solution (Ogata, 1970) to solve the heat transport process in one dimension. We then neglected the second term and adopted the approximate solution. The effects of this truncation for Peclet numbers of 4.2 and 21 are shown in Figure 3.2 (a and b), where the full asymmetric solution (eq. (3.13)) and the approximate symmetric solution (eq. (3.14)) are compared to the results of the numerical simulations. We adopted a similar procedure for the radial case. The validity of this method for the radial problem and the consequences of the truncation are shown in Fig. 3.2 (c and d), where analytical solutions are compared with the results of numerical simulations for Peclet numbers of 1.4 and 14, which correspond to different values of flow

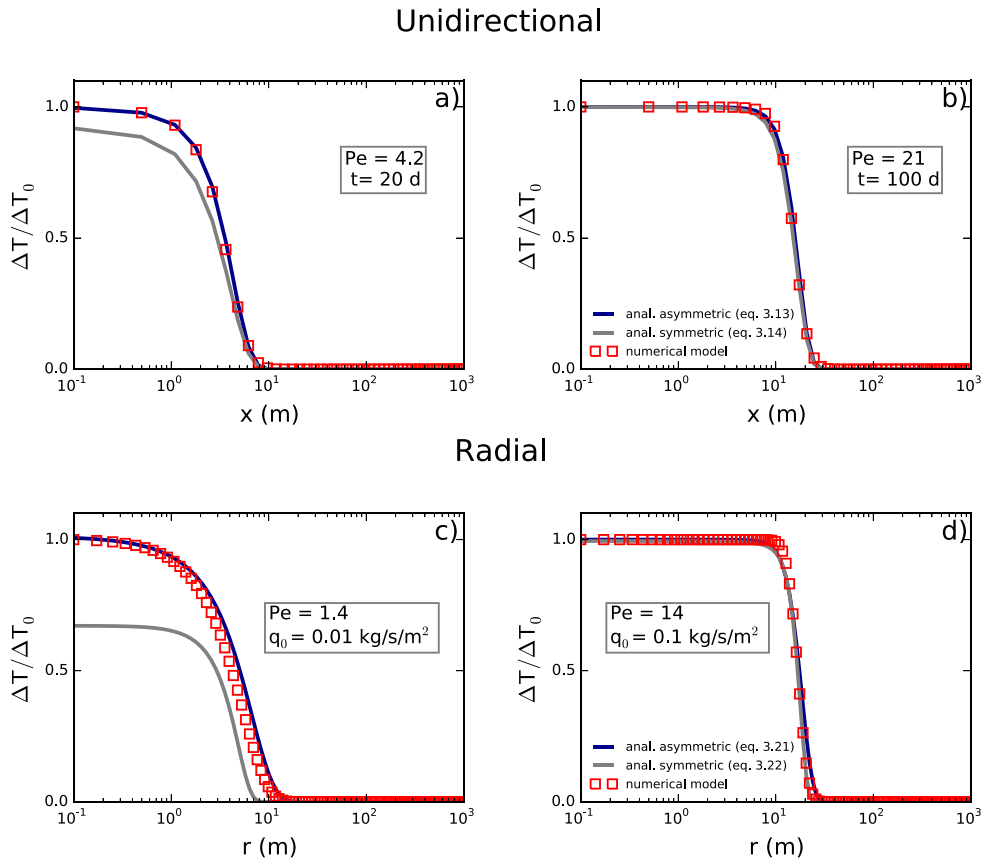

Figure 3.2: Numerical and analytical solutions of the temperature distribution in unidirectional (a and b) and radial (c and d) case for two values of Peclet number Pe and using the parameters of Table 3.3 (the solutions of the unidirectional case are relative to times 20 days and 100 days, being $Pe = qCwL_c/\zeta$ and assuming the advective distance ξ (eq. (3.12)) as characteristic length L_c; the solutions of the radial case are relative to 100 days of injection and to specific injection rate q_0 0.01 kg/s/m^2 and 0.1 kg/s/m^2, being $Pe = q_0 r_0 C_w/\zeta$ for every r).

rate injection q_0 (being $Pe = q_0 r_0 C_w/\zeta$ for every r in the radial case). The other parameters are the ones presented in Table 3.3. Results are relative to 100 days of injection. It may be observed that the complete asymmetric solution (eq. (3.21)) yields a good approximation also for small Peclet numbers. However, only advection-dominated problems (Pe$>$ 1) can be solved by this solution for ϱ to remain a real number (eq. (3.20)). The approximate symmetric solution (eq. (3.22)) gives reasonably accurate results for Peclet number > 10, which is a correct assumption in the case of massive fluid injection in geological formations.

The approximate expressions for the heat transport process are then used

for the solution to the thermoelasticity problem. Figures 3.3a and 3.3b show the comparison between our analytical solutions (Table 3.1) and the results of the numerical simulations for the unidirectional case and for the two scenarios considered (Fig. 3.1) after 300 days of injection. Needless to say, the analytical solutions match the numerical ones. In fact, the unidirectional case is presented only for the sake of completeness as its solution is trivial.

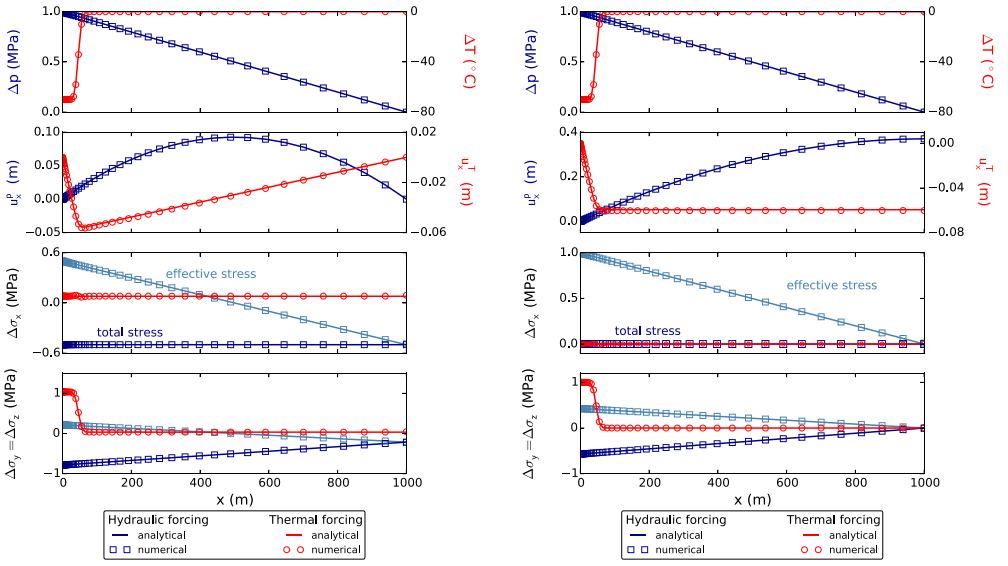

(a) Scenario 1 **(b)** Scenario 2

Figure 3.3: Analytical and numerical solutions in the unidirectional case for Scenario 1 (outer border displacements restrained) and Scenario 2 (outer border displacements allowed). Results are relative to the time = 300 days. Effective stresses are relative to the hydraulic problem (effective and total stresses produced by the thermal forcing are equivalent).

In Figures 3.4a and 3.4b we compare our analytical solutions (Table 3.2) with the numerical simulation results for the radial case and for the two scenarios considered (Fig. 3.1). Results are relative to 100 days of injection. The analytical solution relative to the hydraulic problem matches the numerical solution. The novelty of the present paper lies in the fact that the approximate solution to the radial thermal problem is consistent with the numerical results. Once the validity of the new solution was verified, we used it to illustrate some features in the Discussion.

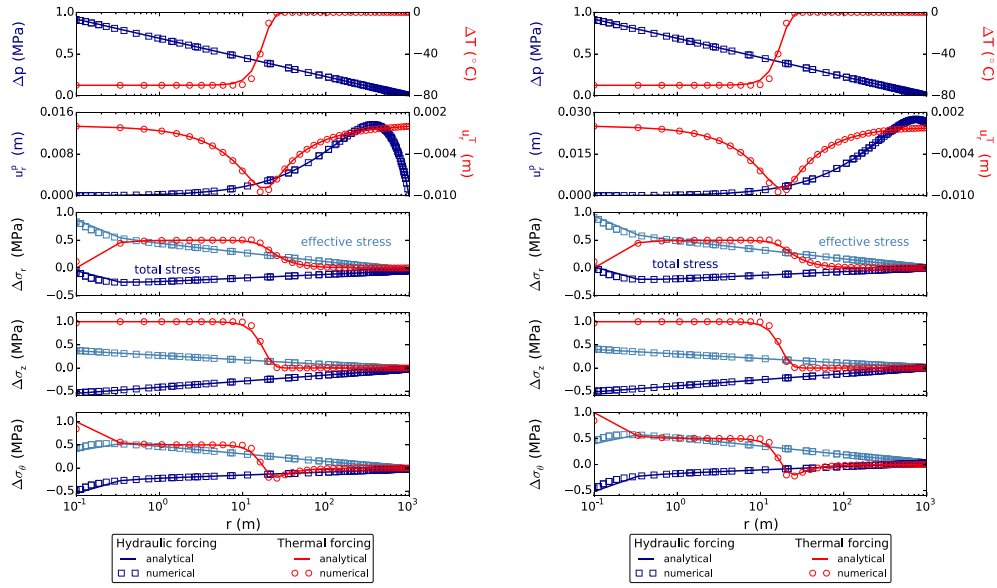

(a) Scenario 1 **(b)** Scenario 2

Figure 3.4: Analytical and numerical solutions in the radial case for Scenario 1 (outer border displacements restrained) and Scenario 2 (outer border displacements allowed). Results are relative to the time = 100 days. Effective stresses are relative to the hydraulic problem (effective and total stresses produced by the thermal forcing are equivalent).

3.3.2 Discussion

Non isothermal injection provokes deformations and stress field alterations driven by pressure and temperature field variation. The analytical expressions illustrate the formal similarity between the hydraulic and thermal impacts. When the injected fluid is cooler than the reservoir, conflicting deformations take place since pressure increase causes expansion and temperature decrease leads to contraction. In the absence of outer constraints (Scenario 2), the reservoir is free to deform. Therefore, total stress in the direction of forcing propagation remains unchanged ($\Delta\sigma_x = 0$) in the unidirectional case (Fig. 3.3b). On the contrary, σ_r does change in the radial case owing to the axisymmetry (Fig. 3.4b). In fact, the formation develops a horizontal arc effect that partially hinders radial displacements even if the outer boundary is free to deform. As a result, the three stresses depend very little on the outer BC (compare Fig. 3.4a and Fig. 3.4b), even though displacements do, as will be discussed in the following. Vertical total stress (and hoop total stress in the radial case), which is constrained, changes as a result of the Poisson effect. This means that vertical (and hoop in

the radial case) compression increases in the hydraulic problem where the reservoir expands, whereas it decreases in the thermal problem where the reservoir contracts. Effective stresses, which govern failure, it may be recalled, are equal to the total stresses plus hydraulic pressure. Thus, in the horizontal direction of the unidirectional case (Fig. 3.3b) there is an increase in the tension (reduction of compression) equivalent to the overpressure in the hydraulic problem and no variation in the thermal problem. However, the increase in tension is smaller than overpressure in the vertical direction and in all directions of the radial case (Fig. 3.4b). This means that both hydraulic and thermal effects increase the effective tensions.

The respective influences of the two processes depend on the material stiffness (thermal stresses are proportional to stiffness, eq. (3.5)), the magnitude of the imposed perturbation (i.e. ΔT_0 and q_0) and on its propagation distance (or distribution). The last factor is a function of the elapsed time of injection and of the material properties (K, k for the hydraulic problem and ζ, ϕ for the thermal one) according to the following expressions

$$\delta^P = \sqrt{\frac{k/\mu\, t}{\phi\, \beta + \frac{1}{K}}} \tag{3.24}$$

$$\delta^T = \sqrt{\frac{\zeta\, t}{C}} + \frac{q\, C_w\, t}{C} \tag{3.25}$$

where δ is the propagation distance. Figure 3.5 shows the hydraulic and thermal effects for two different times for the radial case and no lateral constraints (Scenario 2). Displacements and stresses are normalized with respect to the perturbation imposed at the boundary: the hydraulic effects are normalized with respect to the overpressure at the well (i.e. $\Delta p_0 = q_0\, r_0\, \mu/k\, ln(R/r_0)$), whereas the thermal effects are normalized with respect to $-\Delta T_0$ to avoid confusion about the sign. It is worth noting that thermal effects accumulate locally and they propagate with time (eq. (3.25)) along with the thermal front. The displacements are maxima around the cold front since they accumulate on the displacements caused by cooling up to that point in time, which might be expected. However, neither the stresses nor the displacements are reduced once the thermal front has passed. It should be pointed out that we are considering a steady state fluid flow condition with the result that no temporal variations are observable for the hydraulic problem. Nevertheless, this assumption enables us to compare the thermal and

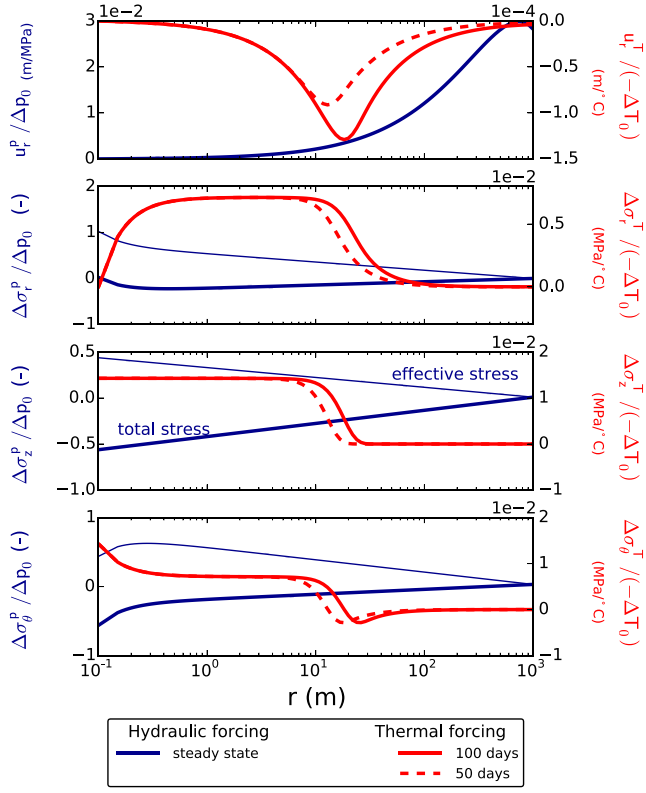

Figure 3.5: Hydraulic and thermal effects for two different times and normalized with respect to the perturbation imposed at the well, for the radial unconstrained case (Scenario 2). Effective stresses are relative to the hydraulic problem (effective and total stresses produced by the thermal forcing are equivalent).

hydraulic problems given that their temporal scale can be very different. In fact, the hydraulic transient conditions would only be relevant for the times during which thermal effects were localized near the well.

It should be noted that pressure and temperature effects are extremely sensitive to stiffness. Although this is apparent in equations (3.4) and (3.5), it is also observed in Figure 3.6. Pressure driven displacements depend on the inverse of stiffness (i.e. displacements decrease when stiffness increases). However, thermal deformation only depends on the thermal expansion coefficient. The opposite occurs in the case of stresses. Thermal stresses are proportional to stiffness, while hydraulic stresses (total and effective) are independent of stiffness. This means that a non isothermal injection in a very stiff reservoir (e.g. granitic rock) will produce smaller deformations and much more stress than in a soft reservoir. Nev-

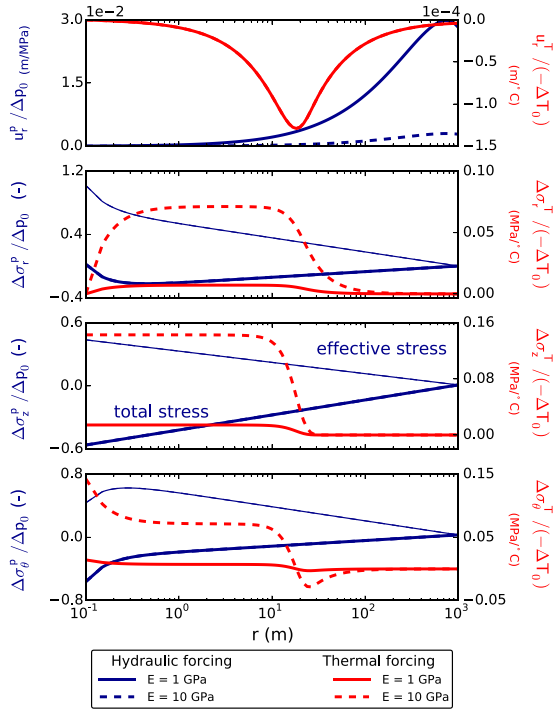

Figure 3.6: Hydraulic and thermal effects for two different reservoir stiffness, normalized with respect to the perturbation imposed at the well, for the radial unconstrained case (Scenario 2) and time = 100 days. Effective stresses are relative to the hydraulic problem (effective and total stresses produced by the thermal forcing are equivalent). Note that stresses due to the hydraulic forcing for two different stiffness values are overlapped, as they do not depend on it. The same occurs for the displacements due to the thermal forcing.

ertheless, if the injected water is in thermal equilibrium with the reservoir, a stiff reservoir will undergo the same stress variation as a soft reservoir.

The last two figures have considered the absence of lateral constraints, which may be unrealistic. If a lateral constraint is considered (Scenario 1), expansion due to overpressure and contraction due to cooling are balanced by contrasting behavior. Such behavior is evident in the unidirectional case (Fig. 3.7) and induces compressive (negative values) total stress in response to overpressure and tensile total stress in response to cooling. This is valid both for horizontal and vertical stresses. The induced stresses are uniform in space, therefore they also involve portions of the domain that have not been reached by the perturbation. Moreover, they increase with time, since they are function of the integral of the perturbation over space (eq. (3.15)). By contrast, in the radial case, as stated

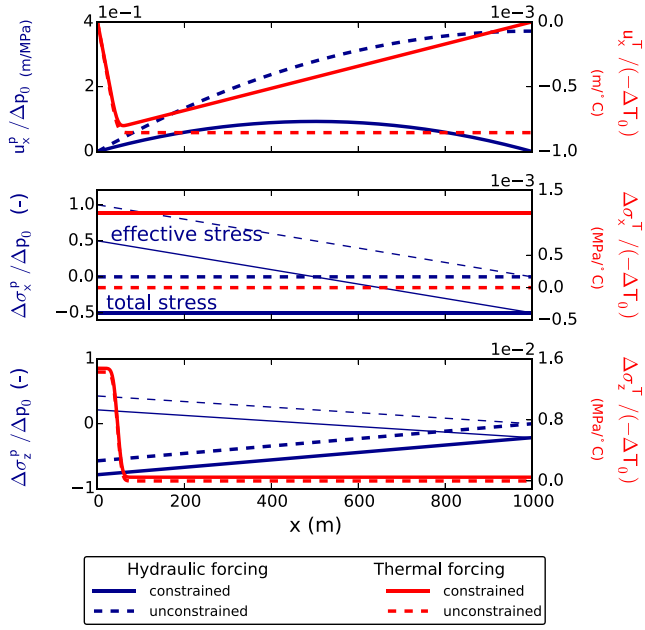

Figure 3.7: Hydraulic and thermal effects for the two external boundary conditions considered (Scenario 1 and 2), normalized by the perturbation imposed at the well, for the unidirectional case and time = 300 days. Effective stresses are relative to the hydraulic problem (effective and total stresses produced by the thermal forcing are equivalent).

above, the radial total stress undergoes a change, even when no lateral constraint is considered. This is because the axial symmetry drives an arc-like response of the formation and acts like a lateral constraint. In fact, very slight differences between Scenario 1 and 2 may be observed for both the hydraulic and thermal problems (Fig. 3.8). Analytically, this is shown by the fact that the constant term (i.e., independent of r, which comes from the BCs terms in eq. (3.23)) is very small for both scenarios (Table 3.2) if the well radius r_0 is small and the domain dimension R is great. For this reason, there is no total stress variation where the perturbation has not arrived. Moreover, the constrained unidirectional case and the two scenarios of the radial case are sensitive to the reservoir dimension, which is logical.

Hitherto, the results were normalized with respect to the imposed boundary perturbation. Although this is useful to generalize the results, it does not facilitate the comparison of the magnitudes of the effects of pressure and temperature variations given their very different scales. In order to better understand real magnitudes, we shall consider the case of EGS, which typically concerns very stiff rocks ($E = 10$ GPa) at great depth (more than 4 km), at approx. 150°C according

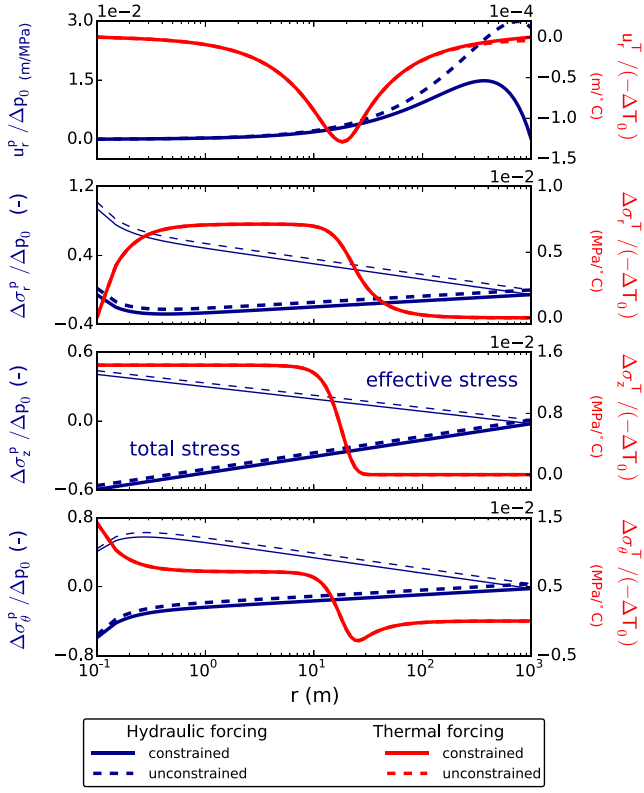

Figure 3.8: Hydraulic and thermal effects for the two external boundary conditions considered (Scenario 1 and 2), normalized by the perturbation imposed at the well,for the radial case and time = 100 days. Effective stresses are relative to the hydraulic problem (effective and total stresses produced by the thermal forcing are equivalent). Note that the boundary condition slightly affects the induced stresses.

to the geothermal gradient. The fluid is generally injected at a temperature of around 50°C so the temperature drop at the well is ΔT_0=100°C. Considering an injection flow rate Q of 20 kg/s along 200 m of screened well, the unitary flow rate q_0 is 0.1 kg/s/m^2; assuming permeability k of 10^{-15} m^2, and steady state conditions with R=1000 m, the boundary imposed condition for the hydraulic problem Δp_0 is almost 10 MPa, which is similar to the overpressure measured at the well at the Soultz HDR site (Baisch et al., 2010). The effects of these pressure and temperature variations, as well as their superposition, are plotted in Figure 3.9 for an injection time of 100 days. Only effective stresses are shown, as they are the ones that control failure. It may be observed that the effective stress variations due to the thermal problem are greater than the variations due

to the hydraulic problem given the adopted conditions. As regards failure, both hydraulic and thermal problems lead to the reduction of compressive stresses, thus increasing instability. However, the non-isotropic variations of stresses may cause an increase in or a reduction in the deviatoric stress depending on the initial stress tension, thus destabilizing or stabilizing the equilibrium.

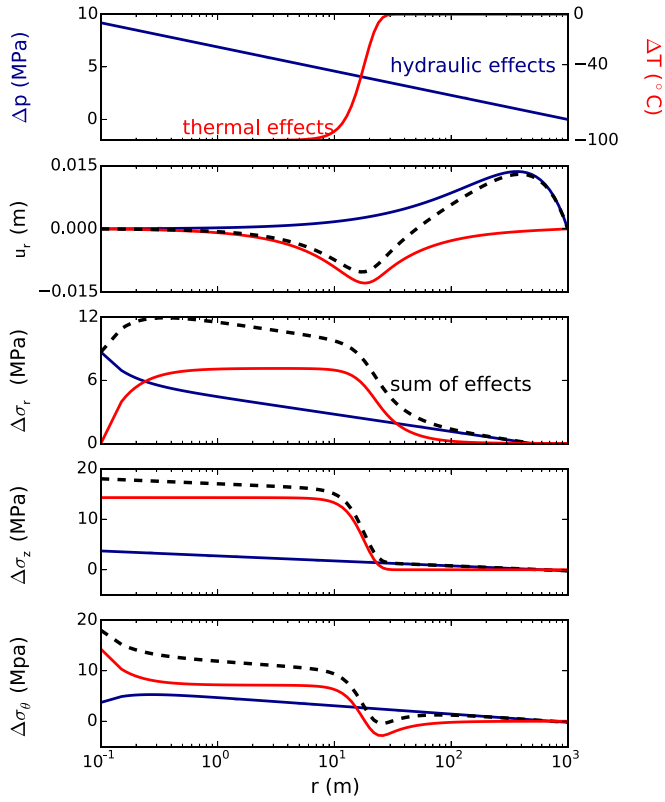

Figure 3.9: Hydraulic, thermal effects and their superposition calculated for typical EGS site values, for the radial case and time = 100 days. Only effective stresses are plotted. Results are relative to the constrained case (Scenario 1), but we have observed that the external boundary condition slightly affects the induced stresses.

3.4 Conclusions

A novel approximate but accurate solution was proposed for advective-conductive heat transport with divergent radial flow. The solution is then applied to the problem of mechanical equilibrium. This results in easy-to-use analytical solutions to displacements and stress induced by non-isothermal injection. The solution is

valid under plain strain conditions neglecting coupled effects (e.g., variations in viscosity due to changes in temperature or variations in pressure driven by thermal strains). The resulting expressions can be useful for testing numerical codes and for providing a rapid assessment of the system response to an alteration and an evaluation of the controlling parameters. The validity of the solution was verified and the results are fairly accurate. However, it should be pointed out that the method is valid only for advection-dominated problems and is a satisfactory approximation for Peclet numbers greater than 10, which is not unusual. The mechanical response is very sensitive to heterogeneity, dimensionality or boundary conditions. Care should therefore be taken when applying this solution to situations different from the ones for which it was derived.

The solution allowed us to gain further insight into some well known and not so well known features of mechanical response to non-isothermal injection.

- Pressure driven stresses are independent of the elastic properties of the medium and depend exclusively on the injection rate. By contrast, thermal stresses are proportional to elastic moduli. The opposite occurs in the case of displacements.
- Thermal impacts driven by a non-isothermal continuous injection are cumulative, i.e. displacements and stresses are maxima around the thermal front but do not decrease once the front has passed.
- The effect of the outer BC is extremely sensitive to the flow dimension. In the case of the steady unidirectional flow, stress buildup is zero if the displacement is unconstrained at the outer boundary but it is equal to half the total pressure drop if displacement is constrained. In the radial case, the outer BC only affects pressure driven displacements in the outer region. The impact is small on pressure driven stresses and it is negligible on temperature driven displacements and stresses.

4

Thermal Coupling May Control Mechanical Stability of Geothermal Reservoir During Cold Water Injection *

4.1 Introduction

Geothermal energy production from deep hot rocks requires a high permeability heat exchanger for economic efficiency. The typical procedure entails intercepting natural pre-existing discontinuities, such as faults and joints, and enhancing their permeability by means of stimulation. Hydraulic stimulation is the most widely used method. It involves the massive injection of a large volume of water (several thousand cubic meters) at high flow rates to increase the downhole pore pressure, which tends to induce shearing along the fracture planes (Pearson, 1981). In this way permeability is enhanced due to dilatancy, especially in the direction perpendicular to shear (Barton et al., 1985; Yeo et al., 1998; Mallikamas and Rajaram, 2005).

Microseismic events occur during hydraulic stimulation. Induced seismicity is typically weak (M<2; Evans et al., 2012) and certifies the effectiveness of the operation. However, these events are sometimes of sufficient magnitude to be felt by the local population. For example, seismic events with magnitude greater than 3 occurred at the Basel Deep Heat Mining Project in Switzerland (Häring et al., 2008) and at the Hot Dry Rock Project of Soultz-sous-Forêts in France (Cornet et al., 1997; Baria et al., 2005). This causes a negative impact on the local population and may compromise the continuation of the project. Hence,

*This chapter is based on the paper by De Simone et al. (2013).

understanding the mechanisms triggering these induced micro-earthquakes is important to properly design and manage geothermal stimulation and operation so as to prevent them.

Induced seismicity occurs when failure conditions are reached, either at an existing fracture or at a newly created one. It is widely believed that the main cause of failure during hydraulic stimulation is overpressure (Shapiro et al., 1999; Shapiro and Patzig, 2003; Parotidis et al., 2004). Indeed, overpressure produces a reduction of effective stresses that can cause the fracture to yield. Rutqvist and Stephansson (2003) provide an accurate review of the hydromechanical coupling in fractured rock and point out its relevance in the geothermal field. However, pore pressure cannot be considered the only cause of induced seismicity. Microseismic events at Soultz-sous-Forêts (Baisch et al., 2010; Evans et al., 2005) and Basel (Häring et al., 2008; Ripperger et al., 2009) were still occurring once injection stopped and often the largest microseisms occurred after the end of injection, like in Basel. These post injection events cannot be explained by pressure diffusion alone, because its magnitude decreases quickly with time (Delleur, 1999).

Interestingly, injected water was cold both at Basel and Soultz. The temperature contrast between the hot reservoir and the injected water (at atmospheric conditions at surface) was large. This produces a significant contraction of both the fracture filling and the surrounding rock, leading to an additional reduction in effective stresses, which has to be taken into account (Majer et al., 2007). This effect is confirmed by the measurements taken at the Geysers geothermal steam field (Santa Rosa, California), where the observed seismicity is not directly related to overpressure (National Academy of Science, 2012). There, the large temperature difference between the injected fluid and the deep rock produced a significant cooling of the geothermal reservoir (Mossop and Segall, 1997), which caused thermal contractions of the rock, affecting the in situ stress state. In short, thermal effects should be considered to better understand the processes involved in geothermal reservoir stimulation (Segall and Fitzgerald, 1998). To achieve this, coupled thermo-hydro-mechanical analyses are necessary.

Thermoelastic effects in geothermal systems have been studied by some authors (e.g., Ghassemi, 2012). They performed thermo-hydro-mechanical models of cold water injection into a planar fracture (Kohl et al., 1995; Ghassemi et al., 2007, 2008; Ghassemi and Zhou, 2011) or in a fracture network (Kolditz and

Clauser, 1998; Bruel, 2002; McDermott et al., 2006). Nevertheless, most of them solely point out the perturbations generated within the fracture or at the fracture's surface, but not the effects on the surrounding rock mass.

We conjecture that the thermal effects developing in the cooled part of the rock matrix may play an important role in triggering induced seismicity. In fact, the intact rock has a greater stiffness than the fracture, so that thermal stress changes may indeed be large, which could explain how seismic events are triggered. To investigate this, we simulate the hydraulic stimulation of an idealized fracture zone embedded in an intact rock matrix. Hydraulic and thermal effects are studied by means of fully coupled thermo-hydro-mechanical (THM) simulations of cold water injection into the hot fracture zone/matrix system. The results of the THM simulation are compared to those of a hydro-mechanical (HM) simulation (i.e. injection of water in isothermal equilibrium with the hot rock) in order to estimate the impact of the thermal effects.

4.2 Methods

4.2.1 Conceptual Model

To investigate the effect of the cooling front caused by cold water injection on thermoelastic strain, we perform coupled HM and THM numerical simulations of water injection into a rock mass containing a zone of discontinuities. An idealized geometry consisting of a planar fracture zone (corresponding to joints or faults) of 1 m thickness embedded into an intact rock mass is considered. The fracture zone is treated like a continuous porous medium. This assumption is made considering that faults often consist of a fault core with a thickness of few centimeters embedded into a highly damaged zone of some tens of centimeters (Gudmundsson, 2004; Cappa and Rutqvist, 2011b). The whole fracture zone is surrounded by the host rock, which is generally less permeable and stiffer than the fracture zone. In fractured crystalline rocks the intrinsic permeability of the intact rock matrix may be some 5 orders of magnitude smaller than that of the fault zone (Rutqvist and Stephansson, 2003). This difference in hydraulic properties converts the fault zone into a preferential flow path.

The numerical simulations calculate deformations and changes in the stress field due to cold water injection. Linear elasticity is assumed for the whole model.

In order to evaluate the potential induced seismicity, we perform a slip tendency analysis (Byerlee, 1978; Morris et al., 1996; Streit and Hillis, 2004). We consider the Mohr-Coulomb failure criterion (Jaeger et al., 2007)

$$\tau_r = c + \psi\, \sigma'_n \,, \tag{4.1}$$

where τ_r is the critical shear stress, c is cohesion, σ'_n is effective normal stress and ψ is friction coefficient, which is often expressed in term of the angle of friction ϕ ($\psi = \tan\phi$). For cohesion-less materials ($c = 0$), sliding occurs when the shear stress τ equals the critical shear stress τ_r, i.e., when the ratio of the shear stress to effective normal stress equals the friction coefficient ψ

$$\frac{\tau}{\sigma'_n} = \tan\phi \,. \tag{4.2}$$

We use this equation to estimate the mobilized friction angle ϕ_{mob} on critically oriented planes (i.e., the one for which ϕ_{mob} is maximum). This value quantifies the shear slip tendency along a plane, because it represents how close is the stress state to the failure envelope.

4.2.2 Mathematical Model

According to linear theory of poro-thermoelasticity (McTigue, 1986), stresses are a function of strain, fluid pressure and temperature

$$\Delta\boldsymbol{\sigma} = K\varepsilon_v\mathbf{I} + 2G\left(\boldsymbol{\varepsilon} - \frac{\varepsilon_v}{3}\mathbf{I} + \frac{1}{2G}\Delta p_f\mathbf{I} + \frac{3K}{2G}\alpha_T\Delta T\mathbf{I}\right) \,, \tag{4.3}$$

where $\boldsymbol{\sigma}$ is the total stress tensor (compression positive), ε_v is volumetric strain, $\mathbf{I}$ is the identity matrix, $\boldsymbol{\varepsilon}$ is the strain tensor, $K = E/(3(1-2\nu))$ is the bulk modulus, $G = E/(2(1+\nu))$ is the shear modulus, E is the Young's modulus, ν is Poisson ratio, p_f is the fluid pressure, α_T is the linear thermal expansion coefficient and T is temperature. Biot coefficient has been assumed to be 1 because the rock compressibility is negligible compared to that of the grains. Moreover, this value is the least favorable, because it leads to the strongest hydromechanical coupling (see also Zimmerman, 2000). Notice that a temperature drop implies an isotropic drop in stresses equal to $3K\alpha_T T$, which can be very large for stiff rocks.

To solve the mechanical problem, the momentum balance has to be satisfied. If the inertial terms are neglected, it reduces to the equilibrium of stresses

$$\nabla \cdot \boldsymbol{\sigma} + \mathbf{b} = \mathbf{0} \,, \tag{4.4}$$

where $\mathbf{b}$ is the vector of body forces.

Equation (4.3) is coupled with the flow equation through fluid pressure. Assuming that there is no external loading and neglecting solid phase compressibility, fluid mass conservation of the fluid can be written as

$$\frac{\phi}{K_f}\frac{\partial p_f}{\partial t} + \nabla \cdot \frac{\mathrm{d}\mathbf{u}}{\mathrm{d}t} + \frac{1}{\rho}\nabla \cdot (\rho \mathbf{q}) = f_w \,, \tag{4.5}$$

where ϕ is porosity, $1/K_f$ is water compressibility, t is time, $\mathbf{u}$ is the solid displacement vector, $\mathbf{q}$ is the water flux and f_w is an external supply of water. Notice that the second term represents the rate of change in volumetric strain (i.e., porosity). The water flux is given by Darcy's Law

$$\mathbf{q} = -\frac{k}{\mu(p_f, T)} \left[\nabla p_f + \rho(p_f, T)\mathbf{g}\nabla z\right] \,, \tag{4.6}$$

where k is the intrinsic permeability, $\mathbf{g}$ is gravity, z is the vertical coordinate, and μ and ρ are respectively the fluid viscosity and density, which are function of pressure and temperature. Note that the flow equation (Eq. (4.5)) is coupled to the mechanical equation (Eq. (4.3)) through the volumetric strain (second term in the left-hand side of Eq. (4.5)), which can be expressed as the divergence of the displacement vector.

An additional equation governing energy balance must be accounted for thermo-hydro-mechanical coupling,

$$\begin{aligned} &\frac{\partial \left(c_s \rho_s \left(1-\phi\right) T + c_f \rho \phi T\right)}{\partial t} \\ &\quad + \nabla \cdot \left(-\lambda \nabla T + c_f \rho T \mathbf{q} + c_f \rho \phi T \frac{d\mathbf{u}}{dt} + c_s \rho_s (1-\phi) T \frac{d\mathbf{u}}{dt}\right) = f_Q \quad , \end{aligned} \tag{4.7}$$

where c_s and c_f are the specific heat capacity of the solid and the fluid, respectively, ρ_s is the solid density, λ is the equivalent thermal conductivity and f_Q is an external/internal supply of energy.

Equations (4.3), (4.5), (4.6) and (4.7) show the strong coupling of the problem

(Zimmerman, 2000). Water pressure influences stresses and strains and it is in turn influenced by the latter, which also change porosity and thus intrinsic permeability. Temperature variations affect stresses directly (see Eq. (4.3)), but also indirectly because water flux depends on temperature by means of density and viscosity. Temperature variation is also affected by water flux because it affects the advective transport of energy.

4.2.3 Numerical Model

Simulations are carried out with the finite element numerical code CODE_BRIGHT (Olivella et al., 1994, 1996) that solves coupled thermo-hydro-mechanical problems in porous media.

The model domain consists of a homogeneous radial horizontal 1 m-thick fracture zone underlain and overlaid by a 250 m-thick low-permeability matrix. We model a 2D vertical section of the formation making use of the axisymmetry around the vertical well axis. The top of the fracture zone is located at a depth of 4250 m. The lateral extension is 2000 m, which ensures that pressure and thermal perturbations are contained inside the modeled domain and are not affected by spurious boundary effects.

The fracture zone is softer than the intact matrix. The value of the Young's modulus for the intact rock matrix is assumed to be 10000 MPa, typical of crystalline rock (Goodman, 1989; Hoek, 2006). In fault zones the stiffness is usually lower (Schultz, 1996; Gudmundsson, 2004; Faulkner et al., 2006) and can vary largely depending on alteration. Due to this uncertainty, a very low value of 100 MPa is considered and a sensitivity analysis is performed. For simplicity both the fracture zone and the fractures contained in the intact rock are considered cohesion-less. The parameters assumed for the simulations are shown in Table 4.1 (values of intrinsic permeability and thermal conductivity are considered constant during the simulations for simplicity).

Initial conditions correspond to hydrostatic pressure, a geothermal gradient of 33°C/km with a surface temperature of 5°C (i.e., 150°C at the fracture zone) and lithostatic vertical stress. The stress regime is considered axisymmetric with the vertical stress greater than the horizontal stresses following the relationship $\sigma'_h = 0.5\sigma'_v$. Conditions of constant pressure and temperature are imposed at the

Table 4.1: Properties of the fracture zone and the intact matrix.

Parameters	Fracture zone	Matrix	Units
Intrinsic Permeability	10^{-13}	10^{-18}	m^2
Porosity	0.5	0.01	-
Young's Modulus	100	10000	MPa
Poisson Ratio	0.3	0.3	
Thermal Conductivity	2.5	1.5	$Wm^{-1}K^{-1}$
Longitudinal Dispersivity for heat	1	1	m
Transverse Dispersivity for heat	0.1	0.1	m
Linear thermal expansion	$1x10^{-5}$	$1x10^{-5}$	$°C^{-}1$
Specific heat for solid phase	800	800	$Jkg^{-1}K^{-1}$

outer boundary of the model, whereas no flow conditions are adopted for the other boundaries. The mechanical boundary conditions are the lithostatic stress on the upper boundary and in the other boundaries no displacement perpendicular to them. Initial and boundary conditions and a schematic representation of the geometry are shown in Figure 4.1.

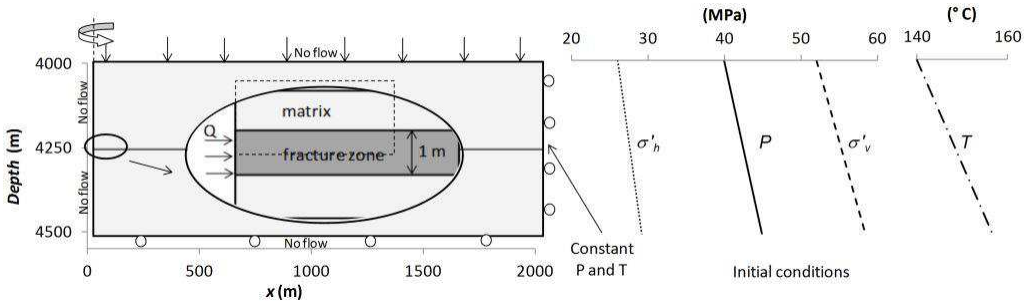

Figure 4.1: Model geometry, boundary and initial conditions – Liquid pressure (solid line), horizontal (dotted line) and vertical (dashed line) effective stress, temperature (dot-dashed line) vs depth. The dashed box indicates the location of the reference area shown in Figure 4.2

Water is injected in the fracture zone with a mass flow rate of 3 kg/s, uniformly distributed along the contact between the fracture zone and the well, which has a radius of 0.5 m. Water injection lasts for 10 days. Unless the opposite is explicitly stated, all figures displayed hereon contain results at this time. In the THM simulation the temperature of the injected water is assumed to be 60°C.

A structured mesh with 8925 structured quadrilateral elements is used. The mesh is refined in the areas affected by the perturbations. In order to obtain a

good accuracy of the results without using a huge number of elements, the element size is smaller close to the injection well, in the fracture zone and its surroundings and increases progressively, varying from a minimum of about $8x10^{-2}$ m^2 next to the injection well in the fracture zone to a maximum of 700 m^2 close to the outer boundary.

4.3 Results

4.3.1 HM and THM coupling

Water injection produces an increase in fluid pressure, which extends further in the fracture zone than in the matrix (Fig. 4.2b) due to the large contrast in hydraulic conductivity between the materials. After 10 days of injection, overpressure (increase of pressure with respect to the initial value) propagates several hundreds of meters within the fracture zone (Fig. 4.3), but only a few meters into the matrix.

Temperature propagates much slower than overpressure along the fracture zone (Fig. 4.2a). After 10 days of cold water injection, the cooling front propagates within the first 20 m of the fracture zone in the longitudinal direction and penetrates 1 m into the matrix in the transverse direction (Fig. 4.2a). Heat transport in the fracture zone is the result of combined advection and conduction, whereas it is mainly governed by conduction in the matrix, where water flow is negligible.

The temperature reduction increases fluid viscosity, thus decreasing hydraulic conductivity. As a result, injection of cold water produces a larger overpressure than injection of warm water (Fig. 4.3). With the given conditions, the resulting overpressure close to the well is almost twice in the THM simulation than in the HM simulation (Fig. 4.2b and 4.3). The decrease of overpressure with the logarithm of distance from the well, which should be linear for a homogeneous medium, exhibits two different slopes for HM and THM simulation in the first 20 meters, because of the temperature difference. Note that, in reality, the decrease in hydraulic conductivity caused by the increase in viscosity of the injected cooler water may be more than compensated by the increase caused by thermal contraction of the matrix, which tends to open the fracture zone, thus increasing

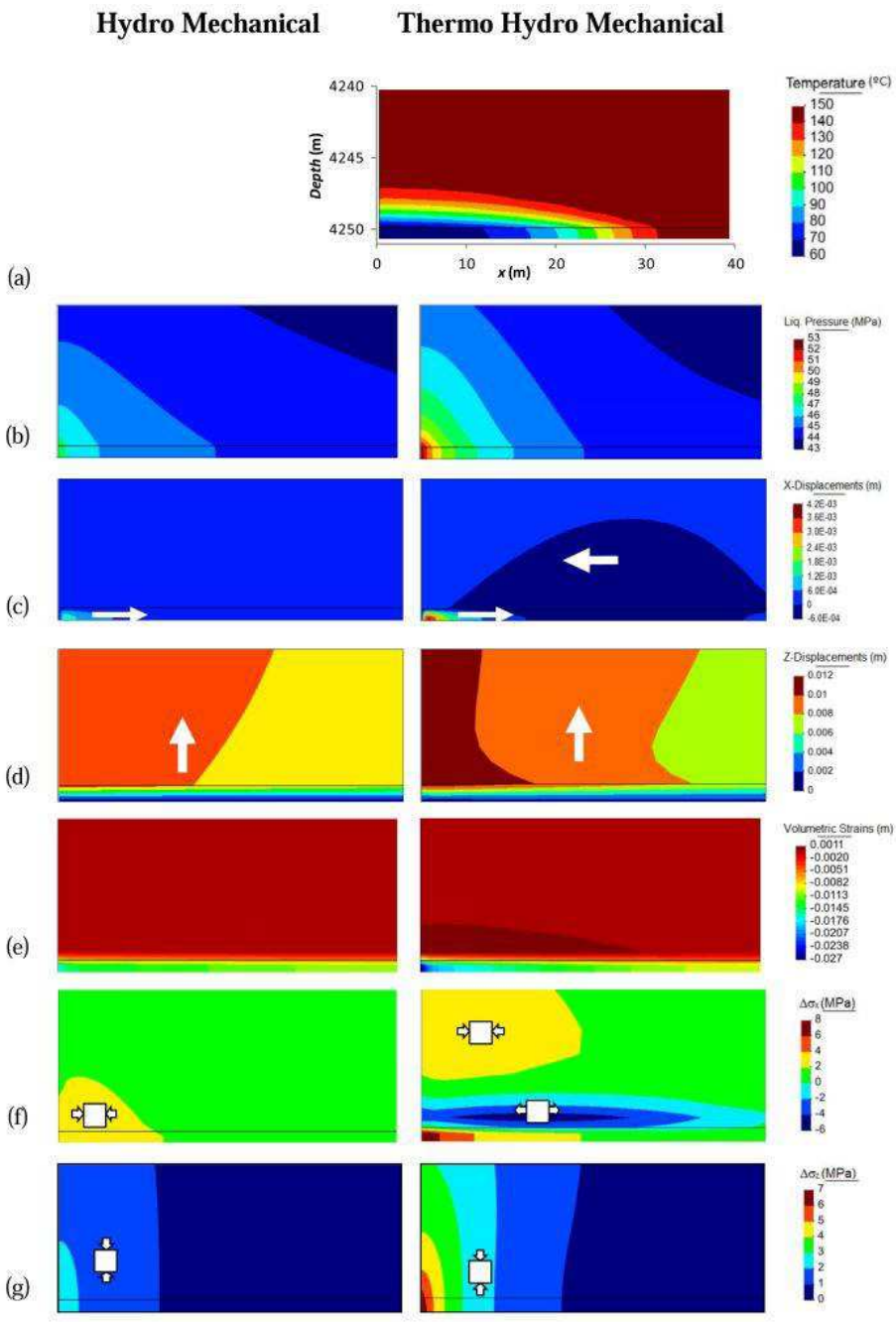

Figure 4.2: Distribution of temperature (a), liquid pressure (b), horizontal (c) and vertical displacements (d), volumetric strains (e), total horizontal (f) and vertical stresses variations (g) for cold water injection and injection of water in thermal equilibrium with the formation in the reference area (recall Fig. 4.1). The sign criterion for deformation in (e) is that positive volumetric strain indicates contraction and negative volumetric strain means expansion. Positive displacements (c-d) are oriented as the corresponding axis.

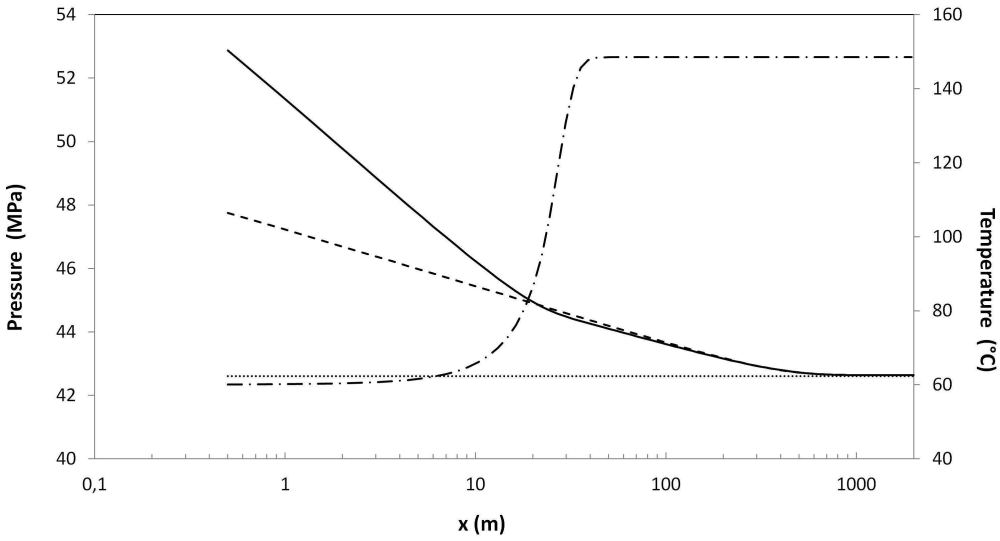

Figure 4.3: Liquid Pressure (dashed line HM, solid line THM) and temperature (dot-dashed line) vs distance inside the fracture zone after 10 days of water injection. The dotted line indicates the undisturbed liquid pressure.

its permeability. This effect has not been simulated in this model, as we consider constant permeability.

Effective stresses decrease as water pressure increases. As a consequence, the whole medium deforms, with greater strains in the vertical direction than in the horizontal one, due to the horizontal orientation of the fracture zone (Fig. 4.2c and 4.2d). Water injection compresses the fracture zone causing horizontal displacements directed away from the well. The overpressure expands the fracture zone in the vertical direction causing displacements directed upwards in the upper side and downwards in the lower side, which tends to open it. This hydraulic effect is superimposed in the THM simulation to the thermal perturbation that contracts the rock as it cools. Figure 4.4 displays the vertical and horizontal displacements as a function of depth for a section placed 3 m away from the injection well. The fracture zone expands as a result of overpressure in both HM and THM simulations. Indeed, the expansion in the fracture zone is larger when thermal effects are accounted for because the overpressure is larger than in the isothermal case (Fig. 4.4a). However, in the THM simulation, the cooled portion of the matrix undergoes a thermal contraction (see Fig. 4.2e), which leads to an increased opening of the fracture zone (i.e., larger vertical displacement in Fig. 4.4c).

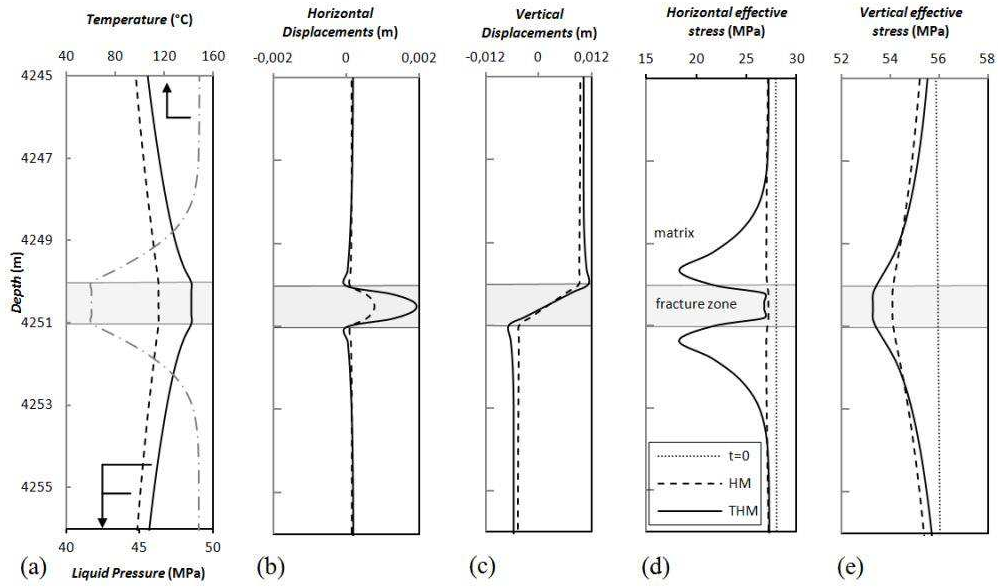

Figure 4.4: Vertical profile of liquid pressure and temperature (a), horizontal (b) and vertical (c) displacements, horizontal (d) and vertical (e) effective stresses for a section placed 3 m away from the well. The solid line represent the THM solution, the dashed line represents the HM solution and the dotted line the initial situation.

Figures 4.4d and 4.4e display the variations of effective stresses due to pressure and temperature perturbations. In the HM simulation, the overpressure and the stress perturbation affect mainly the fracture zone because water flow in the matrix is negligible. Vertical effective stresses decrease more than the horizontal effective stresses because the fracture zone can deform more significantly in the vertical direction than in the horizontal direction. This behavior is also observed in the THM simulation, but with a greater effective stress reduction due to the greater overpressure. However, the most relevant effects of the THM coupling concern the region of the matrix affected by the temperature drop. Here the stress reduction due to thermal effects is much greater than in the fracture zone because of its higher stiffness (recall Equation (4.3)). Additionally, the horizontal effective stress reduces more than the vertical one, leading to an increase in deviatoric stress.

4.3.2 Rock Stability and Potential Induced Seismicity

We represent the stress state by means of the Mohr circles. Figure 4.5 displays the stress state for points placed 3 m away from the well at different depths: inside

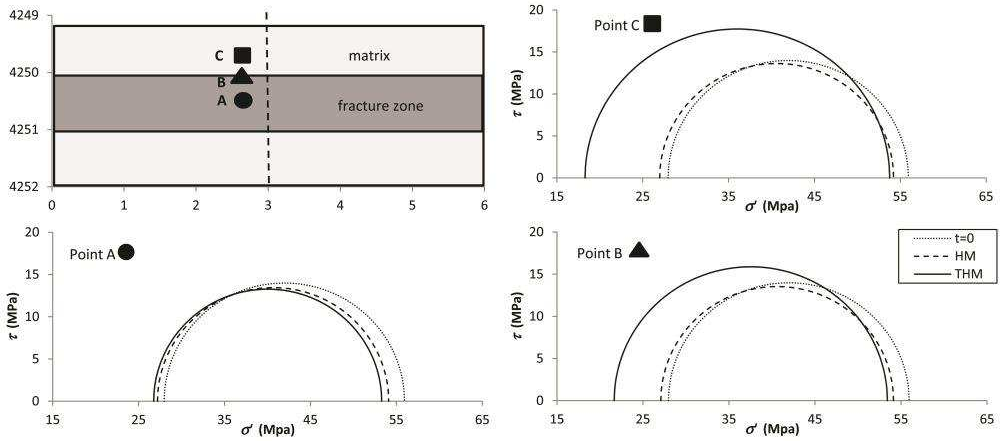

Figure 4.5: Stress field after 10 days of injection for points placed 3 m away from the injection well at different depths. The solid line represent the THM solution, the dashed line represents the HM solution and the dotted line the initial situation.

the fracture (point A), at the contact between the fracture and the matrix (point B) and inside the matrix at 0.4 m from the contact (point C). Results of the HM simulation show that the vertical effective stress decreases more than the horizontal one. This produces a reduction of the size of the Mohr circle for all points. In the case of THM simulation, the thermal contraction causes an increase of the deviatoric stress in the cooled section of the matrix. This results in a bigger Mohr circle for points B and C. Note that the Mohr circle size is greater in the latter point, reflecting a more critical situation. Inside the fracture zone (point A) the results of THM and HM simulation are similar and depict a more stable condition.

According to the Mohr circles, in the fracture zone and its surroundings the mobilized friction angle decreases in the HM simulation (Fig. 4.6). As the mobilized friction angle expresses the proximity to failure conditions, this reduction points to a more stable situation, which is consistent with the fact that we are assuming a normal initial stress tensor (vertical stress larger that horizontal stresses). Under these conditions, opening tends to concentrate on vertical fractures. On the other hand, in the THM simulation significantly higher friction angles are mobilized in the portion of matrix close to the fracture. However, the mobilized friction angle becomes smaller than the original one (that is about 19°) in the central part of the fracture zone. Here, thermal effects have little influence because hydraulic effects dominate (Fig. 4.7).

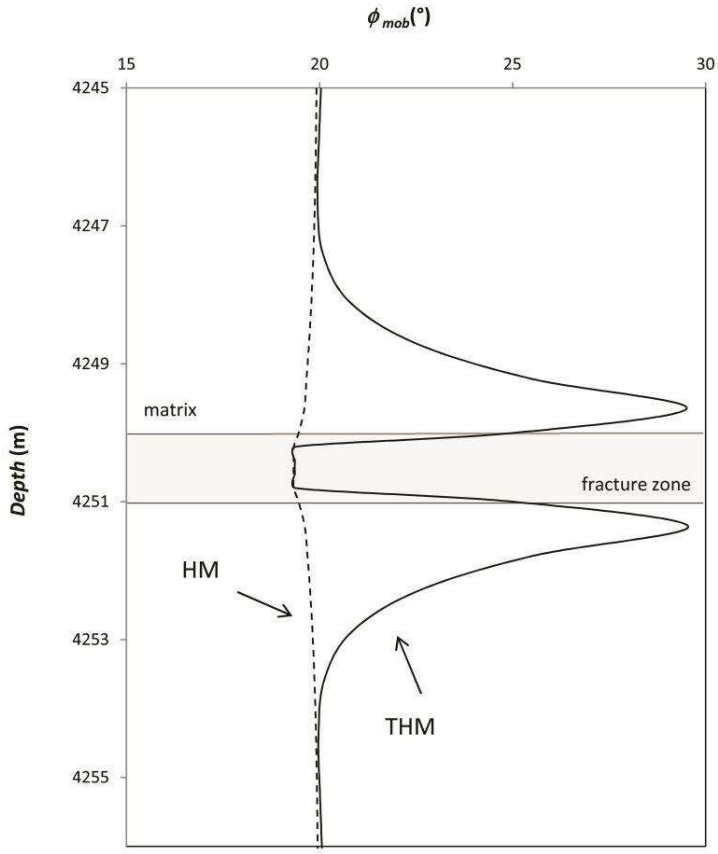

Figure 4.6: Vertical profile of the mobilized friction angle for a section placed 3 m away from the injection well. Dashed line represents HM simulation and solid line represents THM simulation.

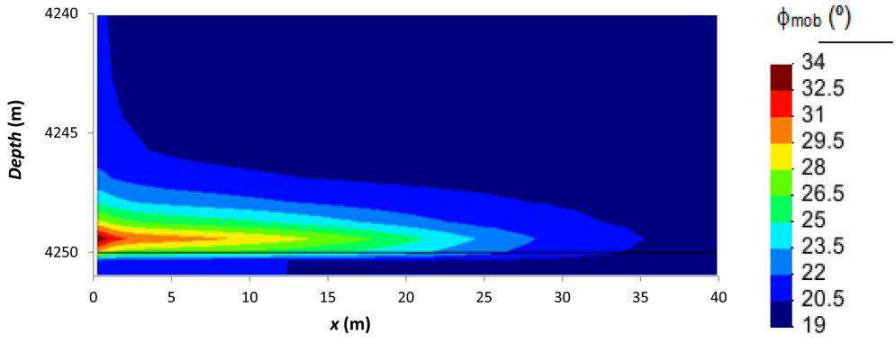

Figure 4.7: Distribution of the mobilized friction angle in the reference area for THM simulation. The mobilized friction angle quantifies the shear slip tendency along critically oriented planes. The area in the intact rock matrix close to the injection well results to be the most critical for slip potential and induced seismicity.

4.3.3 Sensitivity analysis

Sensitivity to stiffness of the fracture zone

We investigate the effects of the fracture zone's stiffness on the HM and THM simulations. Young's modulus is increased from 100 to 5000 MPa. As expected, the increase in stiffness leads to a significant reduction of horizontal and vertical displacements in the HM simulations (Fig. 4.8). In the THM simulation this behavior is superimposed to the thermal contraction, which further reduces the displacements to the point that vertical displacements even become negative within the fracture zone. That is, thermal effects dominate hydraulic effects.

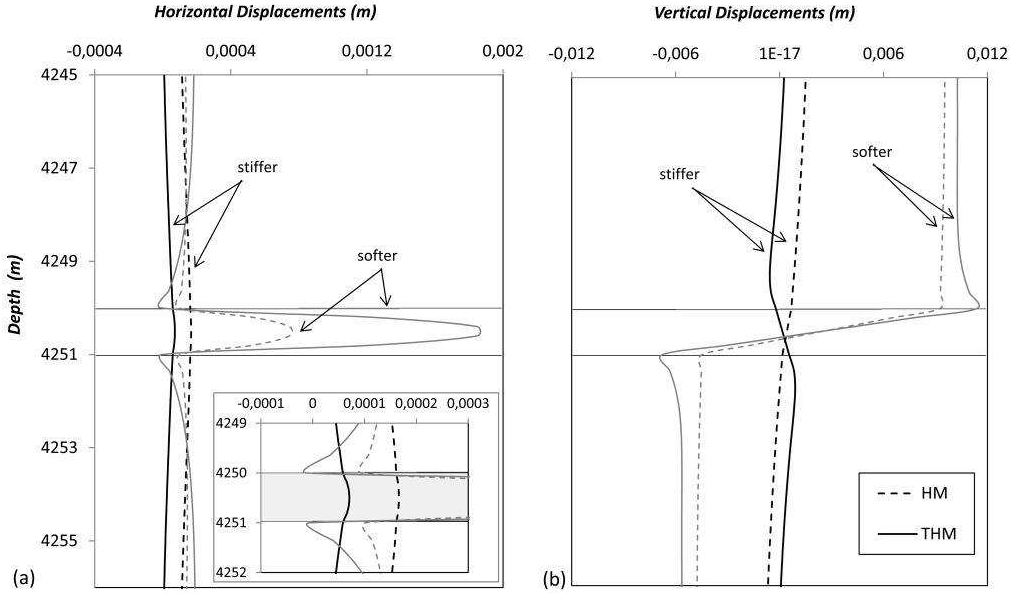

Figure 4.8: Sensitivity to the stiffness of the fracture zone. Vertical profile of horizontal (a) and vertical (b) displacements for a section placed 3 m away from the well. The results of a stiffer fracture zone (E=5000 MPa) are in black, while the ones of a softer fracture zone (E=100 MPa) are in grey. The dashed lines represent the HM simulation and the solid lines the THM simulation. Fig. (a) contains an enlargement of the horizontal displacements in the fracture zone.

Lower rock compressibility yields smaller storage coefficients. This results in slightly higher overpressures, because the hydraulic response to fluid injection is faster. This fact provokes a greater reduction in effective stresses (in both the HM and THM simulations) with respect to the simulation with a softer fracture zone (Fig. 4.9a and 4.9b). However, the most relevant sensitivity to the stiffness of the fracture zone concerns the thermal perturbation of the effective stresses. Indeed,

according to Eq. (4.3), the thermal stress is proportional to the Young's modulus. As a consequence, thermal stresses become significant also in the fracture zone when it is stiffer. Thus, a stiffer fracture zone reduces stability and yields a higher mobilized friction angle (see Fig. 4.9c) in the fracture and in the fracture-matrix contact when cold water is injected.

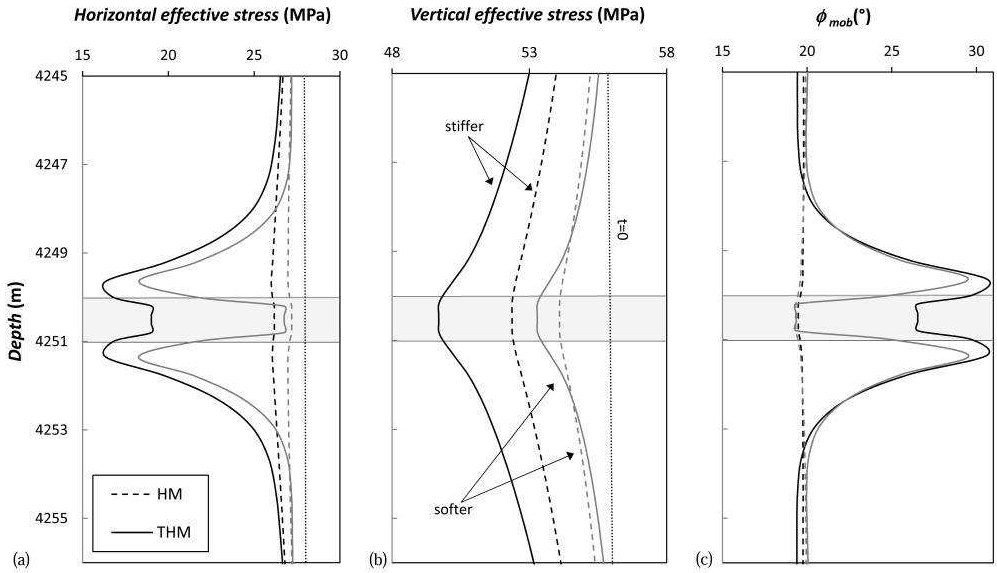

Figure 4.9: Sensitivity to the stiffness of the fracture zone. Vertical profile of horizontal (a) and vertical (b) effective stresses and of mobilized friction angle (c) for a section placed 3 m away from the well. The results of a stiffer fracture zone (E=5000 MPa) are in black, while the ones of a softer fracture zone (E=100 MPa) are in grey. The dashed lines represent the HM simulation, the solid lines the THM simulation and the dotted lines represent the initial situation.

Sensitivity to initial stress condition

Sensitivity to initial stress condition is investigated taking into account a reverse faulting stress regime, in which the maximum principal stress is horizontal, with a lateral earth pressure coefficient of 2, i.e., $\sigma'_h = 2\sigma'_v$. The change of the initial stress field evidently does not affect the net variation of effective stresses, which are the same as in the normal faulting stress regime. Nevertheless, since now the maximum principal stress is horizontal, the effective stress perturbation results in an increase of the size of the Mohr circle in the HM simulation and a decrease in the THM simulation.

This leads to an opposite behavior with respect to the normal faulting stress regime: the mobilized friction angle in the matrix increases for isothermal injection and decreases for cold water injection (Fig. 4.10), but with a smaller magnitude because of the greater confining stresses.

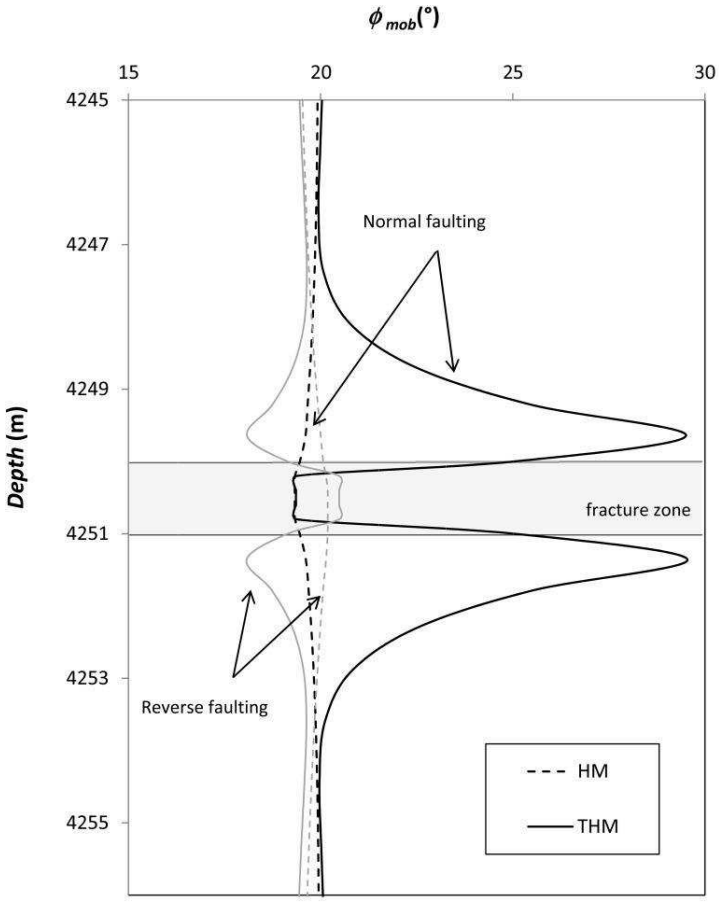

Figure 4.10: Sensitivity to initial stress conditions. Vertical profile of mobilized friction angle for a section placed 3 m away from the well. In black are the results for normal faulting stress regime and in grey for reverse faulting stress regime. Dashed lines represent the HM simulation and solid lines the THM simulation.

4.4 Discussion

Water injection produces an overpressure that reduces effective stresses and tends to open fractures. Even though overpressure acts isotropically and tends to expand the medium in all directions, confinement restricts expansion strains and implies an increase of total stresses, especially in the plane of the fracture. Thus,

the decrease of effective stresses is smaller than the increase in fluid pressure (Engelder and Fischer, 1994; Hillis, 2000). This effect is not predicted by uncoupled models that simply apply the variation of pore pressure on the effective stress state. In the case discussed here (a horizontal fracture zone) the fracture zone can deform more in the vertical direction than in the horizontal one (Fig. 4.4b and 4.4c), due to the geometry and the confinement conditions. This implies a greater increase in horizontal total stress than in vertical total stress (Fig. 4.2f and 4.2g). As a result, the effective stress decreases more in the vertical than in the horizontal direction (Fig. 4.4d and 4.4e). This means that the deviatoric stress decreases with increasing pressure. Therefore, under isothermal conditions, even though the Mohr circle displaces to the left, which causes instability, its size may also be reduced (Vilarrasa et al., 2010), which partly compensates this instability (Fig. 4.5). This behavior explains the induced seismicity observed in depletion processes, such as oil and gas extraction (Segall et al., 1994; Ferronato et al., 2008). In these processes the opposite occurs, i.e., deviatoric stress increases for decreasing pressure.

Acknowledging thermal effects leads to two main differences with respect to the isothermal case. First, cold water injection produces a higher overpressure because water viscosity increases for decreasing temperatures (Fig. 4.3 and 4.4a). This results in a larger effective stress reduction and larger expansion strains than in HM simulations. Second, cold water also contracts the rock, causing a decrease of both total and effective stress. The magnitude of the thermal stress is proportional to the temperature drop and to the stiffness of the material (Eq. (4.3)). Therefore, the thermal stresses reduction is much greater in the matrix than in the fracture zone. The net result is that the fracture zone is mainly affected by overpressure, which produces effects comparable to those of the isothermal case (Fig. 4.4d, 4.4e, 4.5 and 4.6). In contrast, the rock matrix undergoes greater thermal than hydraulic perturbations. In particular, the horizontal stress decreases more than the vertical one (Fig. 4.4d and 4.4e). This difference is due to the relatively large horizontal extent of the temperature perturbation and its limited vertical extent. In fact, in the horizontal direction the cooled zone extends about 20 meters, while in the vertical directions extends only a few meters. This provokes horizontal thermal stresses much greater than the vertical ones. As a result, in the cooled portion of the matrix (points B and C) the deviatoric stress and the Mohr circle's size increase (Fig. 4.5), denoting unstable conditions (Fig. 4.6). Note that the mobilized friction angle reaches value of 34° close to the well (Fig.

4.7), which would induce a microseism if a reasonable friction angle of about 30° is assumed (Zoback, 2007).

Actual stability conditions depend on the initial stress regime. When the maximum principal stress is horizontal (i.e., reverse faulting regime), the deviatoric stress increases for isothermal water injection and decreases for cold water injection in a horizontal fracture. Therefore, the most unfavorable conditions occur for isothermal injection and reverse faulting stress regime or for cold water injection and normal faulting stress regime (Fig. 4.10).

It is worth noting that the described phenomenon is valid for any orientation of the fracture zone. We built up and performed models considering the same configurations but with a vertical orientation of the fracture zone. The models confirm that the orientation has little influence on the general behavior. When we account for HM coupling, the decrease in effective stress caused by fluid injection is always smaller than overpressure and largest in the direction perpendicular to the fracture zone. On the other hand, when thermal perturbations are considered, the greatest effective stress reduction occurs in the direction of the fracture zone. In short, a vertically oriented fracture zone with reverse faulting stress regime acts in the same way than a horizontally oriented one with normal faulting stress regime (Fig. 4.11). Thus, when cold water is injected the critical situation is likely to take place when the greater stress acts normal to the fractures. This is the scenario of Basel and Soultz-sous-Forets, where strike slip faulting ($\sigma_H > \sigma_v > \sigma_h$; where σ_H and σ_h are respectively the maximum and the minimum principal horizontal stresses and σ_v is the vertical stress) is present and therefore shear slip occurs preferentially on vertical or sub-vertical fractures.

The hydro-mechanical and thermo-mechanical effects are very sensitive to the problem settings, i.e., stiffness and thickness of the fracture zone. What is clear is that the temperature drop leads to an unstable situation in the surrounding rock mass. This could eventually induce microseismicity in critically oriented fractures that are close to failure. Nevertheless, these thermal effects are relatively local (some 20 m for the conditions tested in this work) and cannot explain the seismic events with epicenters tens or hundreds of meters far from the injection point. It could be conjectured that these far events are provoked by a cascade effect (Häring et al., 2008). Testing this conjecture requires non-linear simulations, which are planned as future work.

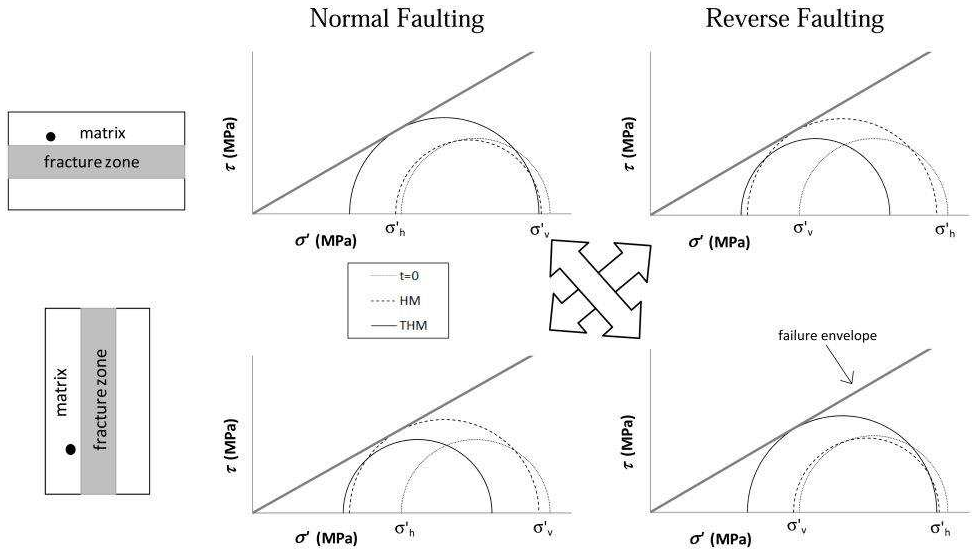

Figure 4.11: Schematic description of the stress state changes in the case of horizontally and vertically oriented fracture zone under different stress regimes (for a point placed in the matrix close to the fracture zone). The solid line represents the THM solution, the dashed line represents the HM solution, the dotted line the initial situation and the grey thick line represents the failure envelope.

It should be lastly underscored that hydro-mechanical and thermo-mechanical processes occur with different response times. Once the injection stops, the hydro-mechanical perturbation will quickly disappear, while the cooling front will continue to penetrate slowly into the rock mass. In this way thermal contribution to deformations and stress perturbation will last after the cessation of injection and can represent a triggering factor of the delayed seismic events (Ghassemi et al., 2007). The analysis discussed here is restricted to the stimulation period. Further work will include simulation of the post injection period.

4.5 Conclusion

We have performed thermo-hydro-mechanical models to investigate the effects of cold water injection in a geothermal reservoir. The model considers a fracture zone embedded into a rock matrix. We perform and compare coupled thermo-hydro-mechanical and hydro-mechanical simulations. This approach facilitates understanding the effects of pressure and temperature variations on the mechanisms leading to induced seismicity.

Results show that thermal effects may be critical for geothermal stimulations. Overpressure affects the stress field, especially within the fracture zone, but it does not necessarily lead to unstable conditions. On the other hand, thermal perturbations cause an increase of the deviatoric stress in the cooled portion of the matrix, provoking an unstable condition. Thus, THM coupling describes processes that can play a key role in the triggering of induced seismicity. Furthermore, results show that the greatest thermal effects occur in the rock mass surrounding the fracture zone, which undergoes a significant reduction in stability.

It is worth noting that the overall process is very sensitive to the problem geometry (orientation of the fracture zone), stiffness parameters, stress state regime and confinement conditions. When the greatest confining stress acts normal to the fractures, thermal effects dominate and thermal stress reduction can trigger induced seismic events.

5

Superposition Approach to Understand Triggering Mechanisms of Post-Injection Induced Seismicity *

5.1 Introduction

Fluid injection in deep geological formations is increasingly employed in energy-related technologies, such as geothermal energy production, CO_2 sequestration and wastewater disposal. The seismicity induced by these activities is generally of such small magnitude that cannot be felt at the ground surface (magnitude less than 2). However, it has occasionally reached undesired magnitudes (M > 4) that generate public concern (National Academy of Science, 2012). One of the most critical issues is the occurrence of felt events after the end of injection, especially concerning in Enhanced Geothermal Systems (EGS), such as Soultz-sous-Forêts, France (Baria et al., 2005; Evans et al., 2005) and Basel, Switzerland (Häring et al., 2008; Deichmann and Giardini, 2009; Terakawa et al., 2012). The inability to anticipate and manage these incidents pointed out the incomplete understanding of the processes that trigger post-injection seismicity. Overcoming this limitation remains a key issue for the future successful development of EGS (Parotidis et al., 2004; De Simone et al., 2013; Segall and Lu, 2015).

Seismicity occurs when shear failure conditions are reached along pre-existing or newly created fractures. In the case of injection-induced seismicity, groundwater flow (i.e., often termed pore pressure diffusion by the EGS community) is assumed to be the main triggering mechanism, because frictional resistance reduces with increasing pressure. A number of studies have attempted to relate

*This chapter is based on the paper by De Simone et al. (2017b).

the seismicity cloud with pore pressure diffusion (Shapiro et al., 1999; Shapiro and Patzig, 2003; Dinske, 2011), even for post-injection events (Parotidis et al., 2004). However, these studies do not acknowledge the poroelastic response of the medium, which may not be trivial. Actually, the role of poroelasticity in the triggering of earthquakes has been analyzed by several authors both numerically (Rutqvist et al., 2008, 2013; Vilarrasa et al., 2010; McClure and Horne, 2011; Ghassemi and Zhou, 2011; Jha and Juanes, 2014, among many others) and analytically (Rudnicki, 1999; Rozhko, 2010). They generally conclude that the interactions between fluid flow and solid deformation produce total stress changes that lead to variations of the effective stress field that are different from those of the pressure field.

Numerical simulations of the hydro-mechanical (HM) response to fluid injection often adopt sophisticated geometries and simultaneously account for several processes, e.g., presence of a fracture network, transmissivity increase during injection, non-linear response or shear slip. These representations are realistic, but model complexity hinders conceptual understanding of the underlying processes and does not help in telling apart the specific contribution of each process to the triggering of seismicity. Furthermore, these studies fail to explain the reasons of post-injection seismicity. Recently, Segall and Lu (2015) used the analytical solutions of Rudnicki (1986) to show that poroelasticity may be the reason of after shut-in seismicity. They assumed a spherical pressure distribution corresponding to a point injection into a homogeneous medium, which is conceptually appropriate, but hardly representative of typical EGS in crystalline reservoirs. These reservoirs are often intersected by numerous fractures belonging to a few sets of orientations and some dominant fault zones, which concentrate fractures with the same orientation (Baria et al., 1999; Genter et al., 2000; Jung, 2013). Injection is usually performed in the proximity of fault zones that are several orders of magnitude more permeable than the surrounding rock matrix and constitute preferential flow paths (Häring et al., 2008; Evans et al., 2005). The pore pressure distribution in such media is very different from spherical and more realistic settings should be investigated.

Hydraulic effects are not the only process involved in induced seismicity. Thermoelasticity may also play a decisive role when the injected fluid is significantly cooler than the hot reservoir and large volumes of fluid are injected, which is the case of EGS or well stimulation. The temperature contrast causes thermal stresses

that may affect mechanical stability (Majer et al., 2007; Ghassemi, 2012; Jeanne et al., 2014a). To study the impact of thermal effects, some authors performed coupled thermo-hydro-mechanical simulations (Kohl et al., 1995; Ghassemi et al., 2007, 2008; Ghassemi and Zhou, 2011; McDermott et al., 2006; Koh et al., 2011; De Simone et al., 2013; Vilarrasa, 2016; Pandey et al., 2017). However, distinguishing the contribution of thermal effects from the other processes is not straightforward.

Shear slip stress transfer may be a third relevant factor. The activation of frictional sliding, which is specifically sought during well stimulation, releases the shear stress on the slipping surface, in the form of microseismic episodes. Frictional sliding improves the local stability, but affects the nearby stress field, thus causing instability and seismic events elsewhere. This concept is extensively used to explain aftershock sequences in natural seismology (e.g., King et al., 1994; Freed, 2005). In recent years, this approach has also been reconsidered as an attempt to explain induced seismicity (Schoenball et al., 2012; Catalli et al., 2013), but has shown that even though static stress transfer is an important process in the occurrence of injection-induced seismicity, it is not the exclusive one.

It is clear that hydraulic, thermal and shear slip stress transfer effects are the main physical processes that induce seismicity. Yet, while they are well understood, post-injection seismicity is not. We conjecture that the key to understanding lies in the superposition of these three processes, whose effects and characteristic times are quite different.

The objective of this work is precisely to analyze the relative importance of each of these three processes separately, and in combination, on the triggering of seismicity during and after injection, so as to help in the identification of the mechanisms that may trigger seismicity in the post-injection period. To this end, we consider the simple, yet realistic, case of a stiff low conductivity reservoir intersected by a soft high conductivity fault zone.

5.2 Methods

5.2.1 Governing equations

The perturbation induced by pressure and temperature variations and shear slip activation are expressed analytically using linear poro-thermoelasticity equi-

librium (McTigue, 1986), which, in the absence of body forces and in terms of variations with respect to an initial equilibrium state, in heterogeneous media can be derived as

$$\nabla\cdot(G\nabla\mathbf{u})+\nabla\cdot\left[G\left(\nabla\mathbf{u}\right)^{T}+\lambda\left(\nabla\cdot\mathbf{u}\right)\mathbf{I}\right]=-\nabla\left(\alpha P\right)-\nabla\left[\alpha_{T}\left(2G+3\lambda\right)T\right], \quad (5.1)$$

where $\mathbf{u}$ is the displacements vector, $G = E/[2(1+\nu)]$ and $\lambda = E\nu/[(1+\nu)(1-2\nu)]$ are the shear and Lamé moduli, respectively, E is Young's modulus, ν is Poisson ratio, P is fluid pressure, α is the Biot-Willis' coefficient, α_T is the linear thermal expansion coefficient and T is temperature. We adopt the sign convention of geomechanics in which compressive strain and stresses are positive, so that the effective stress tensor $\boldsymbol{\sigma}'$ is $\boldsymbol{\sigma} - \alpha P\mathbf{I}$, where $\boldsymbol{\sigma}$ is the total stress tensor and $\mathbf{I}$ is the identity matrix.

Equation (5.1) makes it clear that the three processes, (i.e., shear slip activation, hydro-mechanical coupling, and thermo-mechanical coupling) superimpose linearly. Therefore, they can be analyzed individually and their contribution to the variation of the stress field can be superimposed. The gradients of pressure and temperature act like body forces and provoke analogous perturbation of the total stress field (Biot, 1956b; McTigue, 1986; Norris, 1992; Segall and Fitzgerald, 1998; Rudnicki, 1999; Zimmerman, 2000), although their respective time scales can be dramatically different (Ghassemi et al., 2007). These perturbations can be expressed by

$$\boldsymbol{\sigma}^{HM}(\mathbf{x}) = \boldsymbol{\sigma}_{D}^{HM}(\mathbf{x})P_{c} \quad (5.2)$$

and

$$\boldsymbol{\sigma}^{TM}(\mathbf{x}) = \boldsymbol{\sigma}_{D}^{TM}(\mathbf{x})(2G+3\lambda)\alpha_{T}T_{c} \quad , \quad (5.3)$$

where the subscript c stands for characteristic variables and the subscript D denotes a dimensionless variable (the variable divided by its characteristic value). Thus, $\boldsymbol{\sigma}_D^{HM}$ and $\boldsymbol{\sigma}_D^{TM}$ are the dimensionless HM and TM stresses, which depend on geometry and spatial variability, but not on temperature, injection rate or overall (characteristic) mechanical parameters. Fluid flow is governed by

$$\left(\phi\beta+\frac{1-\phi}{K_{s}}\right)\frac{\partial P}{\partial t}+\frac{\partial}{\partial t}\left(\nabla\cdot\mathbf{u}\right)=\nabla\cdot\left(\frac{k}{\mu}\nabla P\right) \quad , \quad (5.4)$$

where k is intrinsic permeability, μ is fluid viscosity, ϕ is porosity, β is fluid compressibility and K_s is compressibility of the solid grains. This equation is usually written by assuming that the volumetric deformation is proportional to P (i.e., $\nabla \cdot \mathbf{u} = P/K$, where $K = E/[3(1-2\nu)]$ is bulk modulus). While this assumption is a simplification (De Simone and Carrera, 2017), we will keep it to facilitate writing fluid flow equation in dimensionless form (e.g., Bear and Bachmat, 2012)

$$S_{s_D} \frac{\partial P_D}{\partial t_{DH}} = \frac{t_{cH}}{L_{cH}^2} \frac{k_c}{\mu S_{s_c}} \nabla_D \cdot (k_D \nabla_D P_D) \quad , \tag{5.5}$$

where t_{cH} and L_{cH} are the characteristic time and length of the hydraulic problem, respectively. They are chosen so that the coefficient in the right hand side of Eq. (5.5) equals one (i.e., $t_{cH} = \mu S_{s_c} L_{cH}^2 / k_c$). The dimensionless k_D and S_{s_D} are relative to reference values, i.e, $k_D(\mathbf{x}) = k(\mathbf{x})/k_c$ and $S_{s_D}(\mathbf{x}) = S_s(\mathbf{x})/S_{s_c}$, where $S_s(\mathbf{x}) = \phi\beta + (1-\phi)/K_s + 1/K$. The characteristic pressure is taken from the injection boundary condition ($P_c = \mu Q/k_c$, where Q is the volumetric flow rate per unit length).

Heat transport is expressed in dimensionless form as (e.g., Bear and Bachmat, 2012)

$$\frac{\partial T_D}{\partial t_{DT}} = \frac{\zeta}{C} \frac{t_{cT}}{L_{cT}^2} \nabla_D^2 T_D - \frac{q C_w}{C} \frac{t_{cT}}{L_{cT}} \nabla_D T_D \quad , \tag{5.6}$$

where C and C_w are the total and fluid heat capacity, ζ is the thermal conductivity including dispersion, q is the fluid specific flux, t_{cT} and L_{cT} are the characteristic time and length of the thermal problem, respectively. Note that, contrary to flow, there are two options to set the characteristic times and distances. If advection dominates, which may occur along fractures close to the injection well, $L_{cT} = qC_w t_{cT}/C$, that is, the affected region grows linearly with time. When conduction and dispersion dominate, which will occur after injection stops and in sparsely fractured regions, $L_{cT} = \sqrt{\zeta t_{cT}/C}$.

In the case of EGS, the area affected by fluid overpressure is generally much greater than the cooled zone at any given time (Ghassemi, 2012). In fact, using typical values for the characteristic variables above, the pressure propagation distance is in the order of $10^{-2}\sqrt{t}$ (m, with t expressed in s) in granitic rocks, whereas the thermal propagation, governed by conduction due to the low permeability of

granite, is in the order of $10^{-3}\sqrt{t}$ (Jaeger et al., 2007).

The variation of the displacement field in response to the activation of shear slip is expressed by Equation (5.1) solely for the mechanical problem, i.e., right hand side of Eq. (5.1) equals zero, which in dimensionless form for a homogeneous medium is

$$(1-2\nu)\,\nabla_D^2\mathbf{u}_D + \nabla_D\,(\nabla_D\cdot\mathbf{u}_D) = 0 \quad , \tag{5.7}$$

where $\mathbf{x}_D = \mathbf{x}/L$ is the dimensionless distance from the epicenter, L is the length of the slipping surface, $\mathbf{u}_D = \mathbf{u}/u_c$, u_c is the peak shear slip and the characteristic stress is $\sigma_c = u_c G/L$, where G refers to the matrix.

The overall stress variation results from superposition of the stresses associated to the three processes,

$$\boldsymbol{\sigma}(\mathbf{x}) = \boldsymbol{\sigma}_D^{HM}(\mathbf{x})\frac{Q}{k/\mu} + \boldsymbol{\sigma}_D^{TM}(\mathbf{x})(2G+3\lambda)\alpha_T T_c + \boldsymbol{\sigma}_D^{SLIP}(\mathbf{x})\frac{u_c G}{L} \quad . \tag{5.8}$$

The resulting stress field can be used to evaluate if shear failure conditions are reached along a plane, by means of the Coulomb Failure Stress (CFS). According to the Mohr-Coulomb criterion, shear failure occurs if (Jaeger et al., 2007)

$$CFS = |\tau| - (c + \psi\cdot\sigma_n') > 0 \quad , \tag{5.9}$$

where τ is shear stress, c is cohesion, σ_n' is normal effective stress and ψ is the friction coefficient. A positive variation of CFS ($\Delta CFS > 0$) means approaching failure (Harris, 1998).

5.2.2 Numerical simulations

Our study is inspired in some notorious examples of hydraulic stimulation at EGS sites, like the ones at Basel and Soultz (Evans et al., 2005; Häring et al., 2008). We assume a simple but realistic conceptual model typical of EGS consisting of a sub-vertical 1 m thick fault zone embedded in a stiff rock matrix. Cold water is injected through a vertical well that intersects the fault zone, provoking the activation of shear slip along fractures placed within the fault zone. Therefore, it is sufficient to adopt a two-dimensional plane strain domain, which represents

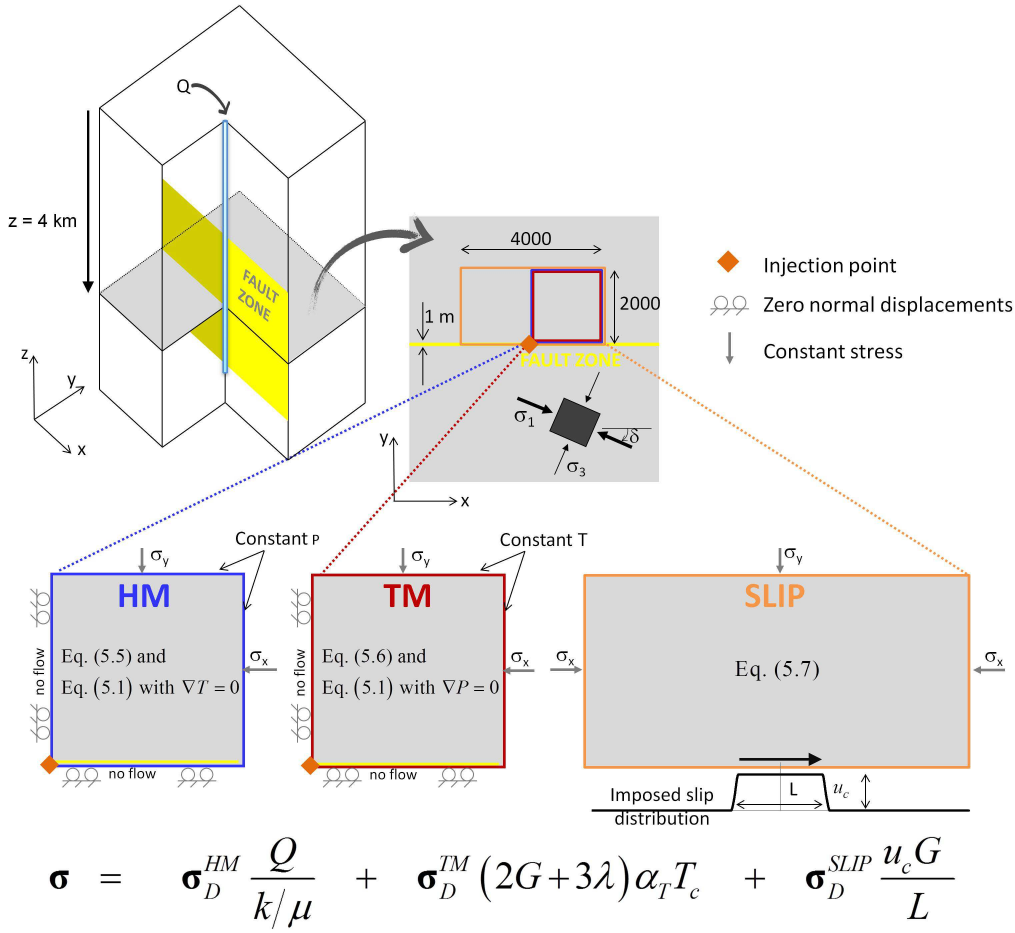

$$\boldsymbol{\sigma} = \boldsymbol{\sigma}_D^{HM}\frac{Q}{k/\mu} + \boldsymbol{\sigma}_D^{TM}\left(2G+3\lambda\right)\alpha_T T_c + \boldsymbol{\sigma}_D^{SLIP}\frac{u_c G}{L}$$

Figure 5.1: Conceptual (upper) and working (lower) geometries used for the evaluation of the hydro-mechanical, thermo-mechanical and shear slip effects. The equations governing each one of the processes and their corresponding perturbations of the stress field are also shown.

a horizontal section placed at 4 km depth in the tridimensional conceptual model (Fig. 5.1). The domain dimensions have been adjusted to avoid boundary effects.

We analyze the three processes separately by means of numerical simulations using the fully coupled numerical code CODE_BRIGHT (Olivella et al., 1994, 1996). We adopt linear elasticity to facilitate superposition of the processes. Both the fault zone and the matrix are isotropic. The fault zone, which represents an intensely fractured and altered region within a granitic fractured rock mass, is much more conductive and softer than the matrix. We present the formulation in dimensionless form, but actual computations are dimensional, using

the parameters of Table 5.1. The material properties are consistent with values at EGS sites (Genter et al., 2009; Evans et al., 2012). To isolate thermal effects we neglect the dependence of fluid density and viscosity on temperature. Initial pressure, temperature and stress state have been evaluated with respect to the considered depth (Table 5.1 and Fig. 5.1). We assume a strike slip stress regime, i.e., the vertical stress σ_v is the intermediate principal stress, so that failure entails horizontal slip along sub-vertical fractures (Anderson, 1951). The fractures within the fault zone are close to be optimally oriented for shear failure, which is reasonable because the existence of a conductive fault zone is often related to

Table 5.1: Material properties, initial and boundary conditions.

Material properties	**Fault zone**	**Matrix**
k, Intrinsic permeability (m^2)	10^{-12}	10^{-17}
μ, fluid viscosity (MPa s)	$1.5x10^{-10}$	
E, Young's modulus (MPa)	100	30000
ϕ, Porosity (-)	0.1	0.05
ν, Poisson ratio (-)	0.3	
α, Biot coefficient (-)	1	
c_s, Specific heat for solid (J/kg/°K)	800	
λ, Thermal conductivity (Wm/°K)	2.5	
α_T, Linear thermal expansion coefficient (1/°K)	$1x10^{-5}$	
c, Cohesion of pre-existing fractures (MPa)	0	
ψ, Friction coefficient of pre-existing fractures (-)	0.577	
Initial conditions		
P_0, Pressure (MPa)	40	
T_0, Temperature (°C)	150	
σ_1, Maximum principal stress (MPa)	130	
σ_3, Minimum principal stress (MPa)	70	
σ_x (MPa)	110	
σ_y (MPa)	90	
σ_z (MPa)	100	
τ_{xy} (MPa)	28	
δ, Stress tensor orientation (°)	∼35	
CFS on the x-direction (MPa)	-0.87	
CFS on the y-direction (MPa)	-12.41	
Boundary conditions		
Q, Injection rate (L/s/m)	0.150	
T_{inj}, Injection temperature (°C)	60	
u_c , peak shear slip (m)	0.30	
L, length of slipping surface (m)	1000	

a favorable current stress regime, and it is consistent with observations at EGS sites (e.g., Häring et al., 2008). Note also that we consider the in-situ stress regime to be close to failure, which is also characteristic of the crystalline basement (Zoback et al., 2002). Nonetheless, as stated above, most of the analysis below is performed in terms of variation of the stress field, i.e., regardless of the initial in-situ conditions, which are relevant only for failure analysis. Therefore, most of the results can be normalized with respect to parameters and inputs, adopting the equations of Section 5.2.1.

We simulate 7 days of injection and 40 days of recovery, which is similar to EGS stimulation operations. To analyze the effects of the activation of shear slip along a pre-existing fault within the fault zone, we impose the cumulative slip distribution shown in Figure 5.1. It represents the superposition of several irreversible slips occurred during injection. Given the linearity of the problem, the cumulative effects of several slips are equal to the effect of the cumulative slip. The relative displacement is a right-lateral strike-slip (Mode II) in direction x, which is consistent with the adopted stress regime. Because of antisymmetry, we only need to apply it as a boundary condition on the lower boundary of the matrix domain (Fig. 5.1). To isolate the effect of static stress transfer from other effects, we disregard the pressure variation inside the fault caused by frictional sliding (Rice and Cleary, 1976; Rudnicki, 1987; Wang, 1997) and the thermal fluid pressurization due to frictional heating during slip (Sibson, 1973; Andrews, 2002; Rice and Dunham, 2009).

5.3 Results

5.3.1 Hydro-mechanical effects

Hydro-mechanical (HM) coupling is the dominant process during the injection phase. The increase in pore pressure reduces the frictional resistance to slip, inducing microseismicity. Overpressure affects most of the fault zone, but only a small region within the low-permeability matrix (Fig. 5.2a). The behavior is similar to that of a thin aquifer, with thickness much smaller than its lateral extent, between impervious layers (Verruijt, 1969; Hsieh and Cooley, 1995; Hsieh, 1996). In this setting, the pressurized region tends to expand laterally (i.e., in the direction of the fault zone, x-direction), but displacement continuity with the surrounding matrix, which is not pressurized and thus does not expand, hinders

this expansion by means of increasing shear stress. This restraint to deformation generates total compressive stresses in the lateral direction ($\Delta\sigma_x$), which are proportional to the stiffness of the surrounding matrix (Rudnicki, 1999). On the other hand, the pressurized region expands without any deformation constraint in the direction normal to the fault (y-direction) and, therefore, the corresponding total stresses (σ_y) barely change. As a result, we observe a large increase of total stress in the direction of the fault zone, $\Delta\sigma_x$ (Fig. 5.2b), but only a small increase in the perpendicular direction, $\Delta\sigma_y$ (Fig. 5.2c).

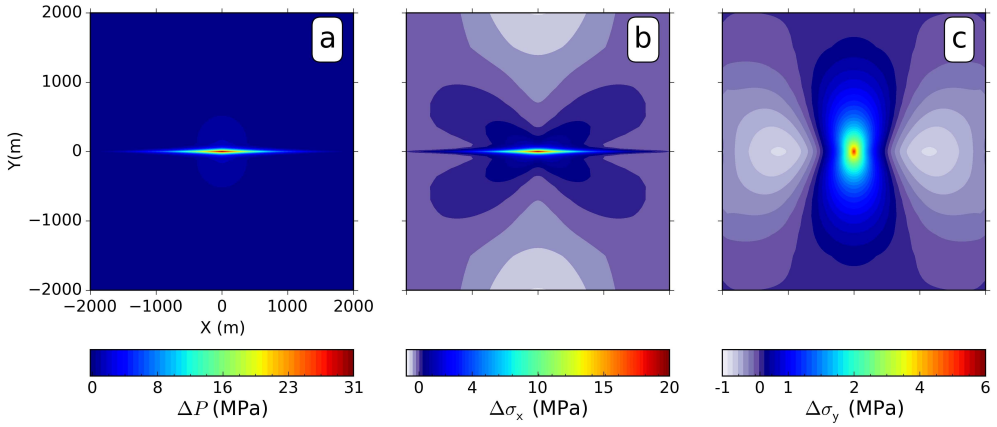

Figure 5.2: Variation of (a) pressure and total stresses in the (b) x- and (c) y-directions after 7 days of injection for the HM problem.

These results make it clear that the effective stress tensor reduction is not isotropic along the fault zone (Fig. 5.3). In particular, the σ'_y variation is greater than the σ'_x variation, which entails an increase of the deviatoric stress (and, therefore, of shear stresses) for our initial stress tensor. Note also that the total stress variation around the injection well is transferred to the whole domain, much like the application of an external load, and thus, acting instantaneously (observe Fig. 5.2). That is, stress propagates further away than the pressurized region, where it causes a non-negligible increase of not only effective stresses, but also of fluid pressure, which is proportional to the Skempton coefficient (Skempton, 1954; Rice and Cleary, 1976).

A consequence of these stress changes is that the normal effective stress and the shear stress on a fracture decrease or increase depending on the fracture location and orientation. Therefore, shear failure may be induced in some fractures during injection, but hindered (or delayed) in others. For example, fractures oriented like the fault zone and placed within the portion of the fault zone affected

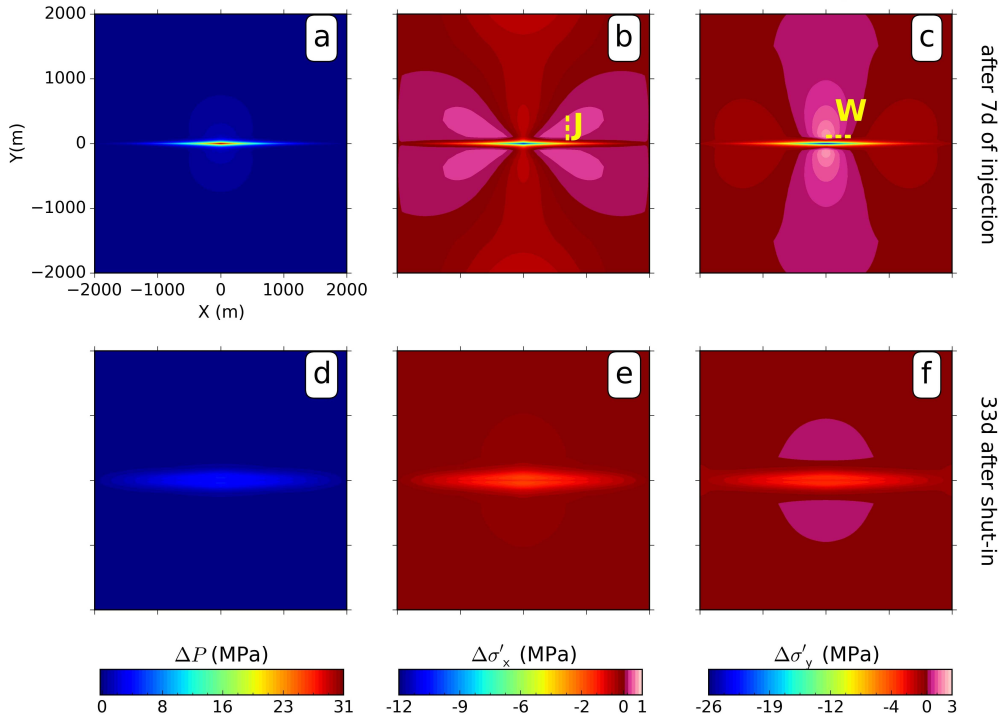

Figure 5.3: Variation of (a) pressure and effective stresses in the (b) x- and (c) y-directions after 7 days of injection and variation of (d) pressure and effective stresses in the (e) x- and (f) y-directions at 33 days after the shut-in for the HM problem.

by overpressure experience a large reduction in normal effective stress (observe $\Delta\sigma'_y$ in Fig. 5.3c). Thus, stability along the fault zone worsens during injection, which may activate a number of earthquakes. On the other hand, some regions of the matrix are affected by a slight increase in effective stresses during injection, so their stability improves. In the region labeled as "J" (Fig. 5.3b) this small increase of σ'_x improves the stability of fractures oriented parallel to the y-axis. Similarly, in the region "W" (Fig. 5.3c), the increase in σ'_y improves the stability of potential fractures oriented parallel to the x-axis. Overpressure decays rapidly once injection stops (Fig. 5.3d-5.3f) but partly diffuses away, which together with the removal of the poromechanical load (sudden decrease of pressure gradients) leads to a sudden drop in the stability of fractures in the regions W and J.

Figure 5.4a and 5.4b display the temporal evolution of the normal effective stress and shear stress at two points representing fractures within W and J. During injection, the normal effective stress acting on both regions increases initially because of the increase in the total stress perpendicular to the fractures. Moreover,

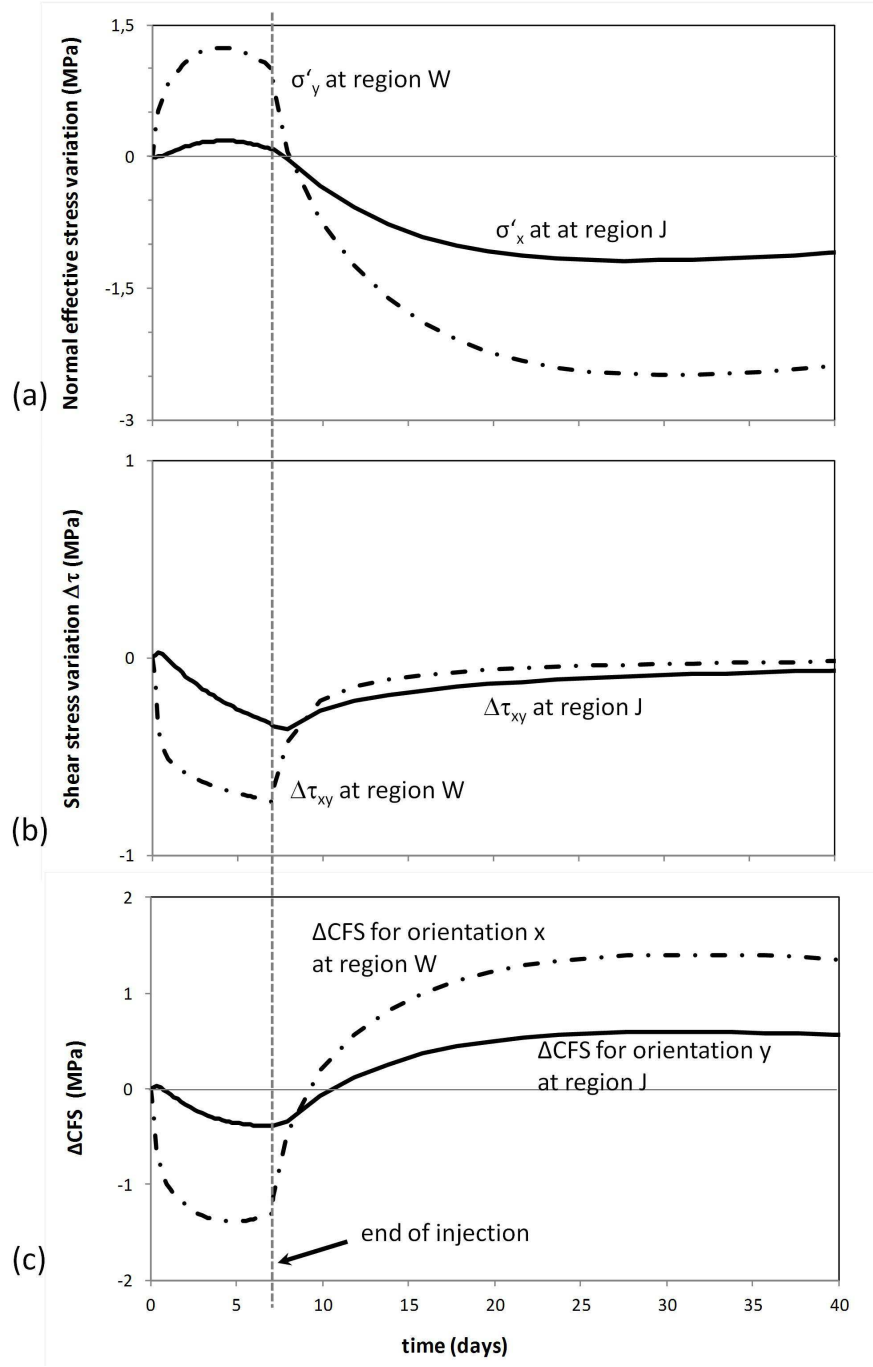

Figure 5.4: Temporal evolution of the variation of (a) normal effective stress, (b) shear stress and (c) failure conditions for vertical fractures placed in region J (x=700, y= 70) and horizontal fractures in region W (x=100, y=100).

the shear stress along these fractures decreases, which further enhances stability. Eventually, the normal effective stress and safety start to decrease slowly as overpressure reaches these points. However, the situation changes rapidly once injection stops because pressure gradients close to the well dissipate much faster than local pressures. Pressure gradients close to the well act as a compressive loading and provoke stabilization during injection in these regions, whereas the residual fluid overpressure causes destabilization by reducing effective stresses. As a result, the decrease in normal effective stresses after shut-in is faster than during the injection period because the stabilization effect vanishes, which may induce post-injection seismicity, as shown by the positive ΔCFS that approaches failure conditions both in region W and J (Fig. 5.4c). It is clear that the decrease in stability in these regions would be lessen by a slow reduction, as opposed to a sudden stop, in injection rate.

5.3.2 Thermo-mechanical effects

The thermo-mechanical (TM) coupling cannot be isolated from the hydraulic problem because heat advection is driven by fluid flow. Therefore, we simulate the THM coupling and then subtract the HM coupling results. This operation enables us to separate thermal from hydraulic effects without forgoing the actual temperature distribution (Fig. 5.5a), which is the result of both dispersion-conduction and advection processes. In fact, heat transport in fractures is significantly governed by advection (Kohl et al., 1995), thus temperature variation propagates mainly along the fault zone, but also diffuses slightly into the matrix by conduction. Furthermore, heat transport is generally much slower than pressure diffusion (Ghassemi, 2012). Therefore, TM effects affect a smaller portion of the domain than HM effects (compare Figs. 5.3 and 5.5).

As the temperature distribution shape is qualitatively similar to that of overpressure (compare Figs. 5.2a and 5.5a), the responses are also similar in terms of total stresses. Similar to poroelastic stresses, thermal stresses arise only when displacements are somehow restrained. Thermal strains occur mostly in the direction normal to the fault zone, whereas they are highly restrained in the direction parallel to the fault. This strain distribution means that total stress parallel to the fault changes significantly more than total stress normal to fault. However, contrary to the stresses induced by overpressure, cooling provokes contraction of the rock that induces the same reduction of total and effective stresses, as we have

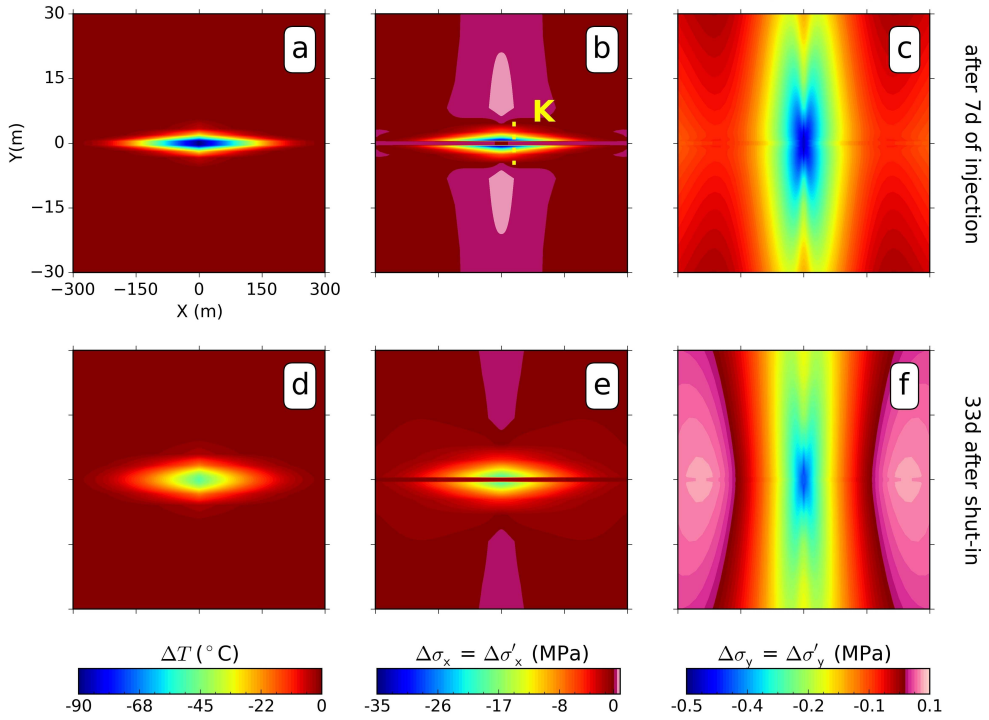

Figure 5.5: Variation of (a) temperature and thermally driven effective stresses in the (b) x- and (c) y-directions after 7 days of injection and variation of (d) temperature and thermally driven effective stresses in the (e) x- and (f) y-directions at 33 days after the shut-in. Note that the region affected by cooling is one order of magnitude smaller than that affected by overpressure.

neglected pressure variations due to thermal effects. Therefore, the σ'_x decrease is greater than the σ'_y decrease (Fig. 5.5). As thermal stresses are proportional to rock stiffness (Eq. (5.3)), large thermal stresses arise in the portion of the matrix affected by temperature drop, but they are small inside the fault zone, which is much softer than the matrix.

The reduction of compressive stress σ'_x is very large around the fault zone, which means that frictional sliding may be activated in the vicinity of the well along fractures parallel to the y-axis (region K in Fig. 5.5b). If the initial stress σ'_x is small, it may be reduced to zero or even become tensile, especially if the effects of overpressure are superimposed. As a result of a tensile stress, cracks would be generated in the y-direction. However, this is not the case in our study because the initial σ'_x is quite large.

When injection stops, the advection contribution to heat transport vanishes,

so cooling proceeds solely by conduction. Given its slowness, the temperature drop and the thermal stress perturbation remain virtually unchanged for long time after shut-in (Fig. 5.5d - 5.5f). This post-injection behavior contrasts with that of overpressure, which dissipates rapidly after shut-in (Fig. 5.3).

5.3.3 Shear slip stress transfer

Activation of slip movements along the fault zone provokes a reduction of shear stress around the slipped surface (stress drop) and anti-symmetric variations of both the stresses perpendicular and parallel to the fault at the tips of the slipped surface (Fig. 5.6). The magnitude of the stress perturbations depends on the slip characteristics (Eq. (5.8)). Similarly to the response to pressure and temperature alterations, the variation of the stress field does not depend on the in-situ initial stress field, although the occurrence of slip does.

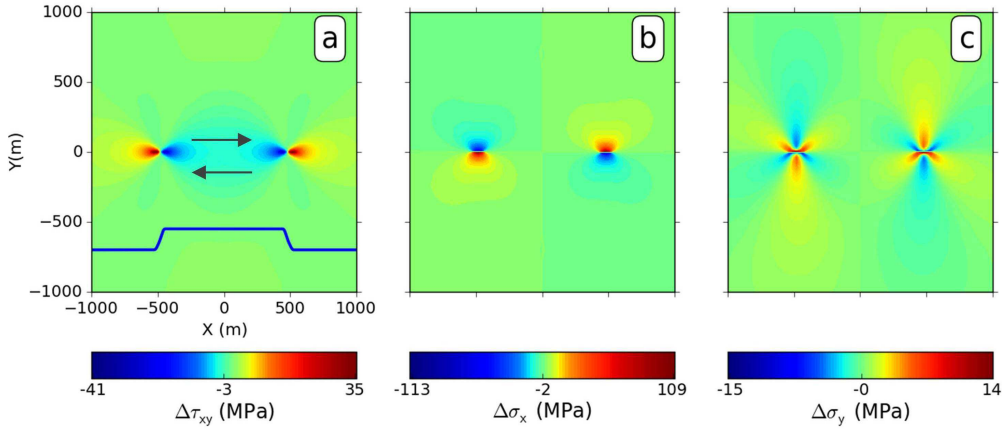

Figure 5.6: Variation of (a) shear and compressive (b) x- and (c) y-stress fields driven by shear slip. The blue line inside (a) represents the spatial distribution of the imposed slip, with the orientation indicated by the grey arrows.

The variation of the stress field produces a rotation of the stress tensor (Fig. 5.7b). Contrary to the variation of the stress field, this rotation does depend on the initial stress state. Specifically, it depends on the ratio of the shear stress variation to the initial in-situ shear stress (King et al., 1994). Therefore, the smaller the initial stresses, the greater the rotation for a given shear stress variation. In our case, the resulting rotation is significant, especially around the tips (Fig. 5.7b), even though the initial stresses are high (Table 5.1). Stress tensor rotation modifies stability conditions. In particular, where the tensor rotation is

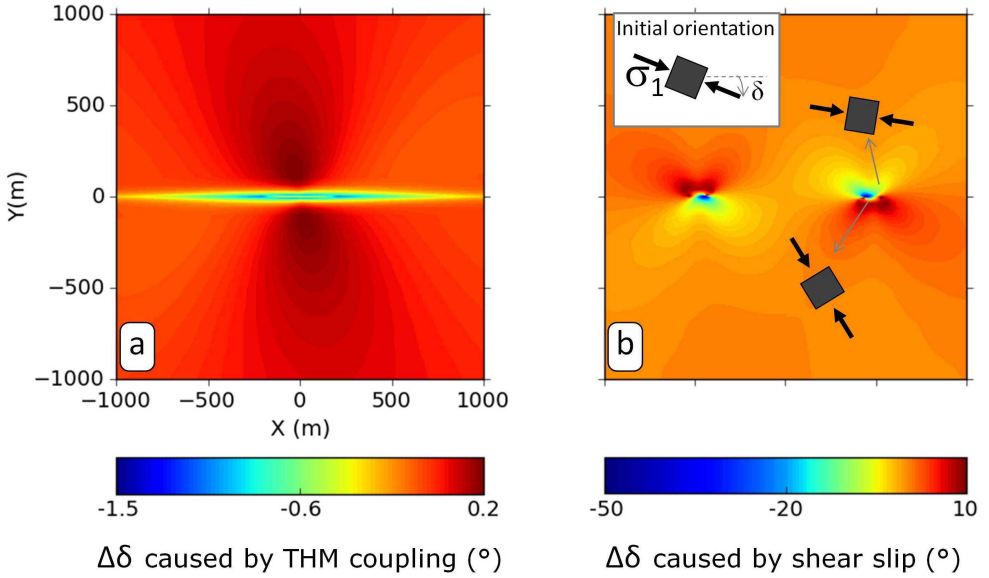

Figure 5.7: Stress field rotation caused (a) by THM coupling after 7 days of injection and (b) by the slip movement. The regional and the perturbed tensor orientation are also shown. Note that we assume the convention of positive clockwise angle and rotation.

positive, a fault oriented like the y-axis becomes closer to failure than before the slip. This perturbation of the stress field is permanent because slip is irreversible.

5.3.4 Superposition of mechanical responses to overpressure, cooling and slip

The superposition of the three effects is analyzed in terms of failure condition (CFS) and its variation (ΔCFS). The CFS depends on the initial stress state, which usually entails some uncertainty. The ΔCFS, conversely, does not depend on the initial conditions, but only on the variation of the stress tensor, which can be normalized with respect to the assumed parameters and the perturbations affecting the system, according to Eq. (5.8).

Figure 5.8 displays ΔCFS due to the combined effect of pressure and temperature variation (i.e., the superposition of the HM and TM couplings) after 7 days of injection and 33 days after shut-in for fractures oriented along the x- and y-directions. Stability is highly worsened during injection in a narrow region around the fault zone, especially for fractures oriented in the x-direction. This reduction in stability is largely controlled by the increase in pressure and, indeed,

its pattern is similar to that of pressure. Thermal effects are limited to the very proximity of the well (region K) and highly decrease stability of fractures oriented in the y-direction. Note that the maximum ΔCFS in the y-orientation (fractures perpendicular to the fault) is greater than that in the x-orientation because of the TM coupling. These positive values of ΔCFS persist in the post-injection period. They are somewhat attenuated, but spread away from the injection well.

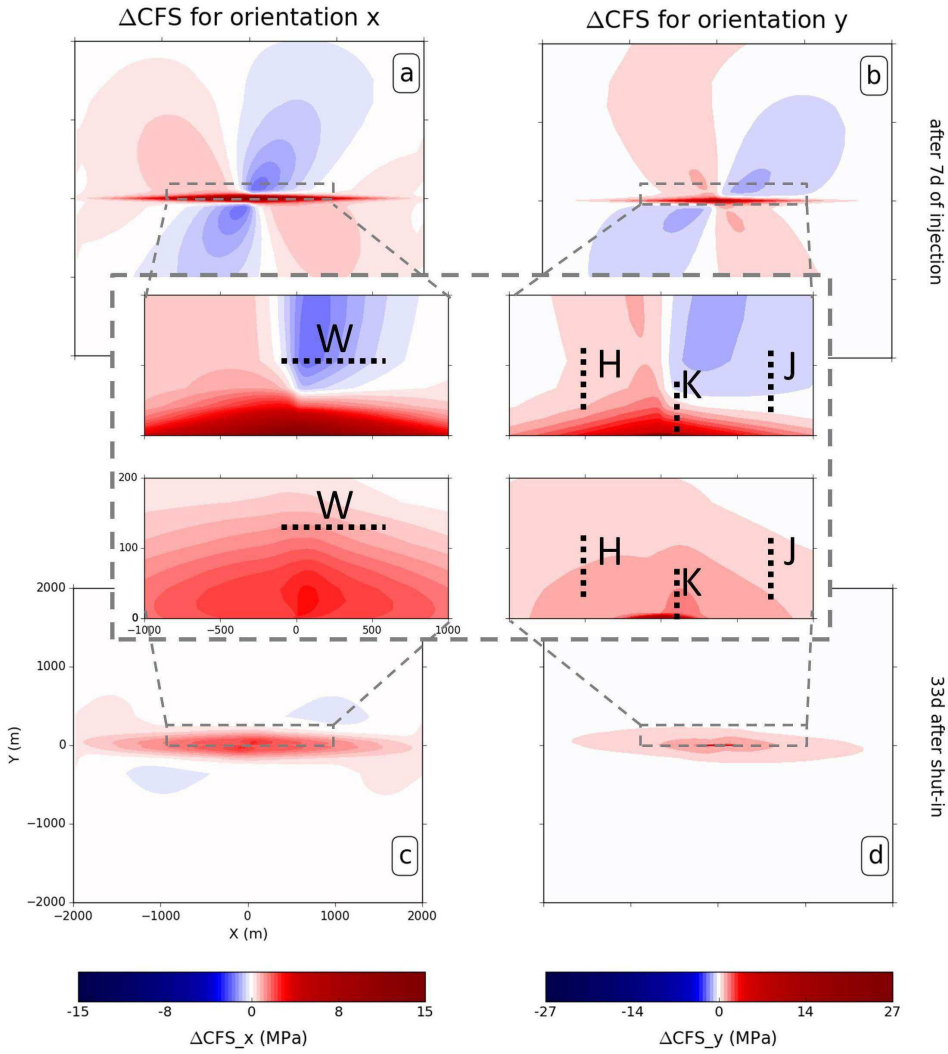

Figure 5.8: Variation of CFS (ΔCFS) due to the sum of hydraulic and thermal effects in the (a) x- and (b) y-direction after 7 days of injection and in the (c) x- and (d) y-direction at 33 days after the shut-in. The close-ups focus on the observation regions W, H, J and K. The dashed black lines indicate fractures whose stability is analyzed in detail.

Moreover, there are four anti-symmetric lobes of positive and negative ΔCFS during injection, which are placed far away from the main area of influence of overpressure. These lobes are generated by the poroelastic behavior described in Section 5.3.1, especially by the non-isotropic increase in effective stresses, which generates anti-symmetric variation of the shear stress in the four quadrants. Therefore, potential fractures placed in the observation regions W and J (marked with black dashed lines in the close-ups of Fig. 5.8) are stabilized during injection, whereas fractures in the region H undergo a decrease in stability. These lobes disappear in the post-injection period (Figs. 5.8c and 5.8d) because the removal of the hydraulic gradient load, together with the propagation of overpressure, results in the reduction in stability of the previously stabilized W and J-fractures in the post-injection period. The fractures that experience a decrease in stability during injection, like H-fractures, remain less stable than initially after injection stops. The change in stability is abrupt, because so is the reduction in flow rate and hydraulic gradients, as shown by the temporal evolution of ΔCFS along the observation fractures (Fig. 5.4c).

Figure 5.9 displays the CFS values, which indicate whether shear failure is actually reached in the regions where positive ΔCFS values have been observed in Fig. 5.8. The CFS for fractures oriented in the x-direction, which is close to the critical direction for failure according to the initial stress state, is very similar to the ΔCFS (compare Fig. 5.8a with Fig. 5.9a and Fig. 5.8c with Fig. 5.9c). Therefore, failure conditions are extensively reached along the fault zone at the end of injection, in agreement with the induced seismicity observed during injection tests (Evans et al., 2005; Deichmann et al., 2014). In the post-injection period, the seismicity cloud migrates away coinciding with the pressure perturbation front (see the evolution of positive CFS values in Figs. 5.9a and 5.9c).

Regarding the fractures that experience stability reduction only after shut-in, i.e., $\Delta CFS > 0$, Figure 5.9 shows that W-fractures do really fail in the post-injection period. On the contrary, J-fractures are initially far from failure condition and ΔCFS is not sufficient to reach failure. Thus, poromechanical response of porous media to fluid injection can explain post-injection seismicity in specific sets of fractures.

Figure 5.10 displays CFS resulting from the superposition of overpressure, cooling and shear slip effects. The slip stress transfer results in a significant and

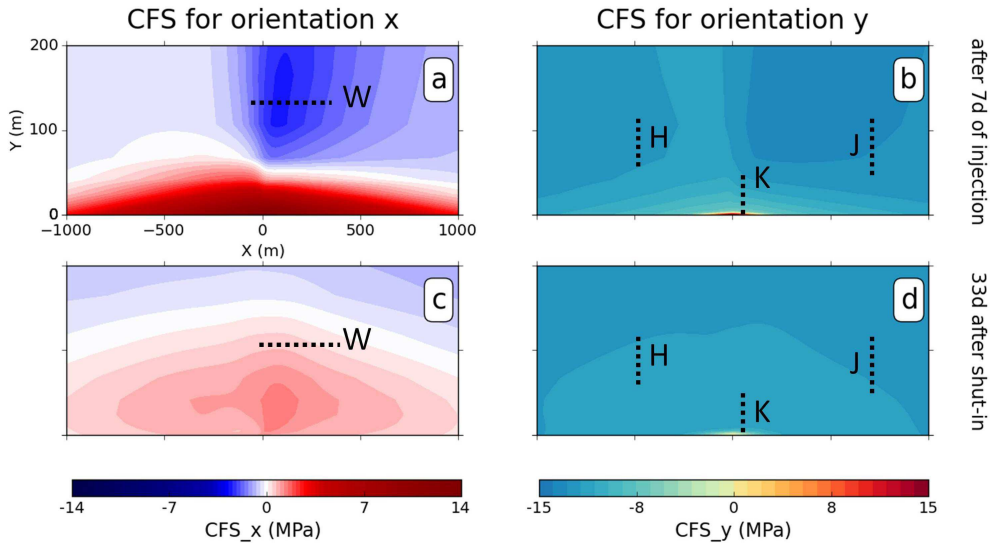

Figure 5.9: *CFS* for the (a) x- and (b) y-directions due to the superposition of hydraulic and thermal effects after 7 days of injection and for the (c) x- and (d) y-directions at 33 days after shut-in. Note that the colormap for y-direction is different than for x-direction in order to better display the results. The dashed lines indicate fractures whose stability is analyzed in detail.

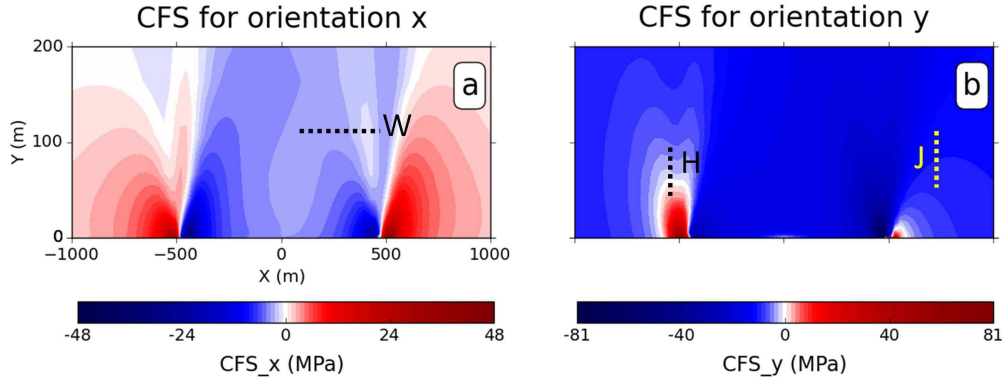

Figure 5.10: *CFS* due to the superposition of hydraulic, thermal and slip movement effects 33 days after shut-in in the (a) x- and (b) y-directions. The dashed lines indicate fractures whose stability is analyzed in detail.

permanent variation of the stress field, which modifies the proximity to shear failure conditions. Stress concentration at the tips highly promotes failure along fractures parallel to the x-axis at the edges of the slipped surface (Fig. 5.10a). In contrast, the shear stress released around the slipped surface highly stabilizes the W-fractures. Perturbation of the stress field also affects the stability of the

faults oriented like the y-axis (Fig. 5.10b). In the zone of extension (Fig. 5.6), where the tensor rotation is positive (Fig. 5.7), H-fractures come closer to shear failure than before the slip movement. In the zone of compression (Fig. 5.6), the effects on the J-fractures, is not very relevant. Still, stability on other orientations should be investigated (Fig. 5.11).

Figure 5.11 displays the CFS value as a function of fracture orientation, both at the end of injection and 33 days into the post-injection period. We distinguish between results for only THM coupling and the ones due to the superposition of THM coupling and slip effects. In the compressional zone (J-region), the CFS due to THM coupling (grey lines in Fig. 5.11a) indicates that failure conditions are not reached for any orientation at the end of the injection ($CFS < 0$). However, failure occurs ($CFS > 0$) in the post-injection period for fractures oriented in the ranges from -5° to 10° with respect to the x-axis, and their conjugate at 60°-70° (see purple shadows in Fig. 5.11a). The activation of shear slip (black lines) introduces a further destabilization (CFS increases) that significantly increases the range of yielding orientations. The CFS resulting from the superposition of the three processes is positive both at the end of injection and in the post-injection period for fractures with orientation in the ranges from -10° to 17° and 52°-78° with respect to the x-axis. Shut-in and the resulting loss of the compressive effect in this region (recall discussion of Figure 5.4) cause further destabilization (increase of CFS) for all orientations. In particular, fractures around orientations -10°, 17°, 50° and 80° with respect to the x-axis (marked with red shadows in Fig. 5.11a) are stable (negative CFS) during injection, but become unstable in the post-injection period. That is, thermal and slip effects tend to cause failure in this region, but the stabilizing effect of pressure gradients keeps them static. It is only when these pressure gradients dissipate that those fractures fail.

In the extensional zone (H region), failure caused by THM coupling occurs during injection for a range of orientations that increases slightly in the post-injection period (grey lines in Fig. 5.11b). The activation of slip further increases the range of failing fractures. Moreover, it provokes a rotation of the stress tensor (recall Fig. 5.7) that shifts the peaks of the curves, which represent the orientation of the most critically stressed fractures. As a result, failure may occur along orientations much different from the ones that were initially critically oriented. Note also that failure occurs only after shut-in for some specific orientations (marked with red shadows in Fig. 5.11b).

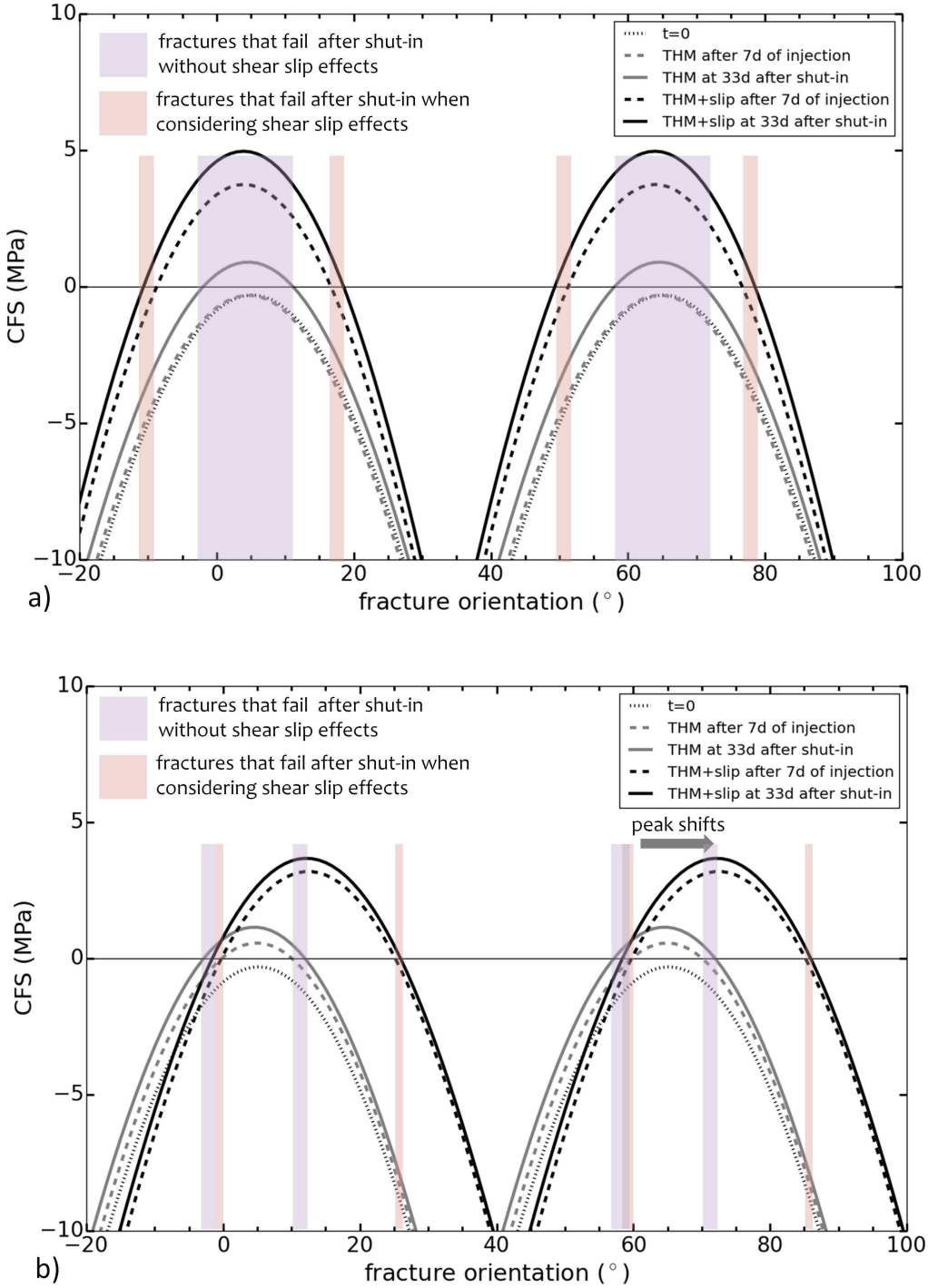

Figure 5.11: CFS as a function of orientation for a point a) within region J (at point x=700, y=70) and b) within region H (at point x=-540, y=70), after 7 days of injection (dashed line) and at 33 days after shut-in (solid line). Grey lines refer to THM effects, whereas black lines are relative to superposition of THM effects and shear slip movement effects. Shadowed regions identify orientations that fail after shut-in, but not during injection.

5.4 Discussion

This study contributes to clarify the specific role of the main mechanisms that may induce seismicity during and after fluid injection operations, such as EGS hydraulic stimulation, wastewater disposal or CO_2 storage. We find that seismicity during injection is mainly induced by overpressure. Cooling enhances the risk of shear failure around the injection well. Nevertheless, while some regions undergo shear failure conditions during injection, other regions become stabilized due to a poromechanical effect (compression driven by pressure gradients). This effect vanishes after the stop of injection, thus destabilizing these zones. Destabilization is enhanced by the stress transfer caused by the shear slip of the (micro)seismic events induced during injection.

To explain induced seismicity, it is frequently assumed that the reduction of effective stresses is equal to the pressure increase (Shapiro et al., 1999; Shapiro and Patzig, 2003; Dinske, 2011), which implicitly assumes that total stresses remain unchanged. Actually, poroelastic effects may cause significant total stress variations (Engelder and Fischer, 1994; Segall and Fitzgerald, 1998; Altmann et al., 2010) and should be taken into consideration in the evaluation of the failure potential due to fluid injection (Kim and Hosseini, 2014; Vilarrasa et al., 2013; Juanes et al., 2016; Chang and Segall, 2016). Our results illustrate the need of acknowledging the poroelastic coupling in a double permeability reservoir, typical of EGS, characterized by a fault zone surrounded by intact rock. The hypothesis of a single fault zone is simplistic, but illustrates the effect of heterogeneities. Fault zones lead to elongated ellipse-like pressure and temperature distribution during injection. Pressure gradients during injection improve stability along fractures near the injector that are parallel to the fault zone (W-fractures) and along fractures far from the injector that are normal to the fault zone (J-fractures) (Fig. 5.8). This behavior is consistent with the intuitive view that fluid overpressure tends to press and close (i.e., increase normal stress) such fractures, which may remain stable despite other destabilizing processes, i.e., cooling or shear slip. However, these fractures experience a rapid decrease in stability (positive ΔCFS) once injection stops (Fig. 5.8), which suggests that shut-in should be operated slowly or by consecutive steps to minimize the risk of felt post-injection earthquakes.

Fluids injected in deep geological formations usually reach the injection interval at a temperature lower than that of the formation (Paterson et al., 2008).

Cooling induces thermal stresses that may cause shear failure in pre-existing fractures normal to the fault zone in the proximity of the well (region K), which is coherent with observations at EGS sites, like the Geyser (Jeanne et al., 2014b). Since cooling persists in the post-injection period (Figs. 5.8 and 5.9), shear slip may occur after shut-in if it was not activated during the injection period (due to heterogeneity in the fault zone rheology, for example). It should be noted that we have neglected the dependence of fluid density and viscosity on temperature in our simulations, in order to isolate thermal effects. However, in reality, cooling causes a significant increase of fluid viscosity, which would lead to greater overpressure (De Simone et al., 2013).

Shear slip stabilizes the region around the slip surface and destabilizes the areas near the tips. If shear slip stress transfer is superimposed to THM effects, W-fractures do not reach failure in the post-injection period (Fig. 5.10). On the other hand, the range of critical orientations is sensibly increased in the H and J regions, where fractures that were initially not optimally oriented for shear failure, will now yield. Thus, post-injection seismicity may occur along structures with orientations different from those yielding during injection. Furthermore, this seismicity may migrate along these non-critically oriented structures because of a "domino effect" (Freed, 2005). This helps in explaining what occurred at the Basel EGS site, where a change in events location and orientation was observed after shut-in (Deichmann et al., 2014). A similar behavior has been also observed at Soultz, where migration of events location following linear structures in the post-injection period has been reported (Caló et al., 2011; Schoenball and Kohl, 2013; Schoenball et al., 2014). Note that the assumed slip distribution corresponds to a cumulative seismic moment of about $3\text{x}10^{14}$ Nm ($M_w = 3.5$), which is similar to that observed at the Soultz and Basel EGS sites after 6-7 days of injection (Dorbath et al., 2009; Buijze et al., 2015).

A significant rotation of the stress tensor has been reported during injection at The Geyser EGS site, up to 35° (Martínez-Garzón et al., 2013), and at Soultz (Schoenball et al., 2014). Schoenball et al. (2014) suggested that these rotations are not completely caused by shear slip stress transfer, but may be the results of HM and TM couplings. However, our simulation results show that stress tensor rotations derive mostly from slips and cannot be explained by hydromechanical or thermomechanical couplings. In fact, the rotation of the stress tensor due to THM effects is very small in our simulations (Figure 5.7a), in spite of (1) the large

variation of pressure and temperature, and (2) the double permeability-stiffness setting which maximizes the growth of shear stresses.

Our representation of the fault zone (planar parallel fault surfaces) is a simplification that does not acknowledge internal fault complexities (Wibberley et al., 2008). The representation of the seismic process (symmetric slip pattern) is also highly simplified. In reality, earthquakes are more complex (see Kanamori and Brodsky, 2004, for a review). We do not take into account rock friction variation, i.e., decay during slip (Cappa and Rutqvist, 2011a) and potential healing when slip stops (Urpi et al., 2016). These effects are critical for modeling the seismic event itself, but not necessarily to study the effect of the seismic displacements on the stress field perturbation. Heterogeneities such as interactions between faults, physical barriers to fault movements and fault propagation, would give rise to irregular, asymmetric slip distributions (Burgmann et al., 1994). We neglected these complexities because they would have hindered the identification of the contribution of each triggering mechanism, i.e., overpressure, cooling and shear slip stress transfer, on induced seismicity, but should be acknowledged in detailed analysis.

Simulation results highlight that both THM coupling and the superposition of THM coupling and shear slip stress transfer may explain the occurrence of post-injection seismicity along fractures that are stabilized by poromechanical effects during injection, but in which the stabilization vanishes after shut-in (Fig. 5.11). Moreover, the range of critical orientations increases, which enhances the likelihood of inducing seismicity because the probability of existence of a critically oriented pre-existing fracture at a point rises. These findings are relevant because the occurrence of felt seismic events induced by fluid injection has increased in recent years (McGarr et al., 2015). Still, the number of injection projects that induce felt induced seismicity is small compared to the number of existing fluid injection projects (Ellsworth, 2013). Moreover, the cases in which post-injection seismic events are of magnitude higher than those induced during injection are even less frequent. And most importantly, this post-injection seismicity cannot be explained only by overpressure, which is the main triggering mechanism of co-injection induced seismicity, because fluid pressure decays quite rapidly after shut-in. Actually, post-injection seismicity can be explained by the superposition of the disappearance of the stabilizing effects caused by pressure gradients and cooling and shear slip stress transfer effects, causing shear failure conditions in

non-critically oriented fractures.

5.5 Conclusions

We find that induced microseismicity may occur during injection in the vicinity of fault zones, where overpressure and cooling propagates elliptically along the fault zone. The associated shear slip causes a stress drop around the slipped surface and concentrates stresses at the tips, thus promoting the propagation of new seismic events that advance away from the injection well in a "domino effect". Cooling and shear slip create conditions in other regions that would be unstable, but are stabilized by the compressive stresses induced by pressure gradients during injection. Such regions become destabilized after shut-in because the pressure gradients dissipate much faster than temperatures gradients and slip effects are irreversible. Note, however, that the orientations of fractures likely to produce post-injection seismicity are limited and do not always coincide with the critically oriented fractures in the initial stress field. Apart from the optimally oriented fractures around the fault zone, the conjugate fractures also become critically stressed, which doubles the likelihood that a critically stressed fracture exists at a point.

Overall, the superposition of thermo-poroelastic effects and shear slip stress transfer explains the occurrence of post-injection seismicity induced in certain fractures, which may not be initially critically stressed. The fact that it is the drop in hydraulic gradients what causes the fast destabilization of fractures suggests that the magnitude of post-injection events can be lowered if injection is not stopped suddenly, but the injection flow rate is reduced slowly.

6

Conclusions

This Thesis improves the understanding of the coupled thermo-hydro-mechanical processes that induce seismicity during and after stimulation and injection operations of Enhanced Geothermal Systems and other fluid injection operations, such as wastewater disposal, geologic carbon storage and hydraulic fracturing operations. The main conclusions of the Thesis are summarized below.

The injection of fluids deforms the aquifer both because pressure gradients act as body forces that push the aquifer in the direction of flow and because the increase in pressure causes a reduction in effective stresses that leads to expansion of the medium. We apply poroelasticity equations to show that deformation capacity of the medium depends not only on its compressibility, but also on the geometry of the reservoir and on the surrounding constraints to deformation. Therefore, the specific storage is non-local, i.e., it depends on the pressure distribution over the whole reservoir. We present analytic solutions to the hydro-mechanical problem of fluid injection (or extraction) into finite reservoirs. We observe that, if the reservoir deformation is constrained by surrounding formations, the HM pressure response deviates significantly from the traditional hydraulic solutions. Thus, poromechanical effects should not be disregarded. Specifically, HM coupling implies that the pressure response propagates faster than predicted by the traditional solution or, alternatively, that pressure variations at a certain time are greater than expected (i.e., calculated according to traditional methods).

When non-isothermal injection is performed, the aquifer is perturbed by two contrasting processes. While overpressure tends to expand the medium, cooling tends to contract it. We compare analytically the similarities and discrepancies between the two forcing and propose easy-to-use solutions for long-term hydraulic and thermal stresses and displacements for unidirectional and radial geometries. Geometry plays an important role, because longitudinal displacements do not cause lateral strains in unidirectional forcing, whereas radial displacements cause

lateral expansion in axially symmetric flow. The resulting expressions can be useful for testing numerical codes and for providing a rapid assessment of the system response to an alteration. Moreover, they help identifying the controlling parameters. The mechanical response is very sensitive to heterogeneity, dimensionality and boundary conditions. In general, both hydraulic and thermal forcing lead to reduction of compressive effective stresses, which leads to more unstable conditions for failure. Pressure driven stresses are independent of the stiffness of the medium, while thermal stresses are proportional to it. Therefore, in stiff reservoirs, thermal stresses may play a decisive role, especially for long-term injection, as heat transport is much slower than pressure propagation.

Despite the utility of analytical solutions, numerical models allow us to investigate the fully coupled thermo-hydro-mechanical processes acknowledging more complex settings. We perform numerical simulations of cold water injection into a fault-intact rock system. In this case, and in general when fluid flow and pressure gradients concentrate in a small region of the domain, a third effect is superimposed on the longitudinal deformation and lateral expansion unveiled by analytical solutions: expansion along the fault generates shear stresses in the adjacent region, which does not expand. Simulation results also show that thermal effects may be critical in the nearby of the injection well. Overpressure affects the stress field, especially within the fracture zone, but it does not necessarily lead to unstable conditions. On the other hand, thermal perturbations cause an increase of the deviatoric stress in the cooled portion of the matrix, provoking unstable conditions. Thus, THM coupling describes processes that can play a key role in the triggering of induced seismicity, especially when the greatest confining stress acts normal to fractures.

We also analyze the superposition of the effects generated by overpressure, cooling and shear slip, both during the injection and in the post-injection period. We find that induced microseismicity may occur during injection in the vicinity of fault zones, where overpressure and cooling propagates elliptically along the fault zone. The associated shear slip causes a stress drop around the slipped surface and concentrates stresses at the tips, thus promoting the propagation of new seismic events that advance away from the injection well in a “domino effect”. Cooling and shear slip create conditions in other regions that would be unstable, but are stabilized by the compressive stresses induced by pressure gradients during injection. Such regions become destabilized after shut-in because

pressure gradients dissipate much faster than temperature gradients and because slip effects are irreversible. The superposition of THM effects and shear slip stress transfer causes a rotation of the stress tensor, which induces post-injection seismicity along fractures that are initially not critically stressed. The fact that it is the drop in hydraulic gradients what causes the fast destabilization of fractures suggests that the magnitude of post-injection events could be lowered if injection is not stopped suddenly, but the injection flow rate is reduced slowly.

A

Volumetric deformation in one-dimensional domain

In the case of one-dimensional domain, the equilibrium equation in the x direction results

$$\frac{\partial \sigma_x}{\partial x} = 0\,. \tag{A.1}$$

Application of Hooke's law (Jaeger et al., 2007) yields

$$\frac{\partial^2 u_x}{\partial x^2} = \frac{a}{2G+\lambda}\,\frac{\partial p}{\partial x}\,, \tag{A.2}$$

where $a/(2G+\lambda)$ can be substituted with α_{p1}. This equation can be integrated to yield (De Simone et al., 2017a)

$$u_x = \alpha_{p1}\left[\int_0^x p(x,t)dx + Ax + B\right] \tag{A.3}$$

and the volumetric deformation is

$$\varepsilon_{vol} = \varepsilon_x = \frac{\partial u_x}{\partial x} = \alpha_{p1}\Big[p(x,t) + A\Big]\,, \tag{A.4}$$

where constants A and B depend on the mechanical BC at the surfaces $x = 0$ and $x = L$. In the case that displacements is constrained at both surfaces ($u = 0$), constants are expressed by

$$A = -\frac{1}{L}\int_0^L p(x,t)dx \tag{A.5}$$

$$B = 0 \quad . \tag{A.6}$$

B

Solution to HM Pressure in one-dimensional domain

Laplace transform with respect to time of Eq. (2.15) yields

$$s\,\widehat{p^*}(x,s) = D\,\frac{\partial^2 \widehat{p^*}(x,s)}{\partial x^2}\,, \tag{B.1}$$

where s is the Laplace variable and the hat denotes the functions in Laplace space. The general solution is given by (Carslaw and Jaeger, 1959)

$$\widehat{p^*}(x,s) = C_1 \exp(\eta x) + C_2 \exp(-\eta x)\,, \tag{B.2}$$

where $\eta = \sqrt{s/D}$.

Constants C_1 and C_2 are defined by the BCs. Constant injection q_0 is applied at the inner boundary ($x = 0$), whereas for the outer boundary ($x = L$) we take into consideration two different boundary conditions, which are constant pressure and zero normal flow. In the case of constant pressure at the outer boundary $x = L$, the conditions are the ones defined in Section 2.3.1:

$$\begin{cases} \dfrac{\partial \widehat{p^*}(x,s)}{\partial x}\,\Big|_{x=0} = -\,\dfrac{q_0}{k/\mu}\,\dfrac{1}{s} & \text{(B.3a)} \\[2ex] \displaystyle\int_0^L \widehat{p^*}(x,s)dx = \frac{1+\theta}{\theta}\,L\,\widehat{p^*}(L,s)\,. & \text{(B.3b)} \end{cases}$$

After deriving the expressions for C_1 and C_2 and applying Eq. (2.18), the

expression of pressure in the Laplace domain is

$$\widehat{p}(x,s) = \frac{q_0}{k/\mu}\,\frac{1}{s\,\eta}\,\cdot \\ \frac{\left[(1+\gamma)\,\mathrm{e}^{-\eta(L-x)} + (1-\gamma)\,\mathrm{e}^{\eta(L-x)} - \mathrm{e}^{\eta x} - \mathrm{e}^{-\eta x} + \mathrm{e}^{\eta L} + \mathrm{e}^{-\eta L} - 2\right]}{(1-\gamma)\,\mathrm{e}^{\eta L} - (1+\gamma)\,\mathrm{e}^{-\eta L}}\,, \quad \text{(B.4)}$$

where $\gamma = (1+\theta)L\eta/\theta$.

The solution is greatly simplified if water and solid grains compressibilities are neglected, so that $\gamma = 0$, which yields

$$\widehat{p}(x,s) = \frac{q_0}{k/\mu}\,\frac{1}{s\,\eta}\,\frac{\mathrm{e}^{-\eta x} - \mathrm{e}^{-\eta(L-x)} - \mathrm{e}^{-\eta L} + 1}{\mathrm{e}^{-\eta L} + 1}\,. \quad \text{(B.5)}$$

Laplace inversion of this equation yields the solution in space and time domains (Eq. (2.20)).

If the hydraulic condition at $x = L$ is of no flow, then Eq. (B.3a) still holds at $x = 0$, but the BC at the outer boundary becomes

$$\left.\frac{\partial \widehat{p^*}(x,s)}{\partial x}\right|_{x=L} = 0 \quad \text{(B.6)}$$

and the solution for $p^*(x,t)$ is

$$\widehat{p^*}(x,s) = \frac{q_0}{k/\mu}\,\frac{1}{s\,\eta}\,\frac{\mathrm{e}^{-\eta x} + \mathrm{e}^{-\eta(2L-x)}}{1 - \mathrm{e}^{-2\eta L}}\,, \quad \text{(B.7)}$$

which can be inverted. After adding the spatial average of pressure $\overline{p}$ (Eq. (2.24)), the solution is given by Eq. (2.25).

C

Volumetric deformation in cylindrical domain

In the case of radial axisymmetry, the equilibrium equation in radial direction results

$$\frac{\partial \sigma_r}{\partial r} + \frac{\sigma_r - \sigma_\theta}{r} = 0\,, \tag{C.1}$$

where we have considered that $\tau_{rz} = 0$, which is valid for both plane stress and plane strain conditions.

Plane strain

Application of Hooke's law (Jaeger et al., 2007) for the case of plane strain in direction z ($\varepsilon_z = 0$)yields

$$\frac{\partial^2 u_r}{\partial r^2} + \frac{1}{r}\frac{\partial u_r}{\partial r} - \frac{1}{r^2}u_r = \frac{a}{2G+\lambda}\,\frac{\partial p}{\partial r}\,, \tag{C.2}$$

where $a/(2G+\lambda)$ can be substituted with α_{p1}. This equation can be integrated to yield (De Simone et al., 2017a)

$$u_r = \alpha_{p1}\left[\frac{1}{r}\int_{r0}^{r} r p(r,t)dr + Cr + \frac{D}{r}\right] \tag{C.3}$$

and the volumetric deformation is

$$\varepsilon_{vol} = \frac{\partial u_r}{\partial r} + \frac{u_r}{r} = \alpha_{p1}\Big[p(r,t) + 2C\Big]\,, \tag{C.4}$$

where constants C and D depend on the mechanical BC at the surfaces $r = r_0$ and $r = R$. We assume zero radial displacements at the inner boundary $u_{r_0} = 0$, whereas we consider two scenarios for the outer boundary, with zero displacements

or zero stress variation, respectively. In the case of zero radial displacements ($u_R = 0$), constant C is expressed by

$$C = -\frac{1}{R^2 - r_0^2} \int_{r_0}^{R} r\, p(r,t) dr \; = -\frac{\overline{p}(t)}{2}. \tag{C.5}$$

In the case of zero radial stress ($\sigma_R = 0$), C is given by

$$\begin{aligned} C = \frac{2G}{(2G + 2\lambda)R^2 + 2Gr_0^2} \int_{r_0}^{R} r p(r,t) dr \\ \approx \frac{G}{G+\lambda} \frac{\overline{p}(t)}{2} = (1-2\nu)\frac{\overline{p}(t)}{2}\,. \end{aligned} \tag{C.6}$$

Plane stress

If plane stress in direction z ($\sigma_z = 0$) is considered, it results

$$\varepsilon_z = \frac{ap}{2G+\lambda} - \frac{\lambda}{2G+\lambda}(\varepsilon_r + \varepsilon_\theta)\,. \tag{C.7}$$

Therefore, the equilibrium equation ends up into

$$\frac{\partial^2 u_r}{\partial r^2} + \frac{1}{r}\frac{\partial u_r}{\partial r} - \frac{1}{r^2} u_r = \frac{a}{2(G+\lambda)} \frac{\partial p}{\partial r}\,, \tag{C.8}$$

which returns

$$u_r = \frac{a}{2(G+\lambda)} \left[\frac{1}{r} \int_{r0}^{r} r\, p(r,t) dr + Cr + \frac{D}{r} \right]\,. \tag{C.9}$$

The volumetric deformation is, thus, given by

$$\varepsilon_{vol} = \frac{\partial u_r}{\partial r} + \frac{u_r}{r} + \varepsilon_z = \alpha_{p2} \left(p(r,t) + \frac{1-2\nu}{1-\nu} C \right)\,, \tag{C.10}$$

where $a/(G+\lambda)$ have been substituted by α_{p2}. The constant C is the same as for the plane strain case ($C = -\overline{p}(t)/2$) in the case of zero radial displacements

($u_R = 0$), whereas in the case of zero radial stress ($\sigma_R = 0$) it is

$$C = \frac{2G + \lambda}{2G + 3\lambda)R^2 + (2G + \lambda)r_0^2} \int_{r_0}^{R} rp(r,t)dr \approx \frac{2G + \lambda}{2G + 3\lambda} \frac{\overline{p}(t)}{2} = \frac{1 - \nu}{1 + \nu} \frac{\overline{p}(t)}{2}. \tag{C.11}$$

D

Solution to HM Pressure in cylindrical domain

Laplace transform with respect to time of Eq. (2.32) yields

$$\frac{\partial^2 \widehat{p^*}(r,s)}{\partial r^2} + \frac{1}{r}\frac{\partial \widehat{p^*}(r,s)}{\partial r} - \frac{s}{D}\,\widehat{p^*}(r,s)\,, \tag{D.1}$$

where s is the Laplace variable and the hat denotes the functions in Laplace space. Its general solution is of the type (Carslaw and Jaeger, 1959)

$$\widehat{p^*}(r,s) = C_1\, I_0\,(\eta r) - \frac{2}{\pi}\, C_2\, K_0\,(\eta r)\ , \tag{D.2}$$

where $\eta = \sqrt{s/D}$, whereas I_0 and K_0 represent the modified Bessel functions of first and second kind, respectively, of order zero. Constants C_1 and C_2 are obtained by applying the hydraulic boundary conditions. As in the linear flow case, we assume constant injection Q_0 at the inner boundary ($r = r_0$), and either constant pressure or zero flow at the outer boundary ($r = R$).

In the first case, the boundary conditions in the Laplace domain are

$$\begin{cases} \lim\limits_{r\to 0}\left(r\ \dfrac{\partial \widehat{p^*}(r,s)}{\partial r}\right) = -\dfrac{Q_0}{2\pi k/\mu}\ \dfrac{1}{s} & \text{(D.3a)} \\[2ex] \displaystyle\int_{r_0}^{R} r\,\widehat{p^*}(r,s)dr = \frac{1+\theta}{\theta}\ \frac{R^2 - r_0^2}{2}\ \widehat{p^*}(R,s)\ . & \text{(D.3b)} \end{cases}$$

After calculation of derivatives and integrals of the Bessel functions (Abramowitz

and Stegun, 1964), the constants are obtained:

$$C_1 = \frac{2}{\pi}\,\frac{Q_0}{4k/\mu}\,\frac{1}{s}\left[\frac{RK_1(R\eta) - r_0K_1(r_0\eta) + \gamma K_0(R\eta)}{RI_1(R\eta) - r_0I_1(r_0\eta) - \gamma I_0(R\eta)}\right], \tag{D.4}$$

$$C_2 = -\frac{Q_0}{4k/\mu}\,\frac{1}{s}, \tag{D.5}$$

where

$$\gamma = \frac{1+\theta}{\theta}\,\frac{R^2 - r_0^2}{2}\,\eta \tag{D.6}$$

and I_1 and K_1 represent the modified Bessel functions of first and second kind, respectively, of the first order.

Once $\widehat{p^*}(r,s)$ is defined, Eq. (2.35) allows to yield the solution for the pressure in the Laplace domain ((2.36)).

In the second case, that is, in the case the flow rate is zero at the outer boundary, Eq. (D.3a) still holds at $r = r_0$, but the BC at $r = R$ becomes

$$\left.\frac{\partial\widehat{p^*}(r,s)}{\partial r}\right|_{r=R} = 0\,. \tag{D.7}$$

Hence, the constants can be easily derived:

$$C_1 = \frac{2}{\pi}\,\frac{Q_0}{4k/\mu}\,\frac{1}{s}\,\frac{K_1(R\eta)}{I_1(R\eta)}, \tag{D.8}$$

$$C_2 = -\frac{Q_0}{4k/\mu}\,\frac{1}{s}\,. \tag{D.9}$$

In order to obtain the solution for pressure, we need to add the average value of pressure to $\widehat{p^*}(r,s)$, which we define in the real space in Eq. (2.40). We transform it into Laplace domain, in order to give the complete expression for the pressure in the Laplace domain (Eq. (2.43)).

E

Integrals of the Temperature field

For the unidirectional analytical solution (Eq. (3.15)) the integrals of pressure and temperature equation are needed. The integral of the pressure field (Eq. (3.11)) is trivial, whereas the integral of the temperature field (Eq. (3.14)) is provided by Ng and Geller (1969), solution 4.1.2

$$\int \Delta T(x)\, dx = \frac{\Delta T_0}{2} \sqrt{4D_T t} \left[\frac{x-\xi}{\sqrt{4D_T t}} \operatorname{erfc}\left(\frac{x-\xi}{\sqrt{4D_T t}} \right) - \frac{1}{\sqrt{\pi}} \exp\left(-\left(\frac{x-\xi}{\sqrt{4D_T t}} \right)^2 \right) \right] \tag{E.1}$$

For the radial case (Eq. (3.23)) we need the integral of the perturbation (ΔF) multiplied by the radius r. For the pressure field, this is easily obtained. For the temperature field, this integral may be obtained making use of the integral provided by Ng and Geller (1969), solution 4.1.5. After some algebra, we obtain

$$\int r\, \Delta T(r)\, dr = \frac{\Delta T_0}{2} \left[\frac{r^2-\varrho^2}{2} \operatorname{erfc}\left(\frac{r-\varrho}{\sqrt{4D_T t}} \right) + \frac{\sqrt{4D_T t}^2}{4} \operatorname{erf}\left(\frac{r-\varrho}{\sqrt{4D_T t}} \right) - \frac{\sqrt{4D_T t}}{\sqrt{\pi}} \frac{r+\varrho}{2} \exp\left(-\left(\frac{r-\varrho}{\sqrt{4D_T t}} \right)^2 \right) \right] \tag{E.2}$$

F

Publications and conference presentations

Publications in scientific journals

De Simone, S., Vilarrasa, V., Carrera, J., Alcolea, A., and Meier, P. (2013). Thermal coupling may control mechanical stability of geothermal reservoirs during cold water injection. *Physics and Chemistry of the Earth, Parts A/B/C. vol. 64, pp. 117–126.*

Pujades, E., Vázquez-Suñé E., Carrera E., Vilarrasa V., **De Simone, S.**, Jurado A., Ledesma A., Ramos G., and Lloret A. (2014). Deep enclosures versus pumping to reduce settlements during shaft excavations. *Engineering Geology 169: 100-111.*

De Simone, S., Carrera, J. and Gómez Castro B. M. (2017). A practical solution to the mechanical perturbations induced by non-isothermal injection into a permeable medium. *International Journal of Rock Mechanics and Mining Sciences 91: 7-17.*

Pujades, E., **De Simone, S.**, Carrera, J., Vázquez-Suñé, E., and Jurado, A. (2017). Settlements around pumping wells: analysis of influential factors and a simple calculation procedure. *Journal of Hydrology - in press.*

De Simone, S. and Carrera, J. (2017). Analytical solutions to coupled HM problems to highlight the non-local nature of aquifer storage. *Submitted.*

De Simone, S., Carrera J. and Vilarrasa, V. (2017). Superposition approach to understand triggering mechanisms of post-injection induced seismicity. *Submitted.*

Presentations in Congresses

2012

De Simone, S., Vilarrasa, V., and Carrera, J. (2012). Fracture instability caused by cold water injection. *EGU General Assembly Conference Abstracts Vol. 14, Vienna, Austria,* 22-27 April 2012.

De Simone, S., Vilarrasa, V., Carrera, J., Alcolea, A., and Meier, P. (2012). Thermo-Hydro-Mechanical Simulation of Geothermal Reservoir Stimulation. *Proceedings of the 4th Workshop of CODE_BRIGHT Users, Barcelona, Spain,* 3 May 2012.

De Simone, S., Vilarrasa, V., Carrera, J., Alcolea, A. and Meier, P. (2012). Coupled thermo-hydro-mechanical modelling of cold water injection in a fractured hot rock. *Proceedings of 2nd Workshop on Advanced Scientific Results from IDAEA, CSIC, Roquetes, Tarragona, Spain*, 14-16 May 2012.

2013

De Simone, S., Vilarrasa, V., Carrera, J., Alcolea, A., and Meier, P. (2013). Modeling the effects of hydraulic stimulation on geothermal reservoirs. *EGU General Assembly Conference Abstracts Vol. 15, Vienna, Austria*, 7-12 April 2013.

De Simone, S., Vilarrasa, V., Carrera, J., Alcolea, A., and Meier, P. (2013). Thermo Hydro Mechanical modeling of hydraulic stimulation in a deep geothermal reservoir. *Congreso sobre aspectos tecnológicos e hidrogeológicos de la geotermia, Barcelona, Spain*, 18-19 April 2013.

2014

De Simone S., Soler J., Carrera J., Slooten L.J., and Ortiz G. (2014). Mechanical characterization of a CO2 fractured reservoir by means of microseismicity induced by high pressure injection tests. *EGU General Assembly Conference Abstracts Vol. 16, Vienna, Austria*, 27 April, 2 May 2014.

Gómez Castro B. M., Fernández López S., Carrera J., **De Simone S.**, Martínez L., Roetting T., Soler J., Ortiz G., de Dios C., and Huber C. (2014). Interpretation of hydraulic tests performed at a carbonate rock site for CO2 storage. *EGU General Assembly Conference Abstracts Vol. 16, Vienna, Austria*, 27 April - 2 May 2014.

De Simone S. and Carrera J. (2014). Potenciales mecanismos de sismicidad inducida en sistemas geotérmicos estimulados. *Congreso Ibérico de las Aguas Subterráneas CIAS, Valencia, Spain*, 8-10 September 2014.

Gómez Castro B.M, Carrera J., Martínez-Landa L., **De Simone S.**, Soler J., Fernández S. (2014). Acoplamiento hidromecánicos en la caracterización de acuíferos salinos profundos para el almacenamiento geológicos de CO2. *Congreso Ibérico de las Aguas Subterráneas CIAS, Valencia, Spain*, 8-10 September 2014.

2015

De Simone S., Carrera J., and Vilarrasa, V. (2015). On the role of processes interaction in the triggering of post-injection seismicity in Enhanced Geothermal Systems. *Schatzalp workshop on induced seismicity, Davos, Switzerland*, 10-13 March 2015.

De Simone S., Carrera J., and Vilarrasa, V. (2015). Interaction of processes may explain induced seismicity after shut-in in Enhanced Geothermal Systems. *EGU General Assembly Conference Abstracts Vol. 17, Vienna, Austria*, 12-17 April 2015.

Gómez Castro B. M., **De Simone S.**, Rossi R., Larese De Tetto A. and Carrera J. Development of a finite element code to solve thermo-hydro-mechanical coupling and simulate induced seismicity. *EGU General Assembly Conference Abstracts Vol. 17, Vienna, Austria*, 12-17 April 2015.

De Simone S. and Carrera J. (2015). Advances in the understanding of the physical processes involved in deep fluid-injection operations. *Summer School on Flow and Transport in Porous and Fractured Media, Development, Protection, Management and Sequestration of Subsurface Fluids, Cargese, Corsica*, 15 July - 1 August 2015.

Gómez Castro B. M., **De Simone S.**, Rossi R., Larese De Tetto A. and Carrera J. Development of a finite element code to solve thermo-hydro-mechanical coupling and simulate induced seismicity. *Summer School on Flow and Transport in Porous and Fractured Media, Development, Protection, Management and Sequestration of Subsurface Fluids, Cargese, Corsica*, 15 July - 1 August 2015.

De Simone S. and Carrera J. (2015). A deep analysis of the processes that may induce seismicity during and after fluid injection into deep reservoirs. *42nd IAH International Congress AQUA2015, Rome, Italy*, 13-18 September 2015.

De Simone S. and Carrera J. (2015). Overview of the physical processes involved in deep fluid-injection operations. *1st Meeting of young researchers from IDAEA-CSIC, Barcelona, Spain*, 22 Octuber 2015.

2016

Pujades E., **De Simone S.**, Carrera J., Vázquez-Suñé E., and Jurado A. (2016). Settlements around pumping wells: distribution, relation with the storage coefficient and role of surrounding layers. *5th International Geologica Belgica 2016 Congress, Mons, Belgium*, 26-29 January 2016.

De Simone S., Carrera J., and Gómez Castro B.M. (2016). Rapid analytical assessment of the mechanical perturbations induced by non-isothermal injection into a subsurface formation. *EGU General Assembly Conference Abstracts Vol. 18, Vienna, Austria*, 17-22 April 2016.

Gómez Castro B. M., De Simone S and Carrera J. (2016). Development of a new code to solve hydro-mechanical coupling, shear failure and tensile failure due to hydraulic fracturing operations. *EGU General Assembly Conference Abstracts Vol. 18, Vienna, Austria*, 17-22 April 2016.

Bibliography

Abramowitz, M. and Stegun, I. A. (1964). Handbook of mathematical functions: with formulas, graphs, and mathematical tables. *Courier Corporation*, 55.

Albaric, J., Oye, V., Langet, N., Hasting, M., Lecomte, I., Iranpour, K., Messeiller, M., and Reid, P. (2014). Monitoring of induced seismicity during the first geothermal reservoir stimulation at paralana, australia. *Geothermics*, 52:120–131.

Altmann, J. B., Müller, T. M., Müller, B. I., Tingay, M. R., and Heidbach, O. (2010). Poroelastic contribution to the reservoir stress path. *International Journal of Rock Mechanics and Mining Sciences*, 47(7):1104–1113.

Anderson, E. (1951). The dynamics of faulting and dyke formation with applications to britain. *Oliver and Boyd.*

Andrews, D. J. (2002). A fault constitutive relation accounting for thermal pressurization of pore fluid. *Journal of Geophysical Research*, 107(B12):2363.

Asanuma, H., Nozaki, H., Niitsuma, H., and Wyborn, D. (2005). Interpretation of microseismic events with large magnitude collected at Cooper Basin, Australia. *Geothermal Resource Council Transactions*, 29:87–91.

Baisch, S. and Harjes, H.-P. (2003). A model for fluid-injection-induced seismicity at the KTB, Germany. *Geophysical Journal International*, 152(1):160–170.

Baisch, S., Vörös, R., Rothert, E., and Stang, H. (2010). A numerical model for fluid injection induced seismicity at Soultz-sous-Forêts. *International Journal of Rock Mechanics and Mining Sciences*, 47(3):405–413.

Baisch, S., Weidler, R., Vörös, R., Wyborn, D., and de Graaf, L. (2006). Induced seismicity during the stimulation of a geothermal HFR reservoir in the Cooper Basin, Australia. *Bulletin of the Seismological Society of America*, 96(6):2242–2256.

Baria, R., Baumga, È., and Rummel, F. (1999). HDR / HWR reservoirs : concepts , understanding and creation. *Geothermics*, 28:533–552.

Baria, R., Michelet, S., Baumgärtner, J., Dyer, B., Nicholls, J., Hettkamp, T., Teza, D., Soma, N., Asanuma, H., Garnish, J., and Megel, T. (2005). Creation and Mapping of 5000 m deep HDR / HFR Reservoir to Produce Electricity. (April):24–29.

Barton, N., Bandis, S., and Bakhtar, K. (1985). Strength, deformation and conductivity coupling of rock joints. *International Journal of Rock Mechanics and Mining Sciences & Geomechanics Abstracts*, 22(3):121–140.

Batchelor, A. (1982). Creation of hot dry rock systems by combined explosive and hydraulic fracturing. *BHRA Fluid Engineering international conference on geothermal energy, Florence, Italy, May 1982, pp. 321-342.*

Batini, F., Bufe, C., Cameli, G., Console, R., and Fiordelisi, A. (1980a). Seismic monitoring in Italian geothermal areas I: seismic activity in the Larderello-Travale region. *In: Proceedings Second DOE-ENEL Workshop on Cooperative Research in Geothermal Energy, Report LBL-11555, Lawrence Berkeley Laboratory, Berkeley, CA, USA, October 20–22, pp. 20–47.*

Batini, F., Cameli, G., Carabelli, E., and Fiordelisi, A. (1980b). Seismic monitoring in Italian geothermal areas II: seismic activity in the geothermal fields during exploitation. *In: Proceedings of Second DOE-ENEL Workshop on Cooperative Research in Geothermal Energy, Report LBL-11555, Lawrence Berkeley Labora- tory, Berkeley, CA, USA, October 20–22, pp. 48–85.*

Batini, F., Console, R., and Luongo, G. (1985). Seismological study of Larderello-Travale geothermal area. *Geothermics 14 (2–3), 255–272.*

Bear, J. and Bachmat, Y. (2012). Introduction to modeling of transport phenomena in porous media. *Vol. 4. Springer Science & Business Media,.*

Bear, J. and Corapcioglu, M. Y. (1981a). Mathematical model for regional land subsidence due to pumping: 1. Integrated aquifer subsidence equations based on vertical displacements only. *Water Resources Research*, 17(4):937–946.

Bear, J. and Corapcioglu, M. Y. (1981b). Mathematical model for regional land subsidence due to pumping: 2. Integrated aquifer subsidence equations for vertical and horizontal displacements. *Water Resources Research*, 17(4):947–958.

Berg, S. J., Hsieh, P. a., and Illman, W. a. (2011). Estimating hydraulic parameters when poroelastic effects are significant. *Groundwater*, 49(6):815–29.

Biot, M. A. (1941). General theory of three-dimensional consolidation. *Journal of Applied Physics*, 12(2):155–164.

Biot, M. A. (1956a). General solutions of the equations of elasticity and consolidation for a porous material. *Journal of applied mechanics*, 23(1):91–96.

Biot, M. A. (1956b). Thermoelasticity and Irreversible Thermodynamics. *Journal of Applied Physics*, 27(3):240.

Bjornsson, G. (2004). Reservoir conditions at 3-6 km depth in the Hellisheidi Geothermal Field, SW Iceland, estimated by deep drilling, coldwater injection, and seismic monitoring. *In: Proceedings 29th Workshop on Geothermal Reservoir Engineering, Stanford University, Stanford, CA, USA, January 26–28, pp. 67–74.*

Bönnemann, C., Schmidt, B., Ritter, J., Gestermann, N., Plenefisch, T., and Wegler, U. (2010). Das seismische Ereignis bei Landau vom 15 August 2009 (The seismic event near Landau of 15th August 2010). Final report by the expert panel on seismic risk associated with hydrothermal geothermal plants,. *Landesamt für Geologie und Bergbau of Rheinland-Pfalz (Regional authority for geology and mines of Rheinland-Pfalz), 54 pp.*

Bommer, J. J., Oates, S., Cepeda, J. M., Lindholm, C., Bird, J., Torres, R., Marroquín, G., and Rivas, J. (2006). Control of hazard due to seismicity induced by a hot fractured rock geothermal project. *Engineering Geology*, 83(4):287–306.

Bruel, D. (2002). Impact of Induced Thermal Stresses During Circulation Tests in an Engineered Fractured Geothermal Reservoir. *Oil & Gas Science and Technology*, 57(5):459–470.

Brustle, W. and Stange, S. (2000). Ann bull state surv geol nat resour min, baden-wuerttemberg.

Buijze, L., Wassing, B., Fokker, P. A., and Wees, J. D. V. (2015). Moment Partitioning for Injection-Induced Seismicity: Case Studies & Insights from Numerical Modeling. *World Geothermal Congress 2015*, (April):19–25.

Burbey, T. J. (1999). Effects of horizontal strain in estimating specific storage and compaction in confined and leaky aquifer systems. *Hydrogeology Journal*, 7(6):521–532.

Burbey, T. J. (2001). Storage coefficient revisited: Is purely vertical strain a good assumption? *Ground Water*, 39(3):458–464.

Burgmann, R., Pollard, D. D., and Martel, S. J. (1994). Slip distributions on faults: effects of stress gradients, inelastic deformation, heterogeneous host-rock stiffness, and fault interaction. *Journal of Structural Geology*, 16(12):1675–1690.

Byerlee, J. (1978). Friction of rocks. *Pure and applied Geophysics*, 116(4-5):615–626.

Caló, M., Dorbath, C., Cornet, F. H., and Cuenot, N. (2011). Large-scale aseismic motion identified through 4-D P-wave tomography. *Geophysical Journal International*, 186(3):1295–1314.

Cappa, F. and Rutqvist, J. (2011a). Impact of CO2 geological sequestration on the nucleation of earthquakes. *Geophysical Research Letters*, 38(17):n/a–n/a.

Cappa, F. and Rutqvist, J. (2011b). Modeling of coupled deformation and permeability evolution during fault reactivation induced by deep underground injection of CO2. *International Journal of Greenhouse Gas Control*, 5(2):336–346.

Carabelli, E., Moia, F., and Fiordelisi, A. (1984). Seismic monitoring during geothermal wells stimulation as contribution to the individuation of prevailing fracturation trends. *In: Presented at Seminar on Utilization of Geothermal Energy for Electric Power Production and Space Heating, Florence, Italy, May 14–17, pp. 1–31.*

Carslaw, H. S. and Jaeger, J. C. (1959). Conduction of heat in solids. *Oxford: Clarendon Press, 1959, 2nd ed.*

Cataldi, F., Meier, M.-A., and Wiemer, S. (2013). The role of Coulomb stress changes for injection-induced seismicity: The Basel enhanced geothermal system. *Geophysical Research Letters*, 40(1):72–77.

Chang, K. W. and Segall, P. (2016). Injection induced seismicity on basement faults including poroelastic stressing. *Journal of Geophysical Research: Solid Earth*, 121:n/a–n/a.

Charléty, J., Cuenot, N., Dorbath, L., Dorbath, C., Haessler, H., and Frogneux, M. (2007). Large earthquakes during hydraulic stimulations at the geothermal site of Soultz-sous-Forêts. *International Journal of Rock Mechanics and Mining Sciences*, 44(8):1091–1105.

Chen, C.-S. (1984). A reinvestigation of the analytical solution for drawdown distributions in a finite confined aquifer. *Water Resources Research*, 20(10):1466–1468.

Cho, H., Kardomateas, G., and Valle, C. (1998). Elastodynamic solution for the thermal shock stresses in an orthotropic thick cylindrical shell. *Journal of applied mechanics*, 65(1):184–193.

CIMNE (2012). Kratos - www.cimne.com/kratos/.

Cornet, F. H., Hlm, J. H., Poitrenaud, H. P., and Etchecopar, A. E. (1997). Seismic and Aseismic Slips Induced by Large-scale Fluid Injections. *Pure and Applied Geophysics*, 150:563–583.

Dadvand, P., Rossi, R., and Oñate, E. (2010). An object-oriented environment for developing finite element codes for multi-disciplinary applications. *Archives of computational methods in engineering*, 17(3):253–297.

de Marsily, G. (1981). Quantitative hydrogeology. *Academic Press.*

De Simone, S. and Carrera, J. (2017). Analytical solutions to coupled HM problems to highlight the non-local nature of aquifer storage. *submitted.*

De Simone, S., Carrera, J., and Gómez-Castro, B. M. (2017a). A practical solution to the mechanical perturbations induced by non-isothermal injection into a permeable medium. *International Journal of Rock Mechanics and Mining Sciences*, 91:7–17.

De Simone, S., Carrera, J., and Vilarrasa, V. (2017b). Superposition Approach to Understand Triggering Mechanisms of Post-Injection Induced Seismicity. *submitted*.

De Simone, S., Vilarrasa, V., Carrera, J., Alcolea, A., and Meier, P. (2013). Thermal coupling may control mechanical stability of geothermal reservoirs during cold water injection. *Physics and Chemistry of the Earth, Parts A/B/C*, 64:117–126.

Deichmann, N. and Ernst, J. (2009). Earthquake focal mechanisms of the induced seismicity in 2006 and 2007 below Basel (Switzerland). *Swiss Journal of Geosciences*, 102(3):457–466.

Deichmann, N. and Giardini, D. (2009). Earthquakes Induced by the Stimulation of an Enhanced Geothermal System below Basel (Switzerland). *Seismological Research Letters*, 80(5):784–798.

Deichmann, N., Kraft, T., and Evans, K. F. (2014). Identification of faults activated during the stimulation of the Basel geothermal project from cluster analysis and focal mechanisms of the larger magnitude events. *Geothermics*, 52:84–97.

Delleur, J. W. (1999). The handbook of groundwater engineering. *CRC Press LLC, Florida*.

Dempsey, D., Kelkar, S., Pawar, R., Keating, E., and Coblentz, D. (2014). Modeling caprock bending stresses and their potential for induced seismicity during CO2 injection. *International Journal of Greenhouse Gas Control*, 22:223–236.

Detournay, E. and Cheng, A. A. H.-D. (1993). Fundamentals of poroelasticity. *Chapter 5 in Comprehensive Rock Engineering: Principles, Practice and Projects, II*, II.

Dinske, C. (2011). *Interpretation of Fluid-Induced Seismicity at Geothermal and Hydrocarbon Reservoirs of Basel and Cotton Valley*. Ph.d thesis.

Dorbath, L., Cuenot, N., Genter, A., and Frogneux, M. (2009). Seismic response of the fractured and faulted granite of Soultz-sous-Forêts (France) to 5 km deep massive water injections. *Geophysical Journal International*, 177(2):653–675.

Ellsworth, W. L. (2013). Injection-Induced Earthquakes. *Science*, 341(6142):1225942–1225942.

Engelder, T. and Fischer, M. (1994). Influence of poroelastic behavior on the magnitude of minimum horizontal stress, Sh in overpressured parts of sedimentary basins. *Geology*, 22.

Evans, K. F., Moriya, H., Niitsuma, H., Jones, R. H., Phillips, W. S., Genter, A., Sausse, J., Jung, R., and Baria, R. (2005). Microseismicity and permeability enhancement of hydrogeologic structures during massive fluid injections into granite at 3 km depth at the Soultz HDR site. *Geophysical Journal International*, 160(1):389–412.

Evans, K. F., Zappone, A., Kraft, T., Deichmann, N., and Moia, F. (2012). A survey of the induced seismic responses to fluid injection in geothermal and CO2 reservoirs in Europe. *Geothermics*, 41:30–54.

Faulkner, D. R., Mitchell, T. M., Healy, D., and Heap, M. J. (2006). Slip on 'weak' faults by the rotation of regional stress in the fracture damage zone. *Nature*, 444(7121):922–5.

Ferronato, M., Gambolati, G., Janna, C., and Teatini, P. (2008). Numerical modelling of regional faults in land subsidence prediction above gas/oil reservoirs. *International journal for numerical and analytical methods in geomechanics*, 32(6):633–657.

Freed, A. M. (2005). Earthquake Triggering By Static, Dynamic, and Postseismic Stress Transfer. *Annual Review of Earth and Planetary Sciences*, 33(1):335–367.

Gambolati, G. (1974). Second-order theory of flow in three-dimensional deforming media. *Water Resources Research*, 10(6):1217–1228.

Geertsma, J. (1957). A remark on the analogy between thermoelasticity and the elasticity of saturated porous media. *Journal of the Mechanics and Physics of Solids*, 6(1):13–16.

Genter, A., Fritsch, D., Cuenot, N., Baumgärtner, J., and Graff, J.-J. (2009). Overview of the Current Activities of the European EGS Soultz Project: From Exploration To Electricity Production. *Thirty-Fourth Workshop on Geothermal Reservoir Engineering*.

Genter, A., Traineau, H., Ledésert, B., Bourgine, B., and Gentier, S. (2000). Over 10 Years of Geological Investigations withing the HDR Soultz Project, France. *World Geothermal Congress 2000*, pages 3706–3712.

Ghassemi, A. (2012). A Review of Some Rock Mechanics Issues in Geothermal Reservoir Development. *Geotechnical and Geological Engineering*, 30(3):647–664.

Ghassemi, A., Nygren, A., and Cheng, A. (2008). Effects of heat extraction on fracture aperture: A poro–thermoelastic analysis. *Geothermics*, 37(5):525–539.

Ghassemi, A., Tarasovs, S., and Cheng, A.-D. (2007). A 3-D study of the effects of thermomechanical loads on fracture slip in enhanced geothermal reservoirs.

International Journal of Rock Mechanics and Mining Sciences, 44(8):1132–1148.

Ghassemi, a. and Zhou, X. (2011). A three-dimensional thermo-poroelastic model for fracture response to injection/extraction in enhanced geothermal systems. *Geothermics*, 40(1):39–49.

Giardini, D. (2009). Geothermal quake risks must be faced. *Nature*, 462(7275):848–849.

Goodman, R. E. (1989.). Introduction to rock mechanics. vol. 2. *New York: Wiley*.

Gudmundsson, A. (2004). Effects of Young's modulus on fault displacement. *Comptes Rendus Geoscience*, 336(1):85–92.

Hantush, M. S. (1961). Drawdown around a partially penetrating well. *Journal of the Hydraulics Division*, 87(4):83–98.

Häring, M. O., Schanz, U., Ladner, F., and Dyer, B. C. (2008). Characterisation of the Basel 1 enhanced geothermal system. *Geothermics*, 37(5):469–495.

Harris, R. (1998). Introduction to special section: Stress triggers, stress shadows, and implications for seismic hazard. *Journal of Geophysical Research*, 103:347–358.

Hasting, M., Albaric, J., Oye, V., Reid, P., Messeiller, M., Llanos, E., Malin, P., Shalev, E., Hogg, M., Alvarez, M., et al. (2011). Real-time induced seismicity monitoring during wellbore stimulation at Paralana-2 South Australia.

Helm, D. C. (1994). Horizontal aquifer movement in a Theis-Thiem confined system. *Water Resources Research*, 30(4):953–964.

Hillis, R. (2000). Pore pressure/stress coupling and its implications for seismicity. *Exploration Geophysics*, 31(2):448.

Hoek, E. (2006). Practical rock engineering. *http: www. rocscience. com*.

Hojka, K., Dusseault, M., and Bogobowicz, A. (1993). Analytical Solutions For Transient Thermoelastic Stress Fields Around A Borehole During Fluid Injection Into Permeable Media. *Journal of Canadian Petroleum Technology*, 32(04).

Hoopes, J. A. and Harleman, D. R. (1967). Dispersion in Radial Flow from a Recharge Well. *Journal of Geophysical Research*, 72(14).

Hsieh, P. A. (1986). A New Formula for the Analytical Solution of the Radial Dispersion Problem. *Water Resources Research*, 22(11):1597–1605.

Hsieh, P. A. (1996). Deformation-induced changes in hydraulic head during ground-water withdrawal. *Ground Water*, 34(6):1082–1089.

Hsieh, P. a. and Cooley, R. L. (1995). Comment on "Horizontal aquifer movement in a Theis-Theim Confined System" by Donald C. Helm. *Water Resources Research*, 31(12):3107–3111.

Hubbert, M. and Rubey, W. (1959). Role of fluid pressure in mechanics of overthrust faulting 1. mechanics of fluid filled porous solids and its application of over- thrust faulting. *Geological Society of America Bulletin 70 (2), 115e166.*

Jacob, C. E. (1940). On the flow of water in an elastic artesian aquifer. *Eos, Transactions American Geophysical Union*, 21(2):574–586.

Jaeger, J. C., Cook, N. G., and Zimmerman, R. (2007). Fundamentals of rock mechanics. *Blackwell Publishing.*

Jeanne, P., Rutqvist, J., Dobson, P. F., Walters, M., Hartline, C., and Garcia, J. (2014a). The impacts of mechanical stress transfers caused by hydromechanical and thermal processes on fault stability during hydraulic stimulation in a deep geothermal reservoir. *International Journal of Rock Mechanics and Mining Sciences*, 72:149–163.

Jeanne, P., Rutqvist, J., Hartline, C., Garcia, J., Dobson, P. F., and Walters, M. (2014b). Reservoir structure and properties from geomechanical modeling and microseismicity analyses associated with an enhanced geothermal system at The Geysers, California. *Geothermics*, 51:460–469.

Jha, B. and Juanes, R. (2014). Coupled multiphase flow and poromechanics: A computational model of pore pressure effects on fault slip and earthquake triggering. *Water Resources Research*, 50:3776–3808.

Jost, M., Büßelberg, T., Jost, Ö., and Harjes, H.-P. (1998). Source parameters of injection-induced microearthquakes at 9 km depth at the KTB deep drilling site, Germany. *Bulletin of the Seismological Society of America*, 88(3):815–832.

Juanes, R., Jha, B., Hager, B. H., Shaw, J. H., Plesch, A., Astiz, L., Dieterich, J. H., and Frohlich, C. (2016). Were the May 2012 Emilia-Romagna earthquakes induced? A coupled flow-geomechanics modeling assessment. *Geophysical Research Letters*, (May 2012):6891–6897.

Jung, R. (2013). EGS — Goodbye or Back to the Future. *ISRM International Conference for Effective and Sustainable Hydraulic Fracturing. International Society for Rock Mechanics.*

Jung, R. (2014). Application and potential of hydraulic-fracturing for geothermal energy production. *Swiis. Bull. angew. Geol., Vol. 19/2.*

Kanamori, H. and Brodsky, E. E. (2004). The physics of earthquakes. *Reports on Progress in Physics*, 67(8):1429–1496.

Kim, S. and Hosseini, S. A. (2014). Geological CO2 storage: Incorporation of pore-pressure/stress coupling and thermal effects to determine maximum sustainable pressure limit. *Energy Procedia*, 63:3339–3346.

King, G., Stein, R., and Lin, J. (1994). Static stress changes and the triggering of earthquakes. *Bulletin of the Seismological Society of America*.

Kocabas, I. (2004). An Analytical Model of Temperature and Stress Fields During Cold-Water Injection Into an Oil Reservoir. *SPE Production & Operations*, 21(2).

Koh, J., Roshan, H., and Rahman, S. S. (2011). A numerical study on the long term thermo-poroelastic effects of cold water injection into naturally fractured geothermal reservoirs. *Computers and Geotechnics*, 38(5):669–682.

Kohl, T., Evans, K. F., Hopkirk, R., and Rybach, L. (1995). Coupled hydraulic, thermal and mechanical considerations for the simulation of hot dry rock reservoirs. *Geothermics*, 24(3):345–359.

Kolditz, O. and Clauser, C. (1998). Numerical Simulation of Flow and Heat Transfer in Fractured Crystalline Rocks: Application to the Hot Dry Rock Site in Rosemanowes (U.K.). *Geothermics*, 27(1):1–23.

Kraft, T., Wassermann, J., Deichmann, N., and Stange, S. (2009). The 2008 earthquakes in the Bavarian Molasse Basin – possible relation to geothermics? *In: Proceedings of European Geophysical Union General Assembly Research Abstracts, European Geophysical Union. Vol. 11, EGU2009-10593-6, Vienna, Austria, April 19–24, p. 1.*

Langguth, H. and Treskatis, C. (1989). Reverse water level fluctuations in semi-confined aquifer systems—"Rhade effect". *Journal of Hydrology*, 109(1):79–93.

Lau, L.-K. S. (1959). Disperion of a water tracer in radial laminar flow through homogeneous porous media. *Hydraulic Laboratory and Sanitary Engineering Research Laboratory, University of California, Berkeley.*

Majer, E., Baria, R., Stark, M., Oates, S., Bommer, J., Smith, B., and Asanuma, H. (2007). Induced seismicity associated with Enhanced Geothermal Systems. *Geothermics*, 36(3):185–222.

Majer, E. L. and Peterson, J. E. (2007). The impact of injection on seismicity at The Geysers, California Geothermal Field. *International Journal of Rock Mechanics and Mining Sciences*, 44(8):1079–1090.

Mallikamas, W. and Rajaram, H. (2005). On the anisotropy of the aperture correlation and effective transmissivity in fractures generated by sliding between identical self-affine surfaces. *Geophysical research letters*, 32(11).

Martínez-Garzón, P., Bohnhoff, M., Kwiatek, G., and Dresen, G. (2013). Stress tensor changes related to fluid injection at the Geysers geothermal field, California. *Geophysical Research Letters*, 40(11):2596–2601.

McClure, M. and Horne, R. (2012). The effect of fault zone development on induced seismicity. *PROCEEDINGS, Thirty-Seventh Workshop on Geothermal Reservoir Engineering Stanford University, Stanford, California, January 30 - February 1, 2012*.

McClure, M. W. and Horne, R. N. (2011). Investigation of injection-induced seismicity using a coupled fluid flow and rate/state friction model. *Geophysics*, 76(6):WC181.

McDermott, C. I., Randriamanjatosoa, A. R., Tenzer, H., and Kolditz, O. (2006). Simulation of heat extraction from crystalline rocks: The influence of coupled processes on differential reservoir cooling. *Geothermics*, 35(3):321–344.

McGarr, A., Bekins, B., Burkardt, N., Dewey, J., Earle, P., Ellsworth, W., Ge, S., Hickman, S., Holland, A., Majer, E., Rubinstein, J., and Sheehan, A. (2015). Coping with earthquakes induced by fluid injection. *Science*, 347(6224):830–831.

McTigue, D. F. (1986). Thermoelastic Response of Fluid-Saturated Porous Rock. *Journal of Geophysical Research*, 91:9533–9542.

Meier, P. M., Carrera, J., and Sánchez-Vila, X. (1998). An evaluation of Jacob's method for the interpretation of pumping tests in heterogeneous formations. *Water Resources Research*, 34(5):1011–1025.

Meinzer, O. E. (1928). Compressibility and elasticity of artesian aquifers. *Economic Geology*, 23(3):263–291.

Mitchell, J. K., Soga, K., et al. (2005). Fundamentals of soil behavior. *John Wiley & Sons Hoboken, NJ*.

Moia, F. (2008). Individuazione ed applicazione di metodologie di monitoraggio di possibili fughe di CO2 dai serbatoi di stoccaggio (Identification and application of methodologies for monitoring potential CO2 leakage from storage reser- voirs). *Report no. 08001015 CESI RICERCA. ASV Ambiente e Sviluppo Sostenibile, Milano, Italy, 64 pp.*

Morris, A., Ferrill, D. A., and Henderson, D. B. (1996). Slip-tendency analysis and fault reactivation. *Geology*, 24(3):275–278.

Mossop, A. (2001). *Seismicity , subsidence and strain at The Geysers geothermal field*. PhD thesis.

Mossop, A. and Segall, P. (1997). Subsidence at The Geysers Geothermal Field, N. California from a comparison of GPS and leveling surveys. *Geophysical Research Letters*, 24(14):1839–1842.

Narasimhan, T. (2006). On Storage Coefficient and Vertical Strain. *Ground Water*, 44(3):488–491.

Narasimhan, T. and Kanehiro, B. (1980). A note on the meaning of storage coefficient. *Water Resources Research*, 16(2):423–429.

National Academy of Science (2012). Induced Seismicity Potential in Energy Technologies. Technical report.

Ng, E. W. and Geller, M. (1969). A table of integrals of the error functions. *Journal of research of the National Bureau of Standards - B. Mathematical Sciences*, 73B(1).

Norris, A. (1992). On the correspondence between poroelasticity and thermoelasticity. *Journal of Applied Physics*, 71(3):1138.

Nur, A. and Byerlee, J. (1971). An exact Effective Stress Law for Elastic Deformation of Rock with Fluids. *Journal of Geophysical Research*, 76(26):6414–6419.

Ogata, A. (1970). Theory of Dispersion in a Granular Medium. *Geological Survey Professional Paper*, 411(1):34.

Olivella, S., Carrera, J., Gens, A., and Alonso, E. (1994). Nonisothermal multiphase flow of brine and gas through saline media. *Transport in porous media*, 15(3):271–293.

Olivella, S., Gens, a., Carrera, J., and Alonso, E. (1996). Numerical formulation for a simulator (CODE_BRIGHT) for the coupled analysis of saline media. *Engineering Computations*, 13(7):87–112.

Oppenheimer, D. H. (1986). Extensional tectonics at The Geysers geothermal area, California. *Journal of Geophysical Research: Solid Earth*, 91(B11):11463–11476.

Palciauskas, V. V. and Domenico, P. a. (1982). Characterization of drained and undrained response of thermally loaded repository rocks. *Water Resources Research*, 18(2):281–290.

Pandey, S., Chaudhuri, A., and Kelkar, S. (2017). A coupled thermo-hydro-mechanical modeling of fracture aperture alteration and reservoir deformation during heat extraction from a geothermal reservoir. *Geothermics*, 65:17–31.

Parotidis, M., Shapiro, S. A., and Rothert, E. (2004). Back front of seismicity induced after termination of borehole fluid injection. *Geophysical Research Letters*, 31(2):n/a–n/a.

Paterson, L., Lu, M., Connell, L., and Ennis-King, J. P. (2008). Numerical modeling of pressure and temperature profiles including phase transitions in carbon dioxide wells. *In SPE Annual Technical Conference and Exhibition. Society of Petroleum Engineers.*

Pearson, C. (1981). The relationship between microseismicity and high pore pressures during hydraulic stimulation experiments in low permeability granitic rocks. *Journal of Geophysical Research*, 86:7855–7864.

Perkins, T. and Gonzalez, J. (1984). Changes in earth stresses around a wellbore caused by radially symmetrical pressure and temperature gradients. *Society of Petroleum Engineers Journal*, 24(02):129–140.

Perkins, T. and Gonzalez, J. (1985). The effect of thermoelastic stresses on injection well fracturing. *Society of Petroleum Engineers Journal*, 25(01):78–88.

Pine, R. and Batchelor, A. (1984). Downward migration of shearing in jointed rock during hydraulic injections. *International Journal of Rock Mechanics and Mining Sciences & Geomechanics Abstracts Mining Sciences*, 21(5):249–263.

Poland, J. F. and Davis, G. H. (1969). Land subsidence due to withdrawal of fluids. *Reviews in engineering geology*, 2:187–270.

Pujades, E., De Simone, S., Carrera, J., Vázquez-Suñé, E., and Jurado, A. (2017). Settlements around pumping wells: analysis of influential factors and a simple calculation procedure. *Journal of Hydrology - in press.*

Raimondi, P., Gardner, G. H. F., and Petrick, C. B. (1959). Effect of pore structure and molecular diffusion on the mixing of miscible liquids flowing in porous media. *AIChE-SPE Joint Symposium, San Francisco.*

Raleigh, C. B., Healy, J. H., and Bredehoeft, J. D. (1976). An experiment in earthquake control at Rangely, Colorado. *American Association for the Advancement of Science*, 191(4233):1230–7.

Renard, P. and De Marsily, G. (1997). Calculating equivalent permeability: a review. *Advances in water resources*, 20(5):253–278.

Rice, J. and Cleary, M. (1976). Some basic stress diffusion solutions for fluid-saturated elastic porous media with compressible constituents. *Reviews of Geophysics*, 14(2).

Rice, J. R. and Dunham, E. M. (2009). Thermo- and hydro-mechanical processes along faults during rapid slip. *Meso-Scale Shear Physics in Earthquake and Landslide mechanics*, pages 3–16.

Ripperger, J., Philipp, K., Donat, F., and Giardini, D. (2009). Ground motion and macroseismic intensities of a seismic event of Basel — observations and modelling. *Geophysical Journal International*, 179:1757–1771.

Rozhko, A. Y. (2010). Role of seepage forces on seismicity triggering. *Journal of Geophysical Research: Solid Earth*, 115(11):1–12.

Rubinstein, J. L. and Mahani, A. B. (2015). Myths and Facts on Wastewater Injection, Hydraulic Fracturing, Enhanced Oil Recovery, and Induced Seismicity. *Seismological Research Letters*, 86(4):1060–1067.

Rudnicki, J. W. (1986). Fluid mass sources and point forces in linear elastic diffusive solids. *Mechanics of Materials*, 5(4):383–393.

Rudnicki, J. W. (1987). Plane Strain Dislocations in Linear Elastic Diffusive Solids. *Journal of Applied Mechanics*, 54(3):545.

Rudnicki, J. W. (1999). Alteration of regional stress by reservoirs and other inhomogeneities : stabilizing or destabilizing? *Proceedings of the Ninth International Congress on Rock Mechanics*, 3.

Rutledge, J. T. and Phillips, W. S. (2003). Case History Hydraulic stimulation of natural fractures as revealed by induced microearthquakes, Carthage Cotton Valley gas field, east Texas. *Geophysics*, 68(2):441–452.

Rutqvist, J. (2010). Predicting the spatial extent of injection-induced zones of enhanced permeability at the northwest Geysers EGS demonstration project. *Lawrence Berkeley National Laboratory*.

Rutqvist, J. (2015). Fractured rock stress-permeability relationships from in situ data and effects of temperature and chemical-mechanical couplings. *Geofluids*, 15(1-2):48–66.

Rutqvist, J., Birkholzer, J. T., and Tsang, C. F. (2008). Coupled reservoir-geomechanical analysis of the potential for tensile and shear failure associated with CO2 injection in multilayered reservoir-caprock systems. *International Journal of Rock Mechanics and Mining Sciences*, 45(2):132–143.

Rutqvist, J., Rinaldi, A. P., Cappa, F., and Moridis, G. J. (2013). Modeling of fault reactivation and induced seismicity during hydraulic fracturing of shale-gas reservoirs. *Journal of Petroleum Science and Engineering*, 107:31–44.

Rutqvist, J. and Stephansson, O. (2003). The role of hydromechanical coupling in fractured rock engineering. *Hydrogeology Journal*, 11(1):7–40.

Sanchez-Vila, X., Guadagnini, A., and Carrera, J. (2006). Representative hydraulic conductivities in saturated groundwater flow. *Reviews of Geophysics*, 44(3).

Sanchez-Vila, X., Meier, P. M., and Carrera, J. (1999). Pumping tests in heterogeneous aquifers: An analytical study of what can be obtained from their interpretation using Jacob's method. *Water Resources Research*, 35(4):943–952.

Sauty, J. (1980). An Analysis of Hydrodispersive Transfer in Aquifers. *Water Resources Research*, 16(1):145–158.

Schanz, U., Stang, H., H., T., Homeier, G., Hase, M., Baisch, S., Weidler, R., Macek, A., and Uhlig, S. (2003). Hot dry rock project URACH – A general overview. *In: Proceed- ings of European Geothermal Conference, Szeged, Hungary, 25–30 May 2003, p. 9.*

Schoenball, M., Baujard, C., Kohl, T., and Dorbath, L. (2012). The role of triggering by static stress transfer during geothermal reservoir stimulation. *Journal of Geophysical Research*, 117(B9):B09307.

Schoenball, M., Dorbath, L., Gaucher, E., Wellmann, J. F., and Kohl, T. (2014). Change of stress regime during geothermal reservoir stimulation. *Geophysical Research Letters*, 41(4):1163–1170.

Schoenball, M. and Kohl, T. (2013). The Peculiar Shut-In Behavior of the Well GPK2 at Soultz-sous-Forêts. *GRC Transactions*, 37.

Schultz, R. A. (1996). Relative scale and the strength and deformability of rock masses. *Journal of Structural Geology*, 18(9):1139–1149.

Segall, P. (1989). Earthquakes triggered by fluid extraction. *Geology*, 17(10):942–946.

Segall, P. and Fitzgerald, S. (1998). A note on induced stress changes in hydrocarbon and geothermal reservoirs. *Tectonophysics*, 289(1-3):117–128.

Segall, P., Grasso, J.-R., and Mossop, A. (1994). Poroelastic stressing and induced seismicity near the Lacq gas field, southwestern France. *Journal of Geophysical Research*, 99(B8):15423.

Segall, P. and Lu, S. (2015). Injection-induced seismicity: Poroelastic and earthquake nucleation effects. *Journal of Geophysical Research: Solid Earth*, 120(7):5082–5103.

Shahani, A. and Nabavi, S. (2007). Analytical solution of the quasi-static thermoelasticity problem in a pressurized thick-walled cylinder subjected to transient thermal loading. *Applied Mathematical Modelling*, 31(9):1807–1818.

Shapiro, S., Audigane, P., and Royer, J. (1999). Large-scale in situ permeability tensor of rocks from induced microseismicity. *Geophysical Journal International*, 137(1):207–213.

Shapiro, S. and Patzig, R. (2003). Triggering of seismicity by pore-pressure perturbations: Permeability-related signatures of the phenomenon. *Pure and Applied Geophysics*, 160:1051–1066.

Sibson, R. H. (1973). Interactions between Temperature and Pore-Fluid Pressure during Earthquake Faulting and a Mechanism for Partial or Total Stress Relief. *Nature*, 243:66–68.

Skempton, A. W. (1954). The pore-pressure coefficients A and B. *Geotechnique 4.4: 143-147.*

Streit, J. E. and Hillis, R. R. (2004). Estimating fault stability and sustainable fluid pressures for underground storage of CO2 in porous rock. *Energy*, 29(9-10):1445–1456.

Tang, D. H. and Babu, D. K. (1979). Analytical Solution of a Velocity Dependent Dispersion Problem. *Water Resources Research*, 15(6).

Tenzer, H., Schanz, U., Stang, U., Baisch, S., and Weidler, R. (2004). Potential for geothermal power production from deep hot crystalline rock at Bad Urach (Southern Germany). *Zeitschrift für Angewandte Geologie 2, 43–49.*

Terakawa, T., Miller, S. A., and Deichmann, N. (2012). High fluid pressure and triggered earthquakes in the enhanced geothermal system in Basel, Switzerland. *Journal of Geophysical Research: Solid Earth*, 117(May):1–15.

Terzaghi, K. (1923). Die Berechnung der Durchlässigkeitziffer des Tones aus dem Verlauf der hydrodynamischen Spannungs- erscheinungen. *Akad Wissensch Wien Sitzungsber Math- naturwissensch Klasse IIa*, 142(3/4).

Tester, J. W., Anderson, B. J., Batchelor, A. S., Blackwell, D. D., DiPippo, R., Drake, E. M., Garnish, J., Livesay, B., Moore, M. C., Nichols, K., Petty, S., Toksoz, M. N., Veatch, R. W., Baria, R., Augustine, C., Murphy, E., Negraru, P., and Richards, M. (2007). Impact of enhanced geothermal systems on US energy supply in the twenty-first century. *Philosophical transactions. Series A, Mathematical, physical, and engineering sciences*, 365(1853):1057–94.

Thiem, G. (1906). Hydrologic methods. *Gebhardt, Leipzig, Germany.*

Timoshenko, S. and Goodier, J. (1951). Theory of elasticity. *New York: McGraw-Hill.*

Turbitt, T., Walker, A., and Browitt, C. (1987). Perceptible hydrofracture seismic events caused by the Hot-Dry-Rock Geothermal Project in Cornwall. *Global*

Seismology Report Number 339. British Geological Survey, Edinburgh, U.K., 23 pp.

Urpi, L., Rinaldi, A. P., Rutqvist, J., Cappa, F., and Spiers, C. J. (2016). Dynamic simulation of CO2 injection-induced fault rupture with slip-rate dependent friction coefficient. *Geomechanics for Energy and the Environment*.

Veling, E. J. M. (2012). Radial transport in a porous medium with Dirichlet, Neumann and Robin-type inhomogeneous boundary values and general initial data: analytical solution and evaluation. *Journal of Engineering Mathematics*, 75(1):173–189.

Verruijt, A. (1969). Elastic Storage of Aquifers, in: Flow through Porous Media (R.J.M. De Wiest, editor). *Academic Press, New York*.

Verruijt, A. (2013). Theory and problems of poroelasticity. *Delft University of Technology*.

Vilarrasa, V. (2016). The role of the stress regime on microseismicity induced by overpressure and cooling in geologic carbon storage. *Geofluids*.

Vilarrasa, V., Bolster, D., Olivella, S., and Carrera, J. (2010). Coupled hydromechanical modeling of CO2 sequestration in deep saline aquifers. *International Journal of Greenhouse Gas Control*, 4(6):910–919.

Vilarrasa, V., Carrera, J., and Olivella, S. (2013). Hydromechanical characterization of CO2 injection sites. *International Journal of Greenhouse Gas Control*, 19:665–677.

Wang, H. F. (1997). Effects of deviatoric stress on undrained pore pressure response to fault slip. *Journal of Geophysical Research*, 102(B8):17943–17950.

Wang, H. F. (2000). Theory of linear poroelasicity with applications to geomechanics and hydrogeology. *Princeton University Press*.

Wang, X. (1995). Thermal shock in a hollow cylinder caused by rapid arbitrary heating. *Journal of Sound and Vibration*, 183.5(5):899–906.

Wang, Y. and Dusseault, M. B. (2003). A coupled conductive-convective thermo-poroelastic solution and implications for wellbore stability. *Journal of Petroleum Science and Engineering*, 38(3-4):187–198.

Wibberley, C. a. J., Yielding, G., and Di Toro, G. (2008). Recent advances in the understanding of fault zone internal structure: a review. *Geological Society, London, Special Publications*, 299(1):5–33.

Yeo, I., Freitas, M. D., and Zimmerman, R. (1998). Effect of shear displacement on the aperture and permeability of a rock fracture. *International Journal of Rock Mechanics and Mining Sciences*, 35(8):1051–1070.

Yin, S., Dusseault, M. B., and Rothenburg, L. (2007). Coupled multiphase poroelastic analysis of reservoir depletion including surrounding strata. *International Journal of Rock Mechanics and Mining Sciences*, 44(5):758–766.

Zang, A., Oye, V., Jousset, P., Deichmann, N., Gritto, R., McGarr, A., Majer, E., and Bruhn, D. (2014). Analysis of induced seismicity in geothermal reservoirs–an overview. *Geothermics*, 52:6–21.

Zimmerman, R. (2000). Coupling in poroelasticity and thermoelasticity. *International Journal of Rock Mechanics and Mining Sciences*, 37(1-2):79–87.

Zoback, M. D. (2007). Reservoir geomechanics: Earth stress and rock mechanics applied to exploration, production and wellbore stability. *Cambridge Press*.

Zoback, M. D. and Harjes, H.-P. (1997). Injection-induced earthquakes and crustal stress at 9 km depth at the KTB deep drilling site, Germany. *Journal of Geophysical Research*, 102(B8):18477.

Zoback, M. D., Townend, J., and Grollimund, B. (2002). Steady-State Failure Equilibrium and Deformation of Intraplate Lithosphere. *International Geology Review*, 44(5):383–401.